8

Shy-Yea Lin

Coherent Structures and Rotatinoal Effects on the Flow over Spinners of Horizontal Axis Wind Turbines

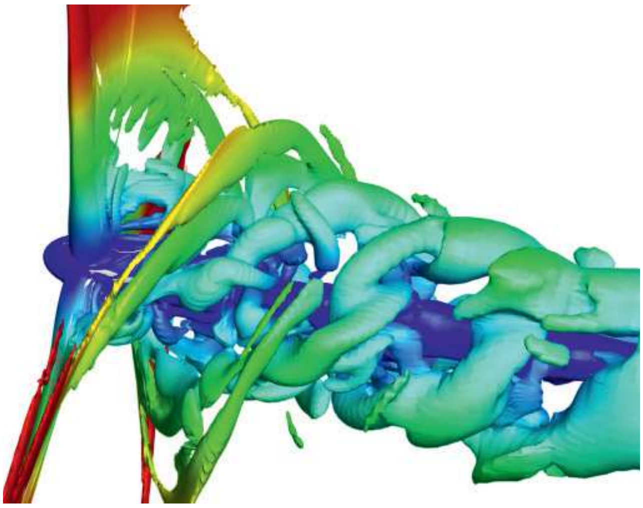

Berichte aus dem Institut für
Turbomaschinen und Fluid-Dynamik
Band 8/2016
Herausgeber: Jörg Seume

Institut für Turbomaschinen
und Fluid-Dynamik

COHERENT STRUCTURES AND ROTATIONAL EFFECTS ON THE FLOW OVER SPINNERS OF HORIZONTAL AXIS WIND TURBINES

Von der Fakultät für Maschinenbau
der Gottfried Wilhelm Leibniz Universität Hannover
zur Erlangung des akademischen Grades
Doktor-Ingenieurin
genehmigte Dissertation

von
Shy-Yea Lin, M.Sc.
geboren am 20. Dezember 1983
in Tainan, Taiwan

2016

KEYWORDS:
Wind Turbine Aerodynamics, Rotational Effects, Coherent Structures

SCHLAGWÖRTER:
Aerodynamik der Windenergieanlage, Rotationseffekte, kohärente Strukturen

MEMBERS OF THE THESIS COMMITTEE:
Prof. Dr.-Ing. Bernd-Arno Behrens (chair)
Prof. Dr.-Ing. Jörg Seume
Prof. Dr. Martin Kühn

DATE OF THE THESIS DEFENCE:
24 June 2016

ABSTRACT

Three-dimensional effects due to rotation which decrease the accuracy of predicting the wind turbine aerodynamic performance, are correlated with coherent structures near the blade roots, specifically with the flow separation. This study aims to give an insight into the complex coherent structures and the 3D rotational effects on the flow over spinners of horizontal axis wind turbines. The flow fields for the identification of the coherent structures and the 3D rotational effects are obtained by solving the Reynolds-averaged Navier-Stokes equations. The complex coherent structures, dominated by viscous shear layers are identified in this study by using various vortex detection methods. The coherent structures near the blade roots of the baseline wind turbine include helical root vortices, trailing edge vortices, flow separation with significant radial flows, von Kármán vortex streets, pairs of counter-rotating base vortices, horseshoe vortices, and a low-speed nacelle wake. The correlation between the helical root vortex and the blade-bound circulation is verified. The dominant sources responsible for the 3D rotational effect on attached and detached boundary layers are estimated by means of order of magnitude analysis. The 3D rotational effect on the baseline wind turbine results in lift augmentation, drag reduction, and significant radial flows in the flow separation region. The significant radial velocity components in the flow separation region are predictable, and substantially driven by the centrifugal acceleration. The Coriolis acceleration in the chordwise direction, induced by these significant radial velocity components in the bottom of the detached boundary layer, is balanced by a pressure gradient in the chordwise direction. This pressure gradient in the chordwise direction over the rotating blade agree well with the analytical expression derived in this study. The separation point is determined accurately in this study by a new criterion based on skin friction coefficients. The limited shift of separation points on the rotating blade, either towards the trailing edge or leading edge, indicates different effects due to rotation on the attached and detached boundary layers.

KURZFASSUNG

Die dreidimensionalen Rotationseffekte, die die Vorhersagegenauigheit der Leistung von horizontalachsigen Windenergieanlagen senken, hängen mit den kohärenten Strukturen im Nabenbereich, speziell mit der Ablösung, zusammen. Das Verständnis der komplexen kohärenten Strukturen und der dreidimensionalen Rotationseffekte auf die Strömung im Nabenbereich der horizontalachsigen Windenergieanlagen ist die Zielsetzung dieser Arbeit. Die Strömungsfelder zur Identifikation der kohärenten Strukturen und der 3D Rotationseffekte werden durch die Berechnungen der Reynolds-gemittelten Navier-Stokes Gleichungen ermittelt. Die komplexen kohärenten Strukturen, die von der viskosen Scherströmung behaftet sind, werden in dieser Arbeit durch verschiedene Methoden identifiziert. Die kohärenten Strukturen im Nabenbereich der Referenzanlage beinhalten den spiralförmigen Wurzelwirbel, den Hinterkantenwirbel, die Ablösung mit erheblicher radialer Geschwindigkeitskomponente, die Karman'sche Wirbelstraße, das gegenläufige Fußwirbelpaar, den Hufeisenwirbel und die langsame Nachlaufströmung hinter der Gondel. Der Zusammenhang des Ursprungs und der Entwicklung der spiralförmigen Wurzelwirbels mit der Zirkulation der Tragflügel wird verifiziert. Die dominante Parameter, die für die 3D Rotationseffekte auf die anliegende und abgelöste Grenzschichten verantwortlich sind, werden durch die Größenordnungsanalyse abgeschätzt. Die Rotationseffekte auf die Referenzanlage haben den Anstieg des Auftriebsbeiwerts, den Abfall des Widerstandsbeiwerts und die erhebliche radiale Strömung der Ablösung zur Folge. Die erhebliche radiale Geschwindigkeitskomponente der Ablösung entsteht durch die Zentrifugalkräfte und ist vorhersagbar. Die Coriolis-Beschleunigung in Richtung der Sehnenlänge, die durch die radiale Geschwindigkeitskomponente der Ablösung induziert wird, steht mit einem Druckgradienten in Richtung der Sehnenlänge im Gleichgewicht. Der Gradient des Druckbeiwerts in Richtung der Sehnenlänge der 3D rotierenden Rotorblätter stimmt mit der analytischen Korrelation, die in dieser Arbeit hergeleitet wurde, überein. Der genaue Ablösepunkt wird durch ein neues Kriterium, das auf Basis der Wandschubspannung definiert wurde, ermittelt. Die geringe Verschiebung des Ablösepunktes entweder in Richtung Hinter- oder Vorderkante des rotierenden Blattes zeigen die verschiedenen Einflüsse der Berücksichtigung der Rotationseffekte auf die anliegende und abgelöste Grenzschichten.

ACKNOWLEDGEMENTS

I am grateful to many people for making this adventure possible.

Firstly, I would like to express my sincere gratitude to my advisor Prof. Dr.-Ing. Jörg Seume for having believed in me from the start and for the freedom he gave me in my research project. His immense knowledge and heuristic guidance helped me throughout my research and writing of this thesis. Besides my advisor, I would like to thank the rest of my thesis committee: Prof. Martin Kühn and Prof. Dr.-Ing. Bern-Arno Behrens, for their insightful comments and hard questions in defense. My sincere thanks also go to Prof. Tzong-Hann Shieh for the recommendation and all the support that made this adventure possible to begin.

I am also grateful to Leibniz Universität IT Services (LUIS) and Norddeutscher Verbund für Hoch- und Höchstleistungsrechnen (HLRN) for the computational support. Furthermore, I would thank German Academic Exchange Service (DAAD) and Dr.-Ing. Joachim Runkel for the financial support. Without them, it would not be possible to conduct and accomplish this research.

I am very grateful to the colleagues at the Institute of Turbomachinery and Fluid Dynamics for all the help and the fun we have had together in the last years. I would particularly thank Diego Flores for great discussions and the time of brainstorming. I would also thank to Torben Wolff for his kindness in daily life and support in the German language. Special thanks also go to Benedikt Ernst and Thorsten kleine Sextro for the activities they organized which let me get to know my colleagues better.

Last but not the least, I would like to thank my family, particularly my mother Hsiu-Chih for the sacrifice and support for my studies abroad. To my later father, I am grateful for his guidance with his wisdom and humor. I would also like to thank Fadi Jabbour for supporting me spiritually through these years and my life in general.

Hanover, in July 2016 *Shy-Yea Lin*

CONTENTS

1 INTRODUCTION 1
  1.1 Motivation 2
  1.2 Literature survey 3
    1.2.1 Effects of spinner geometries on wind turbine aerodynamic performance 4
    1.2.2 Coherent structures near the blade roots 4
    1.2.3 Classification of 2D and 3D effects 6
    1.2.4 The 3D effects due to rotation 8
  1.3 Objectives and approach 17
  1.4 Overview 19
2 WIND TURBINE AERODYNAMICS 21
  2.1 Blade element momentum theory 21
    2.1.1 The axial momentum theory 21
    2.1.2 Glauert's general momentum theory 23
    2.1.3 The blade element momentum theory 26
    2.1.4 Determination of angle of attack using inverse BEM methods 30
  2.2 3D boundary layers on rotating blades 31
    2.2.1 Order of magnitude analysis of attached boundary layers 33
    2.2.2 Snel's order of magnitude analysis of detached boundary layers 36
    2.2.3 Corten's order of magnitude analysis of detached boundary layers 37
    2.2.4 Pressure distributions in the flow separation regions of rotating blades 39
3 COMPUTATIONAL SETUP 41
  3.1 The baseline wind turbine 41
  3.2 BEM iterations and profile aerodynamic data 44
    3.2.1 Computational setup of 2D stationary profiles 44
    3.2.2 BEM iterations 47
  3.3 The farfield CFD models 47
  3.4 The streamtube-based simplified CFD models 49
    3.4.1 Determination of streamtube coordinates 49
    3.4.2 Computational setup 49
    3.4.3 Validation of the simplified CFD models 53
4 RESULTS AND DISCUSSION 55
  4.1 Coherent structures near the blade roots 55
    4.1.1 An overall description of velocity and pressure fields 55
    4.1.2 Flow near the blade roots 57
    4.1.3 Coherent structures 60
    4.1.4 Root vortex origin and development 63
  4.2 Effects of spinner geometries 68
    4.2.1 Coherent structures 69

4.2.2 Aerodynamic performance . . . 69
4.3 3D effect due to rotation . . . 70
4.3.1 Aerodynamic performance . . . 71
4.3.2 Mechanisms . . . 79
5 CONCLUSIONS AND FUTURE WORK 95
5.1 Conclusions . . . 95
5.2 Future work . . . 96
BIBLIOGRAPHY 97
A APPROXIMATE SOLUTIONS OF IDEAL ROTOR DISCS 103
B 3D BOUNDARY LAYERS ON THE WIND TURBINE BLADE 105
CURRICULUM VITAE 111

LIST OF FIGURES

Figure 1.1 European annual and cumulative offshore wind installation 1
Figure 1.2 Flow features near the blade roots of horizontal axis wind turbines . . . 3
Figure 1.3 Comparison of the measured and predicted power curves of a NORTANK 300 kW turbine 4
Figure 1.4 The profile plane in the wind turbine system 7
Figure 1.5 Flow directions on rotating flat plates of (a) low aspect ratios and (b) high aspect ratios by means of ink dot of flow visualization 9
Figure 1.6 Lift coefficients of a rotating propeller blade at various radial positions . 10
Figure 1.7 Flow directions on a rotating propeller blade by means of flow visualization 11
Figure 1.8 The possible streamtube location as the boundary of the simplified CFD model (right) in consideration of the 3D flows near the blade tips and roots (left) 18
Figure 2.1 The actuator disc and the slipstream 22
Figure 2.2 The maximum energy output of an ideal wind turbine rotor disc predicted by Glauert's general momentum theory 25
Figure 2.3 Velocity components experienced by a blade element of a horizontal axis wind turbine 27
Figure 2.4 Decomposition of the lift and drag on the blade element in the axial and tangential directions 28
Figure 2.5 The discontinuity of Glauert's empirical correction in turbulent wake states when considering the tip loss correction factor 29
Figure 2.6 Coordinate system attached to a rotating blade 32
Figure 2.7 The chordwise pressure coefficient gradient in the flow separation region of a rotating profile as a function of the velocity ratio at various chord-to-radius ratios 40
Figure 3.1 The geometrical properties of the baseline wind turbine 43
Figure 3.2 The composition of the baseline wind turbine blade 44
Figure 3.3 Various spinner designs of the baseline wind turbine 45
Figure 3.4 The hexahedral mesh grid (left) and boundary conditions (right) of the 2D CFD models for the determination of stationary aerodynamic characteristics 45
Figure 3.5 Estimated chord Reynolds number and Mach number of the baseline wind turbine without considering induced velocities 46
Figure 3.6 The hexahedral mesh grid of the blade section (left) and in the hub region of the farfield CFD models 48
Figure 3.7 The boundary conditions of the 3D CFD models 49
Figure 3.8 Determination of the streamtube coordinates 50

Figure 3.9 The mesh grid generated in AutoGrid5 (left) and the boundary conditions (right) of the streamtube-based CFD models 51

Figure 3.10 Sensitivity study of the local performance coefficients to the mesh quality and dimensionless cell height adjacent to the blade surface of the baseline wind turbine at $U_\infty = 11.4$ m/s by using different mesh tools . 52

Figure 3.11 Comparison of the local performance coefficients of the baseline wind turbine using the farfield and simplified CFD models at $U_\infty = 11.4$ m/s 54

Figure 4.1 Azimuthally averaged velocity components and pressure over the effective annular area as a function of axial position 56

Figure 4.2 Slice positions and the view direction for studying flow features near the blade roots 57

Figure 4.3 Time-averaged velocity distributions of the inboard flow over the baseline wind turbine at the rated wind speed of $U_\infty = 11.4$ m/s. 58

Figure 4.4 The out-of-plane vorticity distributions evaluated from the time-averaged velocity fields over the baseline wind turbine at the rated wind speed of $U_\infty = 11.4$ m/s 59

Figure 4.5 The streamline patterns on the blade suction side 60

Figure 4.6 The vortex core structures near the blade roots of the baseline wind turbine at $U_\infty = 11.4$ m/s (isosurface of $Q = 0.05$) 61

Figure 4.7 The vortex core structures based on (a) the transient and (b) the time-averaged velocity fields near the blade roots of the baseline wind turbine at $U_\infty = 11.4$ m/s (isosurface of $Q = 0.05$) 62

Figure 4.8 The sketch of the coherent structures near the blade roots of a modern wind turbine 63

Figure 4.9 The dependence of the helical pitch on the wind speeds (isosurface of $Q = 0.05$ based on RANS computational results) 64

Figure 4.10 Determination of (a) the spatial position of the root vortex center and (b) the root vortex size and strength 65

Figure 4.11 The variation of (a) the radial position and (b) the azimuthal angle of the root vortex line as a function of dimensionless axial position 66

Figure 4.12 The development of the root vortex core in (a) size and (b) strength at various wind speeds 66

Figure 4.13 Blade-bound circulation and its spanwise gradient evaluated from the BEM predictions and CFD results 68

Figure 4.14 The vortex core structures based on the time-averaged velocity fields near the blade roots over various spinner geometries at $U_\infty = 11.4$ m/s (iso-surface of $Q = 0.05$) 69

Figure 4.15 The influence of the spinner geometry on (a) the overall power output and (b) the overall rotor thrust 70

Figure 4.16 Local power coefficients of the baseline wind turbine with various spinner designs 71

Figure 4.17 Local thrust coefficients of the baseline wind turbine with various spinner designs 71

Figure 4.18 Comparison of the overall power and thrust on the baseline wind turbine at various wind speeds predicted by BEM and CFD computations . 73
Figure 4.19 Local power, thrust, and torque coefficients as a function of radius at various wind speeds 74
Figure 4.20 The axial, rotational induction factors and loss correction factors as a function of radius at various wind speeds 75
Figure 4.21 Comparison of the geometrical angle of attack α_{geo} and the effective angle of attack α at (a) $U_\infty = 11.4$ m/s and (b) $U_\infty = 20$ m/s 76
Figure 4.22 Local chord Reynolds number as a function of radius at various wind speeds 76
Figure 4.23 The aerodynamic coefficients of the 3D rotating wind turbine blades and the 2D stationary profiles 78
Figure 4.24 The circumferential velocity fields and the aerodynamic characteristics of the 3D rotating wind turbine blades at $U_\infty = 11.4$ m/s and the 2D stationary profiles at the same angles of attack 80
Figure 4.25 The circumferential velocity fields and the aerodynamic characteristics of the 3D rotating wind turbine blades at $U_\infty = 20$ m/s and the 2D stationary profiles at the same angles of attack 81
Figure 4.26 Determination of the boundary layer thickness 82
Figure 4.27 Boundary layer thickness on the suction side of the 3D rotating wind turbine blade relative to that of the 2D stationary profile 83
Figure 4.28 Displacement thickness on the suction side of the 3D rotating wind turbine blade relative to that of the 2D stationary profile 83
Figure 4.29 Displacement thickness of the Ekman layer and the 3D boundary layer on the suction side of the wind turbine blade 85
Figure 4.30 Comparison of the separation points on the 3D rotating wind turbine blade relative to those of the 2D stationary profiles at the same angles of attack 87
Figure 4.31 The pressure distribution on the blade suction side estimated from the 2D stationary profile data and evaluated from the 3D rotating wind turbine blade at $U_\infty = 11.4$ m/s 89
Figure 4.32 Spanwise acceleration and velocity components in the boundary layer on the suction side of the wind turbine blade at $r/R = 0.176$ and $U_\infty = 11.4$ m/s 90
Figure 4.33 The velocity ratio as a function of normalized radius (RANS computations) 92
Figure 4.34 The chordwise gradient of the pressure coefficients in the flow separation region of the 3D rotating wind turbine blade in comparison with the analytical expression 93
Figure B.1 Spanwise acceleration and velocity components in the boundary layer on the suction side of the wind turbine blade at $r/R = 0.252$ and $U_\infty = 11.4$ m/s 105

Figure B.2 Spanwise acceleration and velocity components in the boundary layer on the suction side of the wind turbine blade at $r/R = 0.317$ and $U_\infty = 11.4$ m/s 106
Figure B.3 Spanwise acceleration and velocity components in the boundary layer on the suction side of the wind turbine blade at $r/R = 0.176$ and $U_\infty = 20$ m/s 107
Figure B.4 Spanwise acceleration and velocity components in the boundary layer on the suction side of the wind turbine blade at $r/R = 0.252$ and $U_\infty = 20$ m/s 108
Figure B.5 Spanwise acceleration and velocity components in the boundary layer on the suction side of the wind turbine blade at $r/R = 0.317$ and $U_\infty = 20$ m/s 109

LIST OF TABLES

Table 1.1 Classification of the 2D and 3D effects on non-yawed horizontal axis wind turbines . . . 6
Table 3.1 The rotor control of the baseline wind turbine . . . 41
Table 3.2 The blade geometry of the NREL offshore 5-MW baseline wind turbine (Jonkman et al. 2009) . . . 42
Table 3.3 The grid independence study of the selected NACA64618 airfoil at $\alpha = 4^\circ$ for the 2D CFD models . . . 46
Table 3.4 The grid independence study of the farfield CFD models at the rated operating conditions of $U_\infty = 11.4$ m/s . . . 48
Table 3.5 The grid independence study of the streamtube-based CFD models at the rated operating conditions of $U_\infty = 11.4$ m/s . . . 50
Table 3.6 Comparison of the cumulated aerodynamic performance of the baseline wind turbine up to $r = 40$ m/s using the farfield and simplified CFD models at $U_\infty = 11.4$ m/s . . . 53

NOMENCLATURE

LATIN SYMBOLS

Symbol	Unit	Description	Definition
A	m^2	area	
a	-	axial induction factor	
a'	-	rotational induction factor	
a_s	m/s	sound speed	
B	-	number of blades	
C_D	-	drag coefficient	Eq. (3.4)
C_f	-	skin friction coefficient	$\tau_\mathrm{w}/(0.5\rho U_\mathrm{ref}^2)$
C_L	-	lift coefficient	Eq. (3.3)
C_P	-	power coefficient	Eq. (2.6) or Eq. (2.21)
C_p	-	pressure coefficient	Eq. (2.53)
$C_{p,\,\mathrm{mod}}$	-	modified pressure coefficient	Eq. (4.15)
C_Q	-	torque coefficient	Eq. (2.20)
C_T	-	thrust coefficient	Eq. (2.5) or Eq. (2.19)
c	m	chord length	
D	N	drag	
F	-	Prandtl's correction factor	Eq. (2.32)
g	-	velocity ratio	Eq. (2.51)
L	N	lift	
Ma	-	Mach number	Eq. (3.2)
$\dot{m}$	kg/s	mass flow rate	Eq. (2.1)
n	m	coordinate normal to wall	Fig. 4.26
P	W	power	
p	Pa	pressure	
p_t	Pa	total pressure	
Q	N m	torque or Q-invariant	Eq. (4.3)
R	m	rotor radius	
Re	-	Reynolds number	Eq. (3.1)
r	m	radius	
r, θ, z	m, -, m	cylindrical coordinates	
$S_{i,j}$	1/s	strain-rate tensor	Eq. (4.5)
T	N	thrust	
U_∞	m/s	undisturbed wind speed	
U_ref	m/s	reference wind speed	
u_e	m/s	external free stream velocity	$u_\mathrm{e} = u_\mathrm{max}$ along n
u_i	m/s	velocity vector	
u_τ	m/s	friction velocity	$\sqrt{\tau_\mathrm{w}/\rho}$
x, y, z	m	Cartesian coordinates	
n^+	-	dimensionless wall distance	$\rho u_\tau n/\mu$

GREEK SYMBOLS

Symbol	Unit	Description	Definition
α	°	angle of attack	Eq. (2.23) or Fig. 2.3
α_{geo}	°	geometric angle of attack	Eq. (4.10)
β	°	blade pitch and twist angle	Fig. 2.3
Γ	m^2/s	blade-bound circulation, vortex strength	Eq. (4.7)
δ	m	boundary layer thickness	Eq. (4.11)
δ_1	m	displacement thickness	$\int_0^\delta \left(1-\sqrt{u_i^2}/u_\text{e}\right) \mathrm{d}n$
ζ_P	-	power deviation factor	Eq. (4.8)
ζ_T	-	thrust deviation factor	Eq. (4.9)
η	-	Glauert's efficiency factor	Eq. (A.3)
θ	°	azimuthal angle	
μ	kg/(m s)	dynamic viscosity	
ρ	kg/m^3	density	
τ	N/m^2	shear stress	
ϕ	°	inflow angle	Eq. (2.24) or Fig. 2.3
Ω	1/min	rotor speed	
$\Omega_{i,j}$	1/s	vorticity tensor	Eq. (4.4)
ω	1/s	rotational speed, vorticity	

SUBSCRIPTS

Symbol	Description
∞	undisturbed flow
$\perp$	perpendicular
$\parallel$	parallel
2D	stationary, two-dimensional airfoils
3D + Ω	rotating, three-dimensional wind turbine blades
D	rotor plane
e	external free stream
eff	effective
E	Ekman layer
max	maximal
mod	modified
ref	reference
s	separation point
W	wake
w	wall

OPERATOR

Symbol	Description
Δ	difference or distance
$\equiv$	definition to

ACRONYMS

2D	two-dimensional
3D	three-dimensional
BC	blunt conical
BE	blunt elliptical
BEM	blade element momentum
CAD	computer-aided design
CFD	computational fluid dynamics
COE	cost of energy
EEA	European Environment Agency
EL	elliptical
EU	European Union
EWEA	European Wind Energy Association
GCI	grid convergence index
HAWT	horizontal axis wind turbine
MEXICO	model experiments in controlled conditions
NASA	National Aeronautics and Space Administration
NREL	National Renewable Energy Laboratory
RANS	Reynolds-averaged Navier-Stokes
RMS	root mean square
SST	shear stress transport

1

INTRODUCTION

Wind turbines convert the kinetic energy of the wind into electrical power. In contrast, windmills convert the wind's energy into mechanical power and have been used in this way for at least the 3000 years (Burton et al. 2011, Gasch and Twele 2010). The first use of wind energy to generate electricity appeared at the end of the 19th century. At that time, people tried to couple electrical generators with a windmill rotor. A notable example is the windmill that was built in 1887 by Charles Brush in the USA (Sørensen 2011). Since then, the use of small wind electric generators has become wide spread and from them, the forerunners of modern wind turbine rotors appeared which have three blades and true airfoil shapes (Sørensen 2011).

Wind played an important role in energy generation until the advent of the steam engine and the appearance of other technologies for converting fossil fuels into useful energy. In the mid of the 20th century, the awareness of the environmental consequences of burning fossil fuels and its finite reserves caused people to look for alternative clean and renewable energy sources. As wind is one of the most promising renewable energy sources available, wind energy emerged again in the late 1960s. The 1990s saw a strong worldwide resurgence in the wind industry, with an installed capacity over five-fold of what was previously there at the beginning of the decade. This can be attributed to the political policies and financial support for the research and development of wind technologies (Manwell et al. 2009).

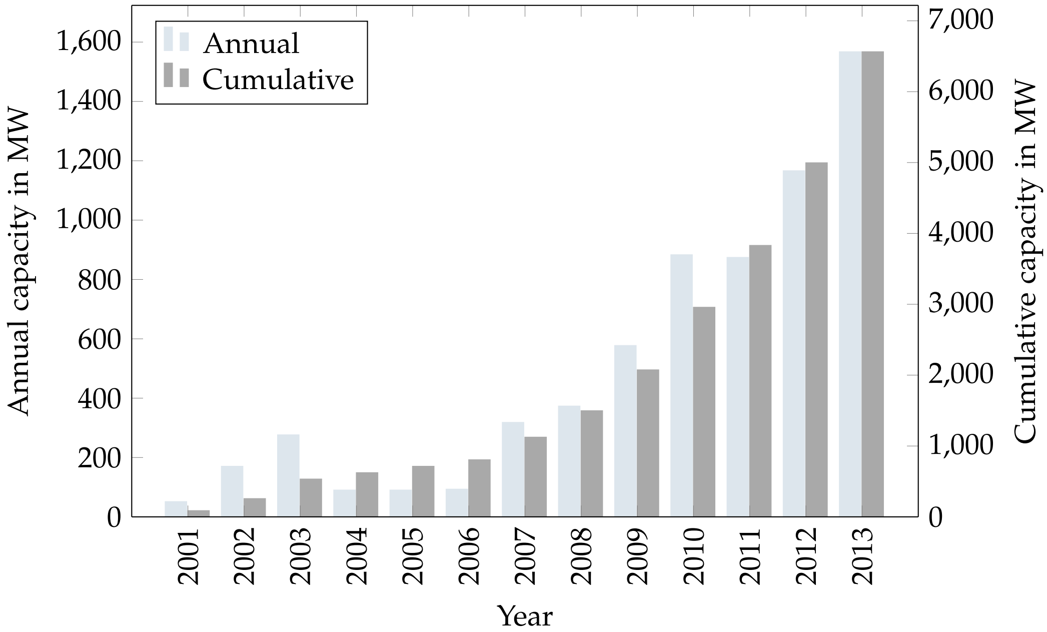

Figure 1.1: European annual and cumulative offshore wind installation (source: Corbetta et al. 2014)

The rated power of a horizontal axis wind turbine (HAWT) is proportional to the square of the rotor diameter, whereas the rotor mass and cost increase with the cube. The optimal rotor size of a HAWT is determined by the minimum specific cost of energy (COE) and varies from 44 m for zero wind shear using a simplified cost model, to approximate 70 m using the National Renewable Energy Laboratory (NREL) cost model for an isolated wind turbine with a rated performance of 1.5 MW (Burton et al. 2011). The current largest commercial wind turbine was introduced by MHI Vestas Offshore Wind$^{\text{TM}}$ in January 2014 (`http://www.mhivestasoffshore.com`). The rotor has a diameter of 164 m, apparently larger than the optimum values. Larger turbines are chosen because they can better exploit the wind energy in a limited area in order to reach a greater annual energy production.

According to the European Wind Energy Association (EWEA) report, the European Union (EU) plans to increase the capacity of renewable energy by up to 20% and reduce the carbon emissions by 20% by 2020 (European Wind Energy Association 2013). Due to the lack of available land with good wind resources for wind turbines, offshore wind technology has been of great interest in the past twenty years, particularly in northern Europe. Europe's offshore wind potential was estimated by the European Environment Agency (EEA) to be able to meet Europe's demand. Therefore, the installed capacity of offshore MW-scaled wind turbines is now growing rapidly (Fig. 1.1).

1.1 MOTIVATION

With the increasing rotor size of wind turbines, the structural stability plays a more crucial role in the design process. Cylindrical shells are one of the most employed designs for blade roots because they provide great structural stiffness and fit pitch-bearing configurations for pitch-controlled wind turbines. With this design, the cylindrical blade root transits smoothly to the innermost airfoil section, forming a thick inboard region. Although the cylindrical shape benefits structural strength, it induces a von Kárman vortex street which leads to periodic loads on the rotor blades. This periodic vortex street, which is usually characterized by Strouhal numbers (Schlichting 1979), may cause failure if it meets the resonant frequency of the rotor blade. Another significant flow structure near the blade roots is root vortices (Fig. 1.2 a), which are caused by the sudden drop in the blade-bound circulation. The root vortices are responsible for the power loss due to wake rotation. The thick inboard section also leads to an unfavorable flow separation (Fig. 1.2 b), which usually represents an aerodynamic loss for stationary airfoils. However, the flow behavior over rotating airfoils, particularly those with massive flow separation, differ from that of two-dimensional (2D) stationary profiles because of the three-dimensional (3D) effect due to rotation (Fig. 1.2 c). The 3D effect due to rotation causes significant lift augmentation, and consequently leads to power overshoot (Fig. 1.3). The rotational augmentation can be considered in the design process by implementing empirical correction models into design codes to correct the aerodynamic coefficients of the stationary profiles (Fig. 1.3). However, a comparison of the existing correction models for the 3D rotational effect shows that these models are inconsistent, and considerably dependent on the rotor blade design (Breton et al. 2008).

Since the flow near the blade roots is responsible for the aerodynamic stabilities and power overshoot, the coherent structures and 3D rotational effects are in the area of interest of this study. Flows passing over the spinner of the wind turbine accelerate and induce radial velocity components. Due to the fact that various spinner geometries exist within wind turbines, it is of importance to know how the spinner geometry affects the accelerated and radially-induced flow components. It is also important to know if the induced flow interacts with the inboard flow structures and affects the inboard aerodynamic performance.

1.2 LITERATURE SURVEY

There has been a wide range of work conducted regarding coherent structures near the blade roots of horizontal axis wind turbines and 3D effect due to rotation. As such, this section critically reviews the relevant literature and research attempts in the same direction as this work. This review will help identifying the gaps in the literature and hence help to articulate this research problem. This section is divided into three subsections. The first subsection discusses prior research related to the effects of spinner and nacelle design on wind turbine performance. The second subsection reviews a number of closely related efforts to identify the coherent structures near the blade roots. This is followed by an illustration of a number of works in the field of three-dimensional effects due to blade rotation.

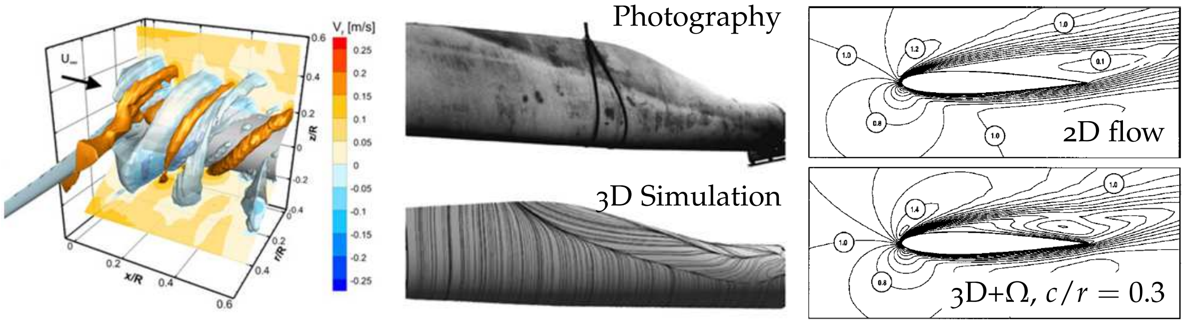
(a) Complex inboard flows (b) Flow separation (c) 3D rotational effects

Figure 1.2: Flow features near the blade roots of horizontal axis wind turbines: (a) Complex inboard flows. Reprinted from "Experimental investigation of the root flow in a horizontal axis wind turbine" by Akay, Ragni, Ferreira and van Bussel, 2013, *Wind Energy*, Vol. 17(7):pp. 1093–1109. Copyright 2013 by John Wiley and Sons. Reprinted with permission. (b) Flow separation. Reprinted from "3D numerical simulation and evaluation of the air flow through wind turbine rotors with focus on the hub area" by Rauch, Krämer, Heinzelmann, Twele and Thamsen, 2007, *Wind Energy: Proceedings of the Euromech Colloquium*, pp. 227–230. Copyright 2007 by Springer. Reprinted with permission. (c) 3D effect due to rotation. Adapted from "Investigating three-dimensional and rotational effects on wind turbine blades by means of a quasi-3D Navier-Stokes solver" by Chaviaropoulos and Hansen, 2000, *Journal of Fluids Engineering*, Vol. 122(2):pp. 330–336. Copyright 2000 by ASME. Adapted with permission.

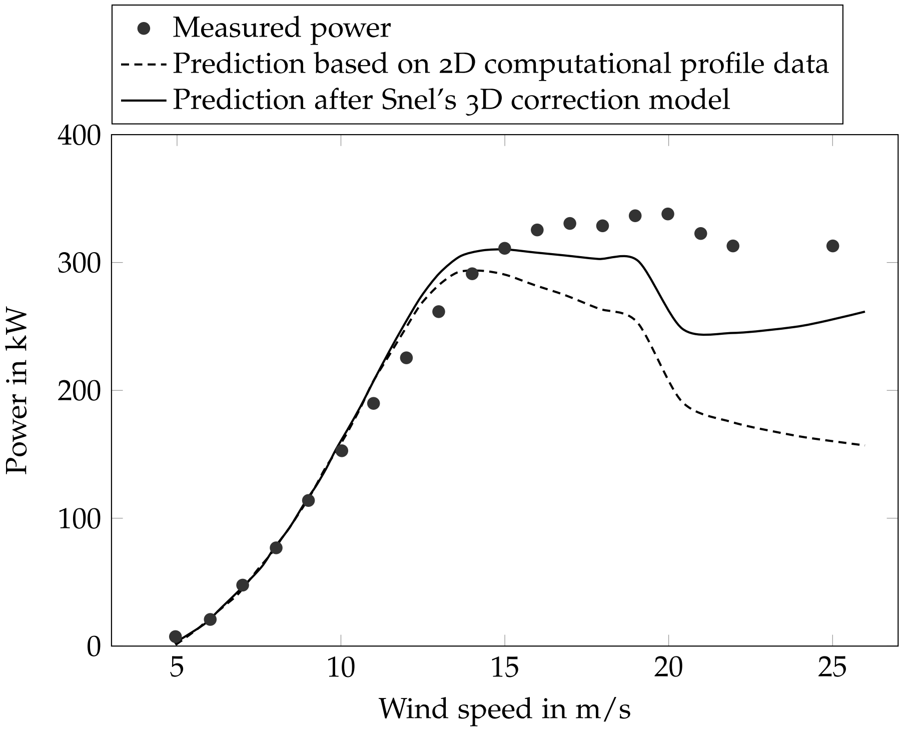

Figure 1.3: Comparison of the measured and predicted power curves of a NORTANK 300 kW turbine. Adapted from "Sectional prediction of lift coefficients on rotating wind turbine blades in stall" by Snel, Houwink and Bosschers, 1994, Technical report ECN-C–93-052. Copyright 1994 by the Energy research Center of the Netherlands (ECN). Adapted with permission.

1.2.1 *Effects of spinner geometries on wind turbine aerodynamic performance*

There have been few studies which consider the influence of spinner design on the performance of wind turbines. Johansen et al. (2006) investigate the inboard aerodynamic performance of a redesigned wind turbine with and without an egg-shaped spinner. In their study, the radius of the spinner is approximately 7% of the rotor radius. Their computational fluid dynamics (CFD) results showed no absolute increase in overall power and thrust coefficients. However, at selected operating conditions, local power and thrust coefficients slightly increased in the inboard region of the wind turbine with the egg-shaped spinner. They demonstrated that the increase in the local performance was caused by an increase in tangential velocities due to the spinner, which led to a pressure drop in the wake. Later, Johansen et al. (2009) proposed a similar rotor design in order to achieve the maximum mechanical power output. However, spinners and nacelles were excluded in their CFD models.

1.2.2 *Coherent structures near the blade roots*

Flows passing through wind turbines induce turbulent shear flows which may subsequently develop vortical structures, called coherent structures (Jeong and Hussain 1995). The coherent structures near the blade root of modern horizontal axis wind turbines, which have been identified so far in the literature, include helical root vortices (Vermeer et al. 2003, Sherry et al. 2013, Akay et al. 2013, Chow and van Dam 2012), trailing edge vortices, flow separation (Vermeer et al. 2003, Chow and van Dam 2012, 2013), von Kármán vortex shedding from cylinder blade roots (Zahle and Sørensen 2011), and a nacelle wake (Akay et al. 2013).

The formation of the root vortex, similarly to tip vortices, is basically caused by the abrupt drop of the blade-bound circulation in the blade root region. The root vortex shedding from the blade root further moves downstream and forms a helical structure due to the blade rotation. The occurrence of the root vortex represents an unfavorable power loss. The power loss due to the root vortex can be taken into account in the design process, by implementing loss factors such as Prandtl's loss factors into design codes (Burton et al. 2011). Root vortices were found shedding from the inboard section of the rotor blades experimentally and numerically, i. e., Whale et al. (2000) and Sherry et al. (2013). Akay et al. (2013) particularly demonstrated that root vortices were released from the maximum chord blade section and then rolled up towards a slightly larger radius. Sherry et al. (2013) observed that the root vortex was only evident closer to the rotor plane and dissipated rapidly due to the effects of the supporting structures of the wind turbine, i. e., the tower. The root vortex dissipates more slowly with the decreasing tip speed ratios (Chow and van Dam 2012). The accurate knowledge of the root vortex origin and development improves the accuracy of predicting the wind turbine aerodynamic performance, specifically the accuracy of the root-loss correction models (Lindenburg 2003). In comparison with tip vortices, whose properties have been thoroughly investigated such as its spatial position and vortex strength with increasing vortex age (Ebert and Wood 2001, Sherry et al. 2013), the corresponding information of root vortices are still unclear.

Flows over rotating wind turbine blades, particularly those in the flow separation region, are highly three-dimensional (Fig. 1.2 b). Significant radial flows in the flow separation region may lead to the extension of the flow separation region towards a larger radius, and subsequently result in an additional power loss (Corten 2001). Chow and van Dam (2012) used a simple full-chord fence to suppress the radial flows and improved the power performance by nearly 1%.

Von Kármán vortices are released from cylindrical blade roots and convected above the nacelle (Sherry et al. 2013, Zahle and Sørensen 2011). Zahle and Sørensen (2011) particularly demonstrated three prominent vortices shedding from each blade root in a series of vorticity contours at the planes perpendicular to the rotor axis near the nacelle end. One of these vortices referred to the root vortex, and the other two vortices forming a pair of counter-rotating vortices referred to von Kármán vortex street. This pair of unsteady vortices dominated the flow in the nacelle region and interacted with the root vortices, generating a high-velocity gradient. As a result, a significant variation in the wind speed and flow angle was measured above the nacelle. Zahle and Sørensen (2011) suggested that data measured by such as nacelle anemometers should be corrected for a more accurate rotor control.

Sherry et al. (2013) and Akay et al. (2013) observed the formation of a low speed, high turbulent, recirculated flow behind the nacelle. Sherry et al. (2013) concluded that the nacelle wake has a pronounced effect on root vortex stability.

In the past decade, coherent structure near the blade roots of horizontal axis wind turbine receive increasing attention, which is due to the urge to optimize wind park designs and accu-

Table 1.1: Classification of the 2D and 3D effects on non-yawed horizontal axis wind turbines

CATEGORY	MECHANISM	INFLUENCE	MODELS/SOLUTIONS
2D effects	blade cascade	limited and negligible	Weinig's coefficient
3D effects	blade solidity	unclear but supposed to be limited	-
	3D blade geometry	limited because of high aspect ratios	-
	end effect	significant at tips/roots	Prandtl's loss factor
	wake expansion	significant at highly loaded sections	unclear
	turbulent wake	significant at highly loaded sections	Glauert's relationship
	blade rotation	significant inboard	inconsistent models

rate wind turbine controls. Although there have been many experimental and computational attempts, a lack of physical descriptions remains, such as where is the origin of this pair of counter-rotating vortices, and how the root vortex develops as a function of traveling distances or life time. Aside from the root vortices, trailing edge vortices, flow separation, von Kármán vortex street, and nacelle wake, does another coherent structure exist near the blade roots of horizontal axis wind turbines and how do they interact with each other?

1.2.3 *Classification of 2D and 3D effects*

Because of complex rotor geometries, it is clear that in addition to the 3D effect due to rotation there are also other 3D effects influencing the blade aerodynamic characteristics. An apparent example is the end effect near the blade tip and the blade root. In order to accurately identify the 3D effect due to rotation, the presence of other 3D effects and their extent must be understood.

Table 1.1 lists the 2D and 3D effects due to various mechanisms which may affect the aerodynamic characteristics of the rotating wind turbine blade relative to those at stationary conditions. The 2D effects on the 3D flow over the wind turbine blades only change the velocity components parallel to the profile plane, i. e., there is no change in the velocity components perpendicular to the profile plane. The 3D effects further involve velocity components perpendicular to the profile plane. The profile plane of a 2D airfoil in a plane flow is defined in a flat plane. In contrast to the 2D airfoil, the profile plane in the wind turbine system is defined in a cylindrical surface which wraps about the rotor axis with a constant radius (Fig. 1.4 a). By unwrapping this cylindrical surface into a flat plane, a cascade with an infinite number of airfoils presents because of the circumferential periodicity of the rotor blades (Fig. 1.4 b).

A blade cascade is usually characterized by the space-to-chord ratio and the stagger angle for axial turbomachines, where the space implies the distance between the trailing edges of two neighboring profiles. The stagger angle implies the angle between the rotor axis and the blade chord. The reciprocal of the space-to-chord ratio is equivalent to the blade solidity for wind turbines. When the space-to-chord ratio is very large, i. e., low blade solidity, each blade can be regarded as isolated and no significant interference occurs. When the space-to-chord

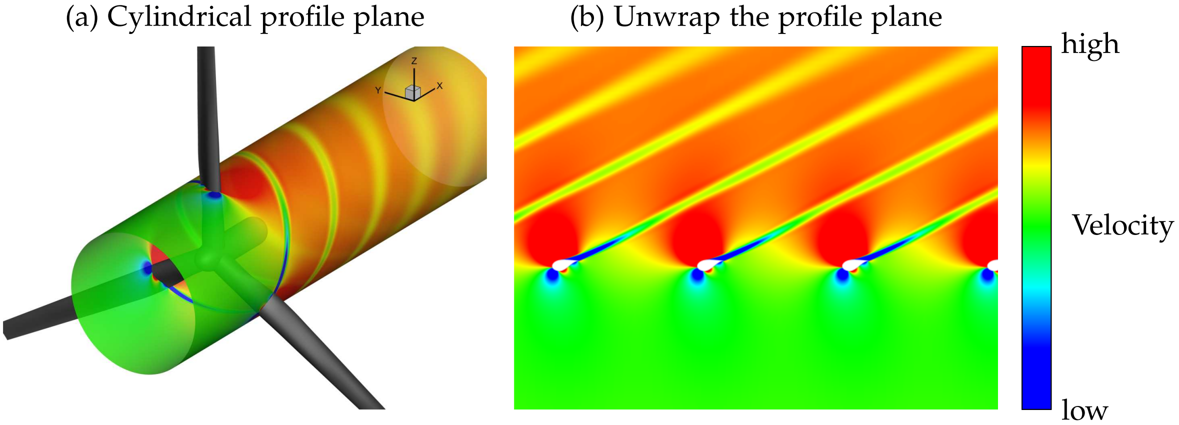

Figure 1.4: The profile plane in the wind turbine system

ratio reduces, i. e., high blade solidity, the aerodynamic characteristics of the profile in the cascade may change due to the increasing interference from neighboring profiles. The change in the airfoil aerodynamics due to the blade cascade can be approximately estimated by multiplying the lift coefficient of an isolated profile by Weinig's coefficients (Lakshminarayana 1996, Sec. 3.3.1). This study uses Weinigs's coefficients for a circular-arc-profile cascade to estimate the 2D effect due to blade cascade on the modern horizontal axis wind turbines, including the NREL/NASA-Ames Phase VI turbine (Hand et al. 2001) and the conceptual NREL 5 MW offshore baseline wind turbine (Jonkman et al. 2009). The space-to-chord ratios and stagger angles of these wind turbines are higher than 5 and 53°, respectively. The corresponding Weinig's coefficients asymptotically approach 1. Based on this estimation, the 2D effect due to blade cascade on the aerodynamic performance of horizontal axis wind turbines is supposed to be limited and assumed to be negligible in this study.

In contrast to the 2D profile cascade where the flow is restricted in the 2D plane, the cascade of the 3D wind turbine blades allows radial flow motion. With increasing blade solidities approaching the rotor axis and the blockage of the spinner, radial flows which are induced in the inboard region may lead to a 3D effect on the blade aerodynamics. This 3D effect due to the blade solidity is, however, unclear. This study assumes that the 3D effect due to the blade solidity is restricted near the rotor axis and has no significant effect on the inboard airfoil sections.

An optimum and efficient blade design usually involves complex blade geometries, see e. g., Burton et al. (2011, Chap. 3.7). The 3D blade geometry may induce radial velocity components and then lead to a 3D effect. This study suggests that this 3D effect due to the 3D blade geometry is limited and negligible because of the high aspect ratios of the modern wind turbine blades. An another 3D effect which is also related to the 3D blade geometry is the end effect at the blade tip and blade root. The 3D effect due to the end effect is usually significant and predictable by Prandtl's loss factor (Burton et al. 2011).

Due to the flow deceleration through the wind turbine blades, flow expansion occurs and induces radial velocity components. The 3D effect due to flow expansion is significant for highly-loaded blade sections. Although the accurate 3D effect due to flow expansion is still unclear and difficult to identify, this study assumes that the 3D effect due to flow expansion in the inboard region of horizontal axis wind turbines is limited and negligible.

The decelerated flow which passes through the wind turbine rotor induces turbulent shear layers adjacent to external free streams. Due to the mass, momentum, and kinetic energy mixtures within the turbulent shear layer, the local blade sections may exceed the limitation of the maximal power output predicted by the momentum theory. The turbulent wake state is significant when the blade section is highly loaded. The 3D effect due to turbulent wake on the local aerodynamic performance is usually estimated by Glauert's empirical relationship (Buhl 2005).

As the rotor blade rotates, another 3D effect due to blade rotation occurs. This 3D effect can be preliminarily understood by considering the flow near a rotating disc which rotates about an axis perpendicular to its plane at a constant angular velocity in a rest fluid. The 3D flow near the rotating disc has been accurately described by Schlichting (1979, pp.102-107): "The layer near the disc is carried by it through friction and is thrown outwards owing to the action of centrifugal forces. This is compensated by particles which flow in an axial direction towards the disc to be in turn carried and ejected centrifugally." This process is usually known as the centrifugal pumping effect (McCroskey and Yaggy 1968). The radial flows due to the centrifugal pumping effect are only significant in the boundary layer over the rotating disc, specifically in the bottom of the boundary layer. Schlichting (1979, pp.102-107) also drew some important conclusions, for example that the pressure gradient as function of the distance from the wall is very small for small viscosities, and there is no pressure gradient in radial direction over the rotating disc. Although the flow near the wind turbine blade is more complex, understanding the flow behavior over a rotating disc and its mechanism help in understanding the complex flow behavior over the rotating wind turbine blades, and the mechanism responsible for the corresponding flow behavior.

In contrast to the rotating disc in a stationary fluid, the incoming flow over the rotating wind turbine blades further induces significant spanwise pressure gradient. This study categorizes the spanwise pressure gradient into the 3D effect due to rotation since the spanwise pressure gradient is closely correlated with the relative fluid velocity with respect to the rotating blade. In the remainder of this thesis, the 3D effects due to rotation are also called the 3D rotational effects for simplification.

Based on the reconsideration of the possible 2D and 3D effects due to various mechanisms and the estimation of their extent, this study suggests that flows over 3D rotating wind turbine blades and flows over 2D stationary profiles can be regarded as flows with and without the 3D rotational effect, once the effects due to the other mechanisms have been carefully taken into account.

1.2.4 *The 3D effects due to rotation*

The 3D effect due to rotation is not a unique phenomenon to wind turbines, it also occurs in the boundary layers over propellers and airscrews. Through the development of propellers and airscrews, the 3D rotational effect was widely investigated. However, at that time due to the limitation of experimental techniques and computational capacities, the understanding of the 3D boundary layers over rotating blades relied on flow visualization experiments and analytical solutions. Since then, with increasing computational capacities and the development of experimental technologies, more accurate flow features have been captured, which improved the understanding of the mechanism responsible for the 3D rotational effect. This section which gives a historical overview of former work regarding the 3D rotational effect is further divided into four groups according to the methodology.

A. EARLY EXPERIMENTAL AND ANALYTICAL STUDIES The publication of Himmelskamp (1950) is one of the first research investigating the 3D rotational effect on the aerodynamic characteristics of rotating profiles. Himmelkamp's work detected the most important phenomena caused by the 3D rotational effect such as the lift augmentation, thus the 3D rotational effect is also known as Himmelskamp effect, (see e. g., Ronsten 1992, Björck et al. 1994).

Before Himmelskamp's investigation, the 3D effect due to rotation on the boundary layer properties of rotating profiles relative to those of stationary profiles had already received attention. Significant radial flows in the flow separation region over rotating profiles were familiar. For instance, Gutsche (1940) used the ink dot technique of flow visualization to show that flows in the attached boundary layer on a rotating profile traveled chordwise parallel to external free streams, whereas flows in the flow separation region, specifically in the 'dead-water' region ('Totwasserbereich' in German), traveled radially towards the blade tip (Fig. 1.5). In

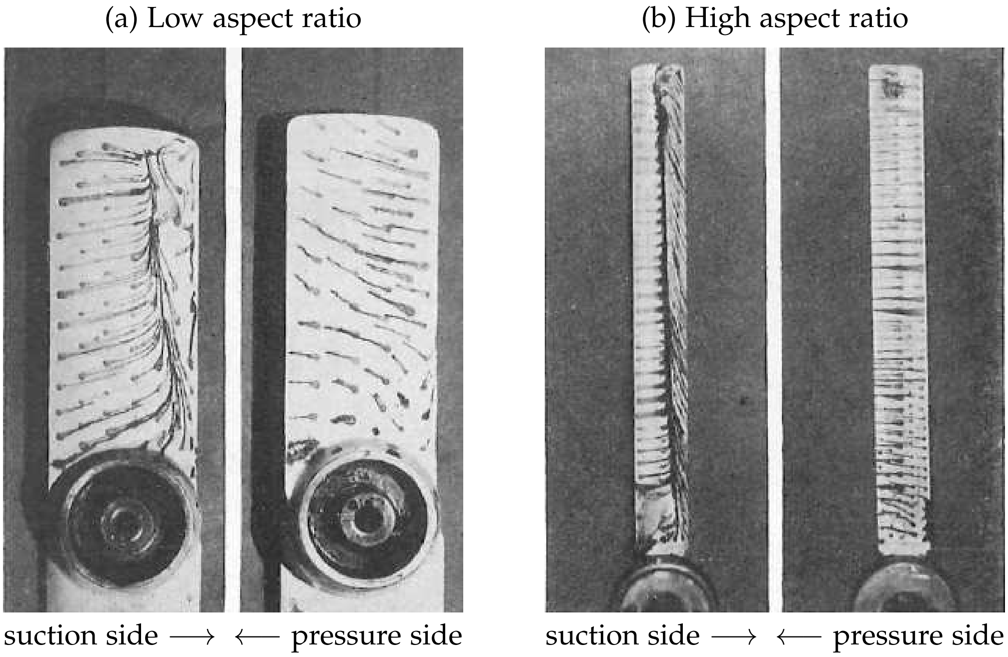
(a) Low aspect ratio
(b) High aspect ratio
suction side ⟶ ⟵ pressure side
suction side ⟶ ⟵ pressure side

Figure 1.5: Flow directions on rotating flat plates of (a) low aspect ratios and (b) high aspect ratios by means of ink dot of flow visualization. Reprinted from "Versuche an umlaufenden Flügelschnitten mit abgerissener Strömung" by Gutsche, 1940, *Mitteilungen der Preußischen Versuchsanstalt für Wasser-, Erd- und Schiffbau, Berlin*. Copyright 1940 by the German Federal Waterways Engineering and Research Institute (Bundesanstalt für Wasserbau, BAW). Reprinted with permission.

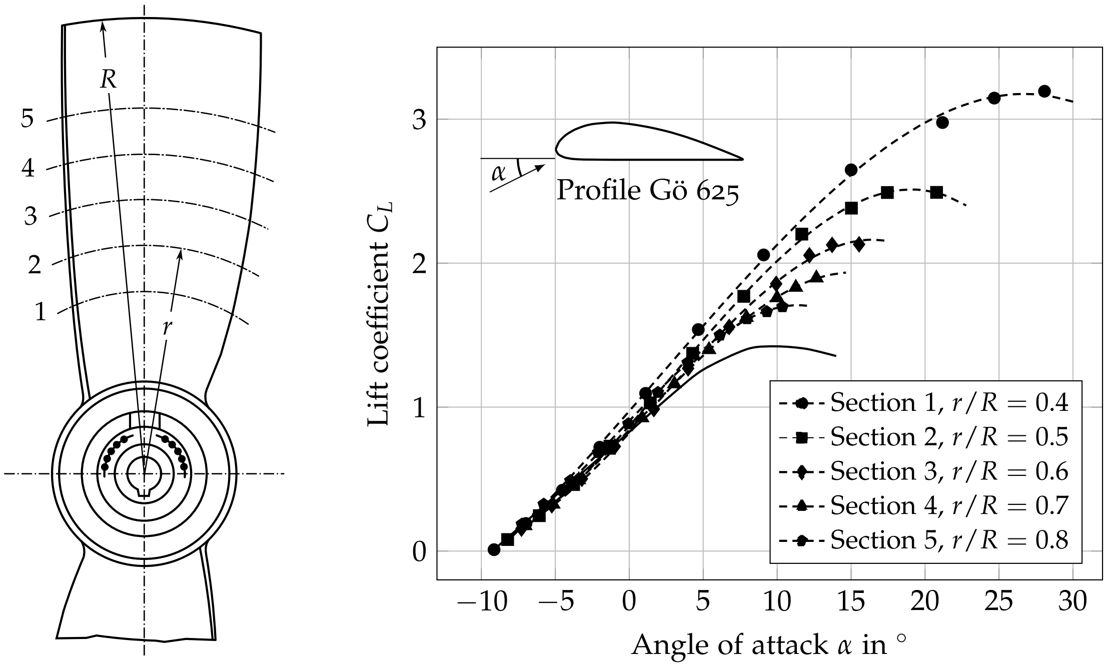

Figure 1.6: Lift coefficients of a rotating propeller blade at various radial positions. Adapted from "Profiluntersuchungen an einem umlaufenden Propeller" by Himmelskamp, 1950, *Mitteilung aus dem Max-Planck-Institut für Strömungsforschung*. Copyright 1950 by the Max Planck Institute for Dynamics and Self-Orgazination. Adapted with permission.

his dimensional analysis, he derived that flows in the dead-water region were pumped radially outwards by the centrifugal acceleration and pressure gradients in the radial direction.

Himmelskamp (1950) evaluated the aerodynamic coefficients of rotating propeller blades (Fig. 1.6 left) based on pressure measurements over the profile surface. He compared the aerodynamic data of the rotating profiles with those of stationary wind tunnel tests. His results show that the maximum lift coefficients of the rotating blade considerably increase, particularly in the inboard region, whereas no significant change occurs at the angles of attack of the linear region (Fig. 1.6 right). The maximal lift coefficients also shift to higher angles of attack, which implies the shift of stall angles of attack towards higher values, known as stall delay. Himmelskamp's results show an increase in the drag coefficients of the rotating profiles at high angles of attack.

Himmelskamp (1950) posited that the lift augmentation and stall delay occurred because the turbulent, detached boundary layer became attached due to the 3D rotational effect. He considered a boundary layer flow element $\mathrm{d}m$ at radius r and at an angular velocity ω, thus the centrifugal force acting on the flow element is $r\omega^2\mathrm{d}m$. Because of the centrifugal acceleration, he posited that the radial velocity of this flow element increased with the radius. He verified the significant radial flows in the boundary layer by flow visualization with filaments glued on the surface of the propeller (Fig. 1.7). As a result of these increasing radial velocity components with radii, he concluded that the boundary layer thickness of the propeller relative to that at stationary conditions decreased. The radial velocity components then yielded

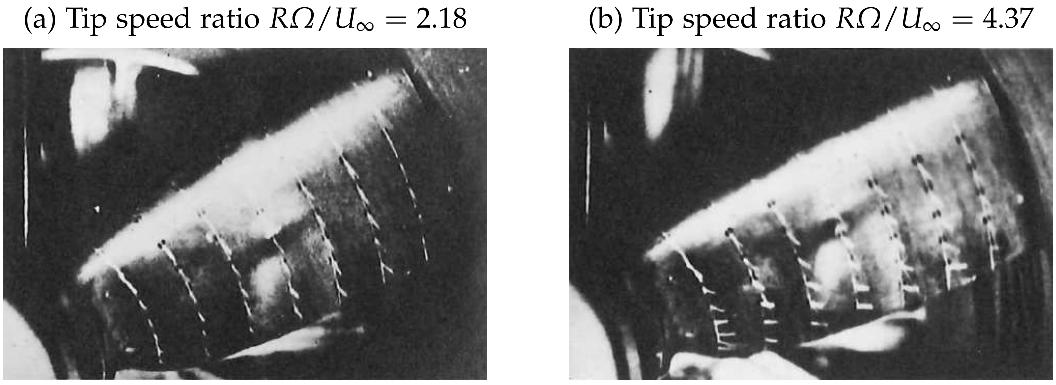
(a) Tip speed ratio $R\Omega/U_\infty = 2.18$

(b) Tip speed ratio $R\Omega/U_\infty = 4.37$

Figure 1.7: Flow directions on a rotating propeller blade by means of flow visualization. Reprinted from "Profiluntersuchungen an einem umlaufenden Propeller" by Himmelskamp, 1950, *Mitteilung aus dem Max-Planck-Institut für Strömungsforschung*. Copyright 1950 by the Max Planck Institute for Dynamics and Self-Orgazination. Reprinted with permission.

chordwise Coriolis acceleration against unfavorable chordwise pressure gradient on the profile suction side. This chordwise Coriolis acceleration benefited the attached boundary layer at higher angles of attack.

The author of this study argues against some of Himmelskamp's interpretations from his experimental results and the explanation of stall delay due to the 3D rotational effect. First, Himmelskamp regarded the boundary layers with significant radial flows as attached boundary layers, which basically contradicted Gutsche's (1940) illustration of the flow directions in the attached and detached boundary layers on rotating profiles. Thus, there should be still massive flow separation with significant radial flows over the rotating propeller blades. As a result of that, the increase in lift coefficient should not be caused by the shift of flow separation toward the trailing edge.

Second, since lift augmentation occurs while massive flow separation still exists over the rotating profiles, it means that the absence of stall does not imply the absence of flow separation for the rotating profiles. In contrast to a typical flat pressure distribution in the flow separation region over a stationary profile, the absence of a similar flat pressure distribution in the flow separation region over a rotating profile does not imply the absence of boundary layer separation, since the presence of the boundary layer separation over the rotating profile has been verified.

Third, Himmelskamp did not consider the period of time for the boundary layer element to be driven by the centrifugal force, which is basically inversely proportional to the radius. Thus, the radial velocity components in the attached boundary layer driven by the centrifugal force over this period of time should be approximately constant. Since the radial velocity components relative to the dominant, circumferential fluid momentum is inversely proportional to the radius, their influence on the blade section far from the rotor axis is negligible. Consequently, the boundary layer thickness of the rotating profile is supposed to be identical to that of the stationary profile. The limited radial velocity components yield limited chordwise Coriolis acceleration against unfavorable chordwise pressure gradients on the profile suction side.

The magnitude of this chordwise Coriolis acceleration due to the radial velocity components determines the change in the boundary layer properties and the shift of separation lines.

After Himmelskamp, much analytical work has been performed in order to confirm his experiments and verify his explanation that the 3D rotational effect delayed the flow separation towards the trailing edge. To this end, most analyzed the 3D boundary layer equations attached to a steadily rotating profile surface in order to accurately predict the onset of the flow separation.

Here, two things must be kept in mind: First, the boundary layer equations are not valid for the detached boundary layers due to a so-called Goldstein singularity (Goldstein 1948 and White 1991, p.6). Second, stall and flow separation are two distinctly different concepts in this study. Stall is specifically used to describe the abrupt loss of lift for airfoils at high angles of attack, while massive flow separation occurs on the profile suction side. That is to say, stall only regards the profile aerodynamic characteristics, whereas flow separation regards the physical flow conditions. It is rational to relate the presence of stall due to the occurrence of flow separation, but the absence of stall does not imply the absence of flow separation, particularly for the rotating profiles.

Fogarty (1951) considered boundary layers at stations several chord lengths from the rotor axis of a thin blade. He neglected relative small terms in the 3D boundary layer equations based on the order of magnitude analysis. The simplified 3D boundary equations show that the chordwise velocity is independent of the spanwise velocity due to rotation, thus the separation line is unaffected by rotation. At the end of his paper, he commented that his results contradicted the common expression of significant 3D effects due to rotation. He explained that rotation may have significant effects on the flow after separation lines. He also commented that his theory was not valid beyond the separation line, thus cannot predict lift augmentation of a rotating blade.

In contrast to Fogarty's analysis, Banks and Gadd (1963) considered the full 3D boundary layer equations attached to a rotating helical surface with a constant angular velocity Ω. They assume that flows over the helical surface undergo unfavorable pressure gradients and the tangential velocity components outside the laminar boundary layer at radius r and the azimuthal position θ is $r\Omega(1 - k\theta)$, where k is a constant representing the velocity gradient outside the boundary layer. The radial velocity outside the boundary layer was assumed zero. Their parameter study of various k shows that for $k \geq 6.8$, the boundary layer separation occurs very near the leading edge of the helical surface and the separation point is identical to that of the 2D stationary boundary layer. For smaller values of k, the 3D effect due to rotation postpones the separation line towards the trailing edge. For example, for $k = 0.7$, the separation point postpones approximately 13% relative to that of the 2D stationary boundary layer. For k less than about 0.548, the laminar boundary layer is completely stabilized and flow separation never occurs. They explained that the 3D effect due to rotation benefited the attached boundary layer against the unfavorable pressure gradient and increased the pressure rise between the leading edge and the separation point. The author of this study comments that the increase in the shift distance of the separation line with the decreasing velocity gradient k is a natural consequence because the period of time for centrifugal forces to accelerate the flow passing through the attached boundary layer increases with decreasing k. Corten

(2001) examined the minimum value of k for modern horizontal axis wind turbines, which is approximately between 2 and 4. He then suggested that the postpone of the flow separation towards the trailing edges of modern horizontal axis wind turbine blades due to the 3D rotational effect is limited and negligible.

Later, McCroskey and Yaggy (1968) analyzed the 3D boundary layer equations of helicopter rotors in forward flight with small-crossflow assumptions and quasi-steady approximations. Similar to Fogarty (1951), they only considered the boundary layers far from the rotor axis. Thus they drew a conclusion agreeing with Fogarty that the dominant primary flow was independent of the crossflow. Their numerical results show a considerable increase in the crossflow velocities on the verge of boundary layer separation. They concluded that the centrifugal pumping effects are more prominent in the retarded flow. They commented that their work with the small-crossflow assumption cannot predict stall characteristics accurately.

Dwyer and McCroskey (1970) extended previous work to the region near the axis of rotation by discarding the small crossflow assumption and considering the full 3D boundary layer equations. Their numerical and perturbation solutions of the laminar viscous flow over rotating profiles show that the 3D rotational effect is limited to the immediate vicinity of the rotor hub. Their results agree with McCroskey and Yaggy (1968) that the 3D rotational effect is sensitive to the chordwise pressure gradients. They explained that the postpone of flow separation towards the trailing edge was caused by the crossflow in the bottom of the boundary layer, which directly led to a favorable chordwise pressure gradient. The induced chordwise velocities, accompanied by an increase in the wall shear, then resisted flow separation.

Dwyer and McCroskey (1970) also performed flow visualization experiments of ammonia vapor. Similar to Gutsche (1940), they identified the laminar separation bubble as the region with significant outward flows driven by centrifugal forces. The separation lines, observed from their flow visualization experiments of the rotating cylinder and NACA0012 profile, agree with 2D calculations, which supports their conclusion that the 3D rotational effect only results in limited shifts of separation lines. They remarked that "the actual separation bubble appeared to be in the form of a short bubble, followed by an attached turbulent boundary layer." Based on this observation, they posited that the 3D rotational effect on separation lines and stall characteristics may be more significant in turbulent boundary layers.

Savino and Nyland (1985) conducted flow visualization studies on a full-scale wind turbine, in order to determine flow patterns on the blade suction side. They described that flows in the attached boundary layer was in the chordwise direction; flows in the separation region directed towards the blade tip, similar to Gutsche (1940). Their experiments, however, contradict the common expression that the 3D rotational effect postpones flow separation lines towards the trailing edges. "If the position of the separation line observed in these tests is compared to that obtained in two-dimensional wind tunnel tests for similar angles of attack, it appears that the separation line is from 10 to 20 percent of a chord length forward (toward the leading edges) for the rotating blade compared to the position found for a nonrotating blade." Corten (2001) posited that the significant radial flows in the separation region can enter attached flow at a larger radial position, and thereby advanced flow separation to a certain extent.

The 3D effect due to rotation on the separation line, specifically postpone or advance, based on the cumulated literature survey has no consistent conclusion, but it is supposed to be limited for horizontal axis wind turbines because of the high chord-to-radius ratios.

B. NUMERICAL INVESTIGATIONS BASED ON INTEGRAL MOMENTUM EQUATIONS Snel et al. (1994) conducted the order of magnitude analysis of the 3D boundary layer equations for the attached and detached boundary layers over a rotating blade, respectively. Their analysis for attached boundary layers is identical to that obtained by Fogarty (1951). Based on their oder of magnitude analysis, they simplified the 3D boundary layer equations by neglecting the relative small terms. They derived a set of quasi-3D boundary layer equations valid for both attached and detached boundary layers. They transformed this set of equations into dimensionless integral quantities. Le Balleur's model (Le Balleur 1981) is used to determine velocity profiles in the boundary layer because it is well suited for attached and separated flows.

Snel et al. (1994) numerical results show that lift augmentation is more pronounced near the axis of rotation, agreeing with Himmelskamp (1950). However, the drag coefficients of the rotating profile slightly decrease, contracting Himmelskamp results. Snel et al. particularly detected triangular pressure distributions in the flow separation region of the rotating profile, different from typical flat pressure distributions over a stationary profile. They identified the flow separation region with these triangular pressure distributions by means of negative surface friction coefficients and shape factors. Similar triangular pressure distributions in flow separation regions were also observed experimentally by Butterfield et al. (1990), Ronsten (1992), Brand et al. (1997), Schreck et al. (2007), Sicot et al. (2008), and computationally by Guntur and Sørensen (2015) who particularly commented on the inaccuracy of using pressure distributions to locate separation points of rotating profiles. The surface friction coefficient distribution over the rotating blade also shows a limited postpone of flow separation. The displacement thickness distributions show that the boundary layer thickness of the attached flow over the rotating blade is almost identical to that over the 2D stationary profile. The boundary layer thickness of the detached boundary layer slightly increases near the separation point then decreases considerably. Snel et al. explained that lift augmentation is caused by the decambering effect due to the reduction in the displacement thickness of the detached boundary layer.

Corten (2001) argued the validity of Snel et al. (1994) order of magnitude analysis for the detached boundary layers based on the boundary layer equations. He proposed another model based on the full 3D Navier-Stokes equations to deal with the detached boundary layers with significant radial velocities. His model predicts triangular pressure distributions in the flow separation region, agreeing with Snel et al. (1994). He commented that chordwise pressure gradients in the flow separation region must exist in order to balance the chordwise acceleration caused by Coriolis effect on the significant radial velocity component. Sicot et al. (2008) derived a semi-empirical relationship from Corten's model for the prediction of pressure distributions in the flow separation region. However, their semi-empirical relationship significantly deviates from their experimental results. Although there is some concern about the validity of the integral momentum equations proposed by Snel et al. (1994), their computational results support the proposition of Fogarty (1951) that the 3D rotational effect significantly influences detached boundary layers.

Later, Du and Selig (2000) extended the work of Snel et al. (1994) to investigate rotational effects on the boundary layer properties. They introduced Pohlhausen and power-law type of velocity profiles for laminar and turbulent boundary layers, respectively, to solve the integral equations. They demonstrated that the postpone of separation point due to the 3D rotational effect is more prominent with increasing rotor speed or decreasing radius. The decrease in the displacement thickness is more significant near the trailing edge. They further demonstrated that the effect of Coriolis forces on the boundary layer thickness was stronger than the centrifugal forces. Thus, they concluded that the 3D rotational effect will be smaller for larger wind turbines because of the reduction in Coriolis forces in thinner boundary layers.

Schreck and Robinson (2002) indicated that lift augmentation caused by the 3D effect due to rotation can occur independently of Reynolds number influences. However, Hu et al. (2006) agreed with the conclusions of Du and Selig (2000) that for increasing radius, the effect of Reynolds numbers on the separation position is stronger than the effects of Coriolis and centrifugal forces. Hu et al. explained that the significant radially outward flow in the separation region induced a chordwise acceleration through the Coriolis forces, which acts as a favorable pressure gradient, tending to delay the separation position towards trailing edges.

Dumitrescu et al. (2007, 2009, 2010) presented a series of work considering integral momentum equations. They concluded that lift augmentation was the consequence of the flow separation reattachment over a rotating blade at high angles of attack. Moreover, they concluded that Coriolis forces were mostly important near the rotor axis while crossflow derivatives were important at the onset of flow separation. Recently, Ramos-García et al. (2014) proposed a viscous-inviscid interaction model where the inviscid part used a 2D panel method and the viscid part used integral momentum equations to predict the aerodynamic behavior of rotating wind turbine blades. This strong interaction made it possible to overcome Goldstein singularity and to compute the boundary layer flow at and beyond the separation point. Instead of using surface friction coefficients, they used shape factors of $H = 2.5$ to define the onset of flow separation. Their numerical results showed that rotational effects decreased the growth of boundary layer and delayed the onset of flow separation, which led to lift augmentation and drag reduction.

C. RECENT COMPUTATIONAL WORK Shen and Sørensen (1999) developed a quasi-3D Navier-Stokes model in a rotating reference frame whose computational costs were similar to typical 2D airfoil computations. They neglected the radial convective terms in all momentum equations by assuming the spanwise velocities to be radially constant. They employed a velocity-vorticity form of the Navier-Stokes equations to determine the spanwise velocity components. Their order of magnitude analysis, similar to Snel et al. (1994), shows that the 3D rotational effect has significant influences on the attached and detached boundary layers near the rotor axis. On the outer part of the blade, rotational effects may only be related to separated flows. Based on the numerical results of NACA profiles, they concluded that the effect of rotation stabilized vortex shedding and suppressed the separation volume. The pressure coefficients on the suction side of the airfoils at a high incident angle of $20°$ decreased near the blade root, whereas the pressure coefficients on the pressure side and the overall surface friction coefficients experienced no significant change. They concluded that the rotational effects only influenced the pressure distribution. This influence was only significant in the separation region. Similar results were also derived by Chaviaropoulos and Hansen (2000). They explained that the 3D rotational effects were strictly caused by the Coriolis force and not by the centrifugal force. The centrifugal term was well-hidden in the pressure-like term in the governing equations. The separated flow in the 3D boundary layer was sucked and redirected radially by the Coriolis force, leading to a reduction in the separation volume. This reduction in the separation volume then led to a pressure drop on the airfoil suction side.

Narramore and Vermeland (1992) used 3D Navier-Stokes methods to investigate the mechanism responsible for the lift augmentation and drag reduction of a rotating blade near stall. However, their research was based on the assumption that the lift augmentation was caused by the delay of separation to higher angles of attack by Coriolis accelerations. No advanced description about the flow properties in the separation region was contributed. Hansen et al. (1994) developed a general purpose 2D/3D Navier-Stokes solver including the standard k-ϵ turbulence model where centrifugal and Coriolis terms were also considered in order to compute rotational effects. Their computational results confirmed the significant radial flow towards the blade tip in the separation region at the blade root. Carcangiu et al. (2007) developed a post-process tool to evaluate boundary layer properties for their CFD results of an untwisted blade with a constant chord length. The evaluated velocity profiles showed significant radial velocity components in detached boundary layers. They also observed that the lift and drag coefficients of the 3D rotating blade were higher than the 2D stationary case for the whole range of flow angles. They explained that the increase in lift coefficients at low angles of attack might be caused by cascade effects. More recently, Herráez et al. (2014) conducted CFD computations and compared with the model experiments in controlled conditions (MEXICO) of Boorsma and Schepers (2003). They concluded that stall delay and lift enhancement could exist independently of each other. Guntur and Sørensen (2015) further showed that the increase in the blade-bound circulation due to the 3D rotational effect yielded a disagreement in the position of stagnation points between stationary and rotating profiles at similar angles of attack.

D. ENGINEERING CORRECTION MODELS The 3D rotational effect must taken into account in the design process in order to predict the wind turbine aerodynamic performance more accurately. This is usually accomplished by implementing correction models into design codes to correct the aerodynamic coefficients of stationary profiles.

Snel et al. (1994) proposed a simple correction formula for lift coefficients based on order of magnitude analysis. Their model includes a key parameter of the chord-to-radius ratio and a calibration constant determined by measurements. Later, Lindenburg (2003) modified the model of Snel et al. (1994) by considering the local speed ratio as an additional parameter. Chaviaropoulos and Hansen (2000) extended the correction model of Snel for lift and drag coefficients. They introduced blade twist angles as another key parameter. The correction model proposed by Du and Selig (1998) considered the lift augmentation and the drag reduction. They used the chord-to-radius ratio and local speed ratios as key parameters. Several correction models were also proposed, such as Lindenburg (2004) and Dumitrescu and Cardoş (2009). Breton et al. (2008) implemented six different stall delay models to correct 2D aerodynamic coefficients into a lifting-line-prescribed wake vortex scheme and compared the predicted performance with the NREL phase VI measurements. They observed considerable discrepancies between the prediction and measurements. They concluded that these models cannot represent the flow physics accurately. Additionally, there was no generality within these correction models.

The 3D effect due to rotation on the aerodynamic characteristics and boundary layer properties has been investigated experimentally, analytically, and computationally for several decades. Although many attempted to explain the mechanism responsible for the lift augmentation, heretofore there is still no general, common explanation. The conflicting descriptions of the flow over the rotating profiles imply that there is insufficient knowledge to understand the complex 3D flow.

1.3 OBJECTIVES AND APPROACH

The objective of this study is to ascertain the mechanisms responsible for the 3D rotational effects by giving an accurate knowledge of the 3D rotational effects on the aerodynamic characteristics and boundary layer properties of 3D rotating wind turbine blades. This study also aims to identify the coherent structures near the blade roots of horizontal axis wind turbines, particularly those closely correlated to the 3D effects.

Direct measurements of the flow fields over the blades of a full-scale wind turbine are difficult and expensive. A scaled wind turbine in a wind tunnel is unable to accurately present the aerodynamic characteristics in the full-scale. As a result, the detailed flow fields over a full-scale wind turbine are captured in this study by means of CFD computations, specifically by solving the Reynolds-averaged Navier-Stokes (RANS) equations.

CFD computations are usually time-consuming and have some restrictions. The CFD computations of an isolated wind turbine with a rotor diameter D needs a wide computational domain in order to avoid disturbance from the boundary conditions. The distance from the rotor center to the boundaries varies from 2 to 20 rotor diameters (Tachos and Filios 2009, Sørensen and Schreck 2012, Chow and van Dam 2012). Since the flow near the blade roots are of interest in this work, a simplified model with a reduced computational domain is proposed in this study in order to accelerate computations and to reduce computational requirements. The concept of the simplified model is based on a smooth and steady streamtube through which no mass flow passes. The choice of the streamtubes is limited because of the 3D flow structures at the blade roots and tips (Fig. 1.8 left). The possible streamtube position as the boundary of the simplified model is within the 2D attached flow region (Fig. 1.8 right). There is no shortcut to determine the coordinates of the streamtube, because they are dependent on the operating conditions and the aerodynamic performance of every blade section. The only way to determine the streamtube coordinates is from CFD computations with conventional farfield boundaries.

In order to accurately identify the 3D effect due to rotation on profile aerodynamics and boundary layer properties, this study further conducts 2D CFD computations of stationary

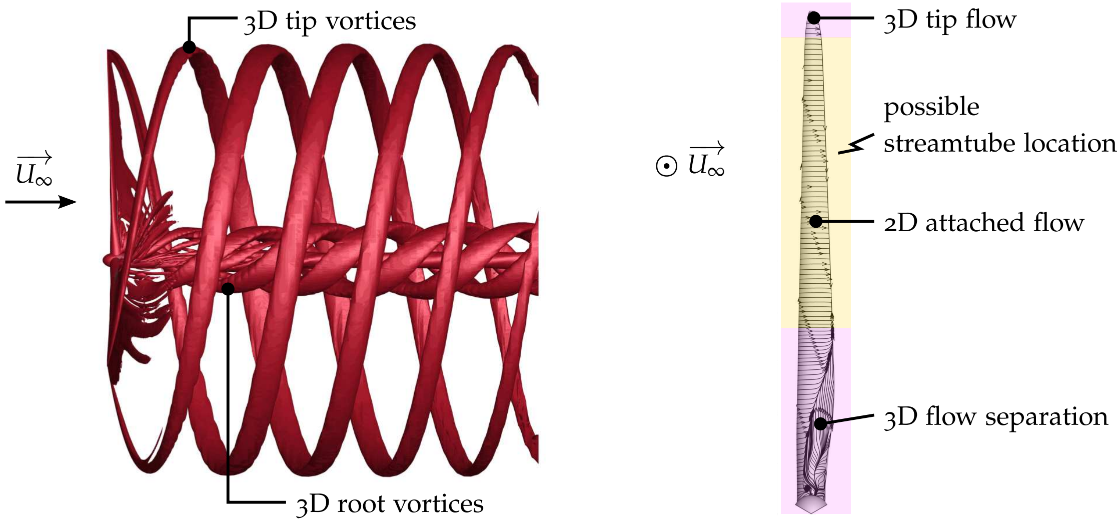

Figure 1.8: The possible streamtube location as the boundary of the simplified CFD model (right) in consideration of the 3D flows near the blade tips and roots (left)

profiles at various angles of attack. The power overshoot of a horizontal axis wind turbine is identified in this study by the comparison between the aerodynamic performance evaluated from the 3D CFD results and that of blade element momentum (BEM) predictions using stationary profile data from the 2D CFD computations.

The approach of this study based on the preceding concepts are summarized in the following. First, CFD computations of a horizontal axis wind turbine with conventional farfield boundaries at various operating conditions are conducted so as to obtain streamtube coordinates and corresponding inlet/outlet boundary conditions for the simplified CFD models. 2D CFD computations of stationary profiles at various angles of attack are also conducted, in order to predict the wind turbine aerodynamic performance by means of BEM methods. The coherent structures near the blade roots are detected by various vortex detection methods and summarized in a sketch. The 3D rotational effects on the wind turbine aerodynamic performance, namely the power overshoot, is identified by comparing the overall and local aerodynamic performance evaluated from the 3D CFD results with that of BEM predictions. Once the streamtube coordinates are determined, additional RANS computations using the streamtube-based simplified CFD models are conducted in order to validate the simplified CFD models and evaluate the errors that arise through their use. Subsequently, CFD computations using the streamtube-based simplified models with various spinner geometries are conducted in order to identify the influence of the spinner geometry on the inboard coherent structures and aerodynamics. A comprehensive and thorough investigation of the 3D rotational effect is carried out by comparing flows over the 3D rotating wind turbine blades, and those over the 2D stationary profiles. This comparison gives an insight into the 3D rotational effect on the aerodynamic characteristics and boundary layer properties. Mechanisms responsible for the 3D rotational effects are also estimated by the order of magnitude analysis. This study attempts to derive an analytical solution from Corten's model, in order to accurately predict the pressure distributions in the flow separation region over the rotating blade. This analytical solution is validated in this study by comparing with the 3D CFD results.

1.4 OVERVIEW

This thesis consists of five chapters. In Chap. 2, the related fundamentals are introduced, including the BEM methods and the order of magnitude analysis for the governing equations of attached and detached boundary layers. The derivation of an analytical expression for accurate prediction of the pressure distributions in the flow separation regions of rotating blades, is introduced in Sec. 2.2.4. Chapter 3 describes the baseline wind turbine and the computational setups. The validation of the streamtube-based simplified CFD models is presented in Sec. 3.4.3. The computational results are analyzed and presented in the subsequent Chap. 4, including the identification of the coherent structures near the blade roots of the baseline wind turbine, the influence of spinner geometries, and the 3D rotational effect. The last Chap. 5 draws conclusions from this work and makes some suggestions for future work.

2

WIND TURBINE AERODYNAMICS

The power overshoot caused by the 3D effect due to rotation is identified in this study by comparing the wind turbine aerodynamic performance evaluated from the 3D CFD computations and that of BEM predictions which use 2D stationary profile data. The classical BEM method and some correction models which are usually implemented in wind turbine design codes are introduced in this chapter. In order to understand how the centrifugal acceleration, Coriolis effects, and spanwise pressure gradient affect the boundary layer over a rotating blade, the order of magnitude analysis of the 3D governing equations of attached and detached boundary layers is also discussed in this chapter. The derivation of an analytical expression for accurate prediction of pressure distributions in the flow separation region over rotating profiles is introduced at the end of this chapter.

2.1 BLADE ELEMENT MOMENTUM THEORY

2.1.1 *The axial momentum theory*

A simple way to describe the wind turbine aerodynamics is the axial momentum theory, also called Rankine-Froude theory (Glauert 1935). The axial momentum theory, which was originally developed to analyze the energy conversion and efficiency of propellers, was successfully applied to wind turbines. The difference between the wind turbines and the propellers is the direction of energy conversion. The wind turbine extracts kinetic energy from the wind, whereas the wind extracts kinetic energy from the propeller, imparting a backward motion to the fluid in order to provide a forward thrust along its axis. The axial momentum theory described in this study is from the view of energy extractions by the wind turbine.

The axial momentum theory is a very fundamental knowledge in wind turbine aerodynamics, which can be easily found in wind energy textbooks such as Burton et al. (2011). The most important assumptions, governing equations, and the maximum energy output predicted by the axial momentum theory are briefly summarized here.

The axial momentum theory replaces the rotor by a homogeneous and infinitely thin disc, known as Froude's actuator disc (Glauert 1935), thus no specific rotor design has to be considered. Flows passing through the actuator disc is divided from those not passing through the disc by a slipstream (Fig. 2.1). The axial momentum theory considers only axial velocity components and ignores all the other energy loss sources. The stationary and incompressible flows in the slipstream decelerate smoothly, whereas their pressures increase smoothly before entering the actuator disc and abruptly drops at the disc plane yielding a thrust on the disc. Flows after entering the actuator disc then gradually recover their pressures as the undisturbed flow.

Flows within a control volume enclosed by the slipstream are described mathematically by the principles of mass conservation

$$\dot{m} = \rho A_\infty U_\infty = \rho A_\mathrm{D} U_\mathrm{D} = \rho A_\mathrm{W} U_\mathrm{W}, \tag{2.1}$$

momentum conservation

$$T = \dot{m}\left(U_\infty - U_\mathrm{W}\right), \tag{2.2}$$

and energy conservation

$$P = T U_\mathrm{D} = \frac{1}{2}\dot{m}(U_\infty^2 - U_\mathrm{W}^2), \tag{2.3}$$

where A and U are cross-sectional areas and axial velocities at various axial positions, and the subscripts of ∞, D and W denote flows at ultimate upstream, the rotor plane, and ultimate downstream, respectively. Equation (2.1), Eq. (2.2), and Eq. (2.3) derive that the axial velocity at the rotor plane is the arithmetic mean of those at ultimately upstream and downstream

$$U_\mathrm{D} = \frac{1}{2}(U_\infty + U_\mathrm{W}). \tag{2.4}$$

The axial velocities at the rotor plane and in the ultimate wake are usually further reformulated as $U_\mathrm{D} = (1-a)$ and $U_\mathrm{W} = U_\infty(1-2a)$ by introducing an axial induction factor a.

The axial momentum theory has some restrictions and is only valid for $a < 0.5$. For $a \geq 0.5$, the axial velocity in the ultimate wake becoming zero or negative violates the basic assumptions in the axial momentum theory. Physically, the flow state of $a \geq 0.5$ can occur, but the flow only slows down rather than reverses due to turbulent mixtures between the flows in the

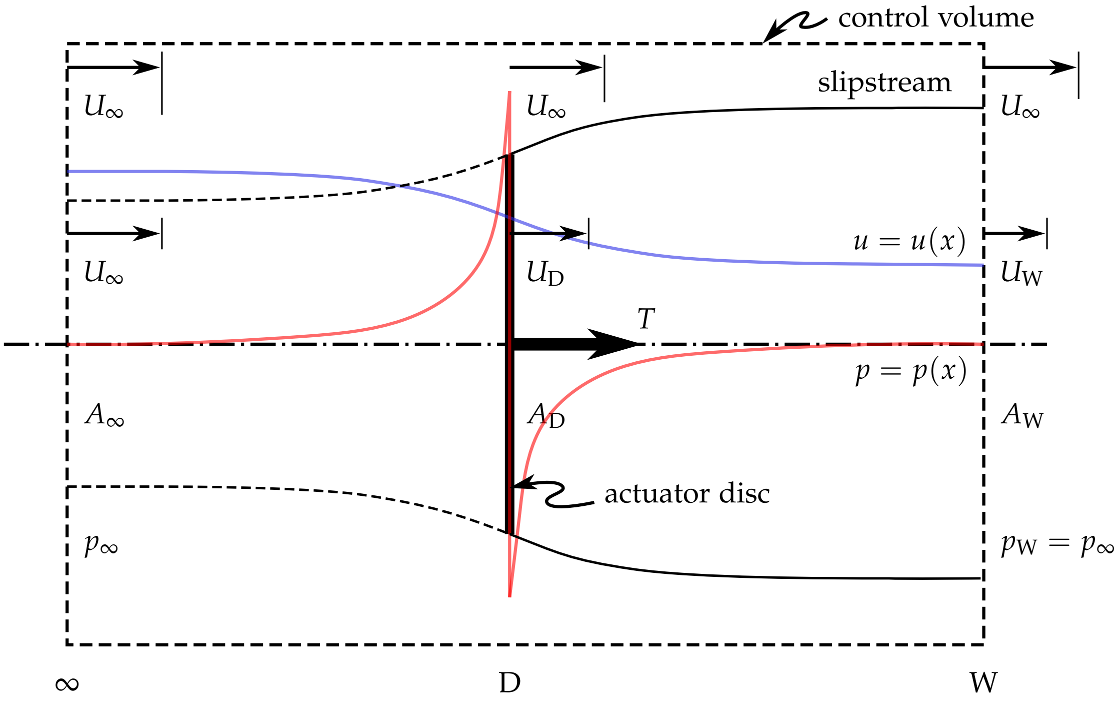
control volume
slipstream
U_∞
U_∞
U_∞
U_∞
U_D
$u = u(x)$
U_W
T
$p = p(x)$
A_∞
A_D
A_W
actuator disc
p_∞
$p_\mathrm{W} = p_\infty$
∞
D
W

Figure 2.1: The actuator disc model and the slipstream

slipstream and the undisturbed flows outside the slipstream. Under this condition, the axial momentum theory breaks down and empirical relationships should be taken into account in order to determine rotor's aerodynamic performance.

The overall aerodynamic performance of the actuator disc is usually expressed by the thrust coefficient

$$C_T = \frac{T}{\frac{1}{2}\rho A_{\mathrm{D}} U_\infty^2} = 4a(1-a), \tag{2.5}$$

and the power coefficient

$$C_P = \frac{P}{\frac{1}{2}\rho A_{\mathrm{D}} U_\infty^3} = 4a(1-a)^2, \tag{2.6}$$

which are defined as the ratios of the energy extracted by the actuator disc and the available energy of the undisturbed flow passing through the same area as the disc.

The maximum power output occurs at $a = 1/3$ while $C_T = 8/9$ and $C_{P,\max} = 16/27$. This maximum power coefficient is usually known as Betz-limit or Lanchester-Betz-Joukowski-limit (Van Kuik 2007).

2.1.2 *Glauert's general momentum theory*

The rotor shaft receives not only thrust but also torque, which leads to a change in the fluid's angular momentum and causes wake rotation. Glauert (1935, Chapter III) extended the axial momentum theory to a more general theory by considering this angular momentum.

Glauert's general momentum theory replaces the rotor by a rotating rotor disc. Thus, similar to the axial momentum theory, no specific rotor design is taken into account. The rotor disc is then divided into many annular elements. Flows passing through an arbitrary annular disc of a thickness $\mathrm{d}r$ at radius r are independent of neighboring flows and can be divided by two boundaries through the edges of the annular disc, forming an annular shell. The general momentum theory assumes that the velocity components and the pressure of the flow in the annular shell are azimuthally constant, and all the other energy loss sources are negligible.

This rotating rotor disc imparts an additional angular momentum to the fluid, leading to wake rotation, while the axial and radial components remain unaltered. Because of the wake rotation, a radial pressure gradient occurs in the wake

$$\frac{\mathrm{d}p_{\mathrm{W}}}{\mathrm{d}r_{\mathrm{W}}} = \rho \omega_{\mathrm{W}}^2 r_{\mathrm{W}} \tag{2.7}$$

in order to balance fluid's centrifugal force, where p, ω, and ρ denote pressure, angular velocity, and fluid density, respectively. Thus, the pressure in the wake is lower than the undisturbed outer flow, i. e., $p_{\mathrm{W}} \leq p_\infty$.

The continuity equation of the flow in the annular shell along the rotor axis is

$$U_\infty r_\infty \mathrm{d}r_\infty = U_{\mathrm{D}} r_{\mathrm{D}} \mathrm{d}r_{\mathrm{D}} = U_{\mathrm{W}} r_{\mathrm{W}} \mathrm{d}r_{\mathrm{W}}, \tag{2.8}$$

where U implies axial velocity component, and the subscripts of ∞, D, and W denote ultimate upstream, the rotor disc, and ultimate downstream, respectively.

The thrust on the annular rotor disc is equivalent to the decrease in the axial momentum of the flow in the annular shell

$$\mathrm{d}T = \rho U_\mathrm{D} \mathrm{d}A_\mathrm{D} (U_\infty - U_\mathrm{W}) + (p_\infty - p_\mathrm{W}) \mathrm{d}A_\mathrm{W}, \tag{2.9}$$

where $\mathrm{d}A = 2\pi r \mathrm{d}r$ is the cross-sectional area of the annular shell. Similarly, the torque of the annular rotor disc is equivalent to the increase in the angular momentum

$$\mathrm{d}Q = \rho U_\mathrm{D}\, \mathrm{d}A_\mathrm{D}\, r_\mathrm{D}^2 \omega_\mathrm{D}. \tag{2.10}$$

Furthermore, the power gained by the annular disc is equal to the multiplication of the torque of the annular disc and the rotor speed Ω

$$\mathrm{d}P = \Omega \mathrm{d}Q. \tag{2.11}$$

By applying Bernoulli's equation, the fluid's total pressures before entering the rotor disc

$$p_\infty + \frac{1}{2}\rho U_\infty^2 = p_\mathrm{D} + \frac{1}{2}\rho \left(U_\mathrm{D}^2 + V_\mathrm{D}^2\right) \tag{2.12}$$

and behind the rotor disc

$$p_\mathrm{D} - \Delta p + \frac{1}{2}\rho \left(U_\mathrm{D}^2 + V_\mathrm{D}^2 + r_\mathrm{D}^2 \omega_\mathrm{D}^2\right) = p_\mathrm{W} + \frac{1}{2}\rho \left(U_\mathrm{W}^2 + r_\mathrm{W}^2 \omega_\mathrm{W}^2\right) \tag{2.13}$$

determine the pressure drop at the rotor plane

$$\Delta p = p_\infty - p_\mathrm{W} + \frac{1}{2}\rho \left(U_\infty^2 - U_\mathrm{W}^2 + r_\mathrm{D}^2 \omega_\mathrm{D}^2 - r_\mathrm{W}^2 \omega_\mathrm{W}^2\right), \tag{2.14}$$

where $r_\mathrm{D}^2 \omega_\mathrm{D}^2$ and $r_\mathrm{W}^2 \omega_\mathrm{W}^2$ indicate the energy loss due to wake rotation. V_D is the radial velocity component at the rotor plane. Since the induced angular velocities in comparison with the rotor speed is very small, all the terms involving the square of the induced angular velocities are negligible. Thus, the energy loss due to wake rotation in Eq. (2.14) and the pressure gradient in the radial direction of the wake flow in Eq. (2.7) are negligible. As a result, the pressure in the ultimate downstream is equivalent to that of the undisturbed free stream, $p_\mathrm{W} = p_\infty$.

The pressure drop at the rotor plane can be also determined by considering the fluid's angular velocity relative to the rotating rotor disc. The relative angular velocities of the flow before the rotor disc, Ω, and behind the rotor disc, $\Omega - \omega_\mathrm{D}$, imply a pressure drop at the rotor plane

$$\Delta p = \rho \left(\Omega + \frac{1}{2}\omega_\mathrm{D}\right) \omega_\mathrm{D} r_\mathrm{D}^2. \tag{2.15}$$

Since the thrust of the annular disc is also equivalent to the integration of the pressure drop over the annular disc

$$\mathrm{d}T = \Delta p \mathrm{d}A_\mathrm{D}, \tag{2.16}$$

the axial velocity component at the rotor plane is then obtained from Eq. (2.9), Eq. (2.14), and Eq. (2.16)

$$U_\mathrm{D} = \frac{1}{2}(U_\infty + U_\mathrm{W}), \tag{2.17}$$

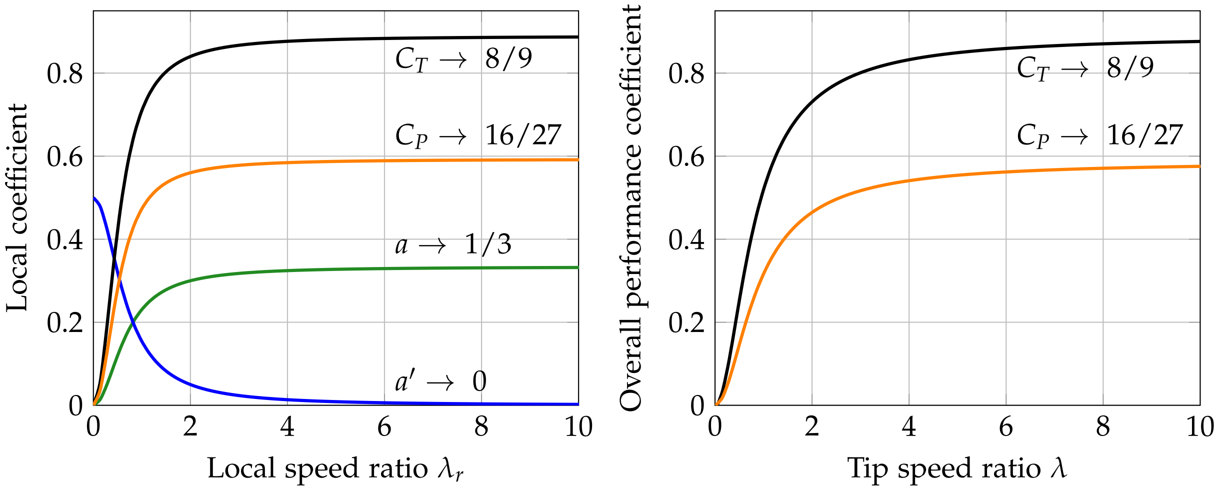

Figure 2.2: The maximum energy output of an ideal wind turbine rotor disc predicted by Glauert's general momentum theory

which is identical to Eq. (2.4) derived from the axial momentum theory. The angular velocity immediately behind the rotor disc is reformulated as

$$\omega_\mathrm{D} = 2a'\Omega, \tag{2.18}$$

where a' is the rotational induction factor.

The local aerodynamic performance of the rotor disc is usually expressed by the thrust coefficient

$$C_T = \frac{\mathrm{d}T}{\frac{1}{2}\rho U_\infty^2 \mathrm{d}A_\mathrm{D}} = 4a(1-a), \tag{2.19}$$

the torque coefficient

$$C_Q = \frac{\mathrm{d}Q}{\frac{1}{2}\rho U_\infty^2 r_\mathrm{D} \mathrm{d}A_\mathrm{D}} = 4a'(1-a)\lambda_r, \tag{2.20}$$

and the power coefficient

$$C_P = \frac{\mathrm{d}P}{\frac{1}{2}\rho U_\infty^3 \mathrm{d}A_\mathrm{D}} = 4a'(1-a)\lambda_r^2, \tag{2.21}$$

which are defined as the ratios of the energy extracted by the annular disc and the available energy of the undisturbed flow passing through the same area as the annular disc, where $\lambda_r = r\Omega/U_\infty$ is the local speed ratio.

Based on the general momentum theory, the axial and rotational induction factors as a function of radius for an ideal propeller with minimum energy loss due to wake rotation were approximated by Glauert (1935). This study modifies Glauert's approach by considering the energy conversion direction and derives approximate solutions for the wind turbine (Appendix A). Figure 2.2 depicts the maximum energy output of an ideal wind turbine rotor disc with minimum energy loss due to wake rotation and without any other energy loss in an incompressible flow. The local performance coefficients as a function of the local speed ratio show that the rotational induction coefficient is maximum at the rotor center and then decreases rapidly with the local speed ratio. In contrast, the axial induction factor and the local performance coefficients rapidly increase from zero at the rotor center and asymptotically approaching constant values. The general momentum theory derives that the overall rotor disc performs better and approaches Betz-limit at high tip speed ratios.

2.1.3 *The blade element momentum theory*

The momentum theory evaluates the wind turbine aerodynamic performance, but it does not indicate what kind of blade designs can achieve this result. The blade element method, which estimates forces experienced by the rotor blades directly, is an alternative way to predict the aerodynamic performance. The blade element momentum (BEM) method, which is the combination of the momentum theory and the blade element method, overcomes the disadvantage of the momentum theory.

The blade element method divides the rotor blade radially into many elements. Flows over an arbitrary blade element of a length $\mathrm{d}r$ at radius r (Fig. 2.3) are independent of those of neighboring elements. No induced radial velocity components occur over the blade element. Basically, the aerodynamic forces of the blade element are determined once the flow speed, the angle of attack, and the aerodynamic characteristics of the blade profile are known.

The flow speed over the blade element at the rotor plane is called the effective velocity which considers the induced axial and tangential velocities. According to the momentum theory, the axial velocity component of the flow at the rotor plane is $U_\infty(1-a)$, where a is the axial induction factor. The tangential velocity at the rotor plane, however, has not been specified yet in the general momentum theory (Sec. 2.1.2).

The tangential velocity at the rotor plane can be determined by observing the blade-bound circulation of the blade element, which induces an equivalent but opposite angular velocity $\pm\omega'$ immediately before and behind the rotor disc (Glauert 1935). The blade-bound circulations which leave the blade tips and blade roots further form a trailing vortex system. This trailing vortex system must induce an angular velocity ω' at the rotor plane in order to cancel the induced tangential velocity due to the blade-bound circulation immediately before the rotor disc. As a result, the total induced angular velocity immediately behind the rotor disc is $2\omega'$, which has to be equivalent to the induced angular velocity $2a'\Omega$ derived in the momentum theory. Thus, the angular velocity at the rotor plane is $\omega' = a'\Omega$. Consequently, the fluid's tangential velocity relative to the rotor blade at the rotor plane is $r\Omega(1+a')$.

The effective velocity of the flow over the blade element at the rotor plane

$$U_{\text{eff}} = \sqrt{(U_\infty(1-a))^2 + (r\Omega(1+a'))^2} \tag{2.22}$$

and the angle of attack

$$\alpha = \phi - \beta, \tag{2.23}$$

are determined, where the inflow angle

$$\phi = \tan^{-1}\left(\frac{U_\infty(1-a)}{r\Omega(1+a')}\right) = \tan^{-1}\left(\frac{1-a}{\lambda_r(1+a')}\right). \tag{2.24}$$

is the angle between the incoming flow and the rotor plane, and β is the angle between the blade chord and the rotor plane (Fig. 2.3).

For the blade element of a blade chord c in the fluid of density ρ, the lift of the blade element

$$\mathrm{d}L = \frac{1}{2} C_L \rho U_{\mathrm{eff}}^2 c \mathrm{d}r \tag{2.25}$$

and the drag of the blade element

$$\mathrm{d}D = \frac{1}{2} C_D \rho U_{\mathrm{eff}}^2 c \mathrm{d}r \tag{2.26}$$

are determined, where C_L and C_D imply the lift and drag coefficients, respectively. By decomposing the lift and drag into axial and tangential components (Fig. 2.4), the local thrust coefficient

$$C_T = \sigma(C_L \cos\phi + C_D \sin\phi)\frac{U_{\mathrm{eff}}^2}{U_\infty^2} \tag{2.27}$$

and the local torque coefficient

$$C_Q = \sigma(C_L \sin\phi - C_D \cos\phi)\frac{U_{\mathrm{eff}}^2}{U_\infty^2}, \tag{2.28}$$

based on the forces experienced by the blade element are obtained, where B is the numbers of blades and

$$\sigma = \frac{Bc}{2\pi r} \tag{2.29}$$

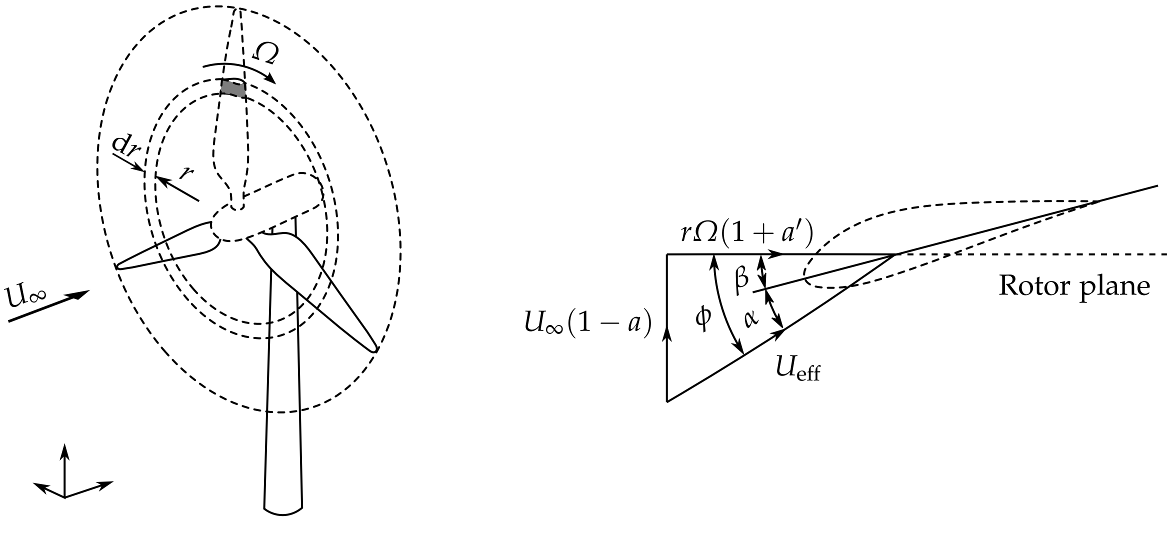

Figure 2.3: Velocity components experienced by a blade element of a horizontal axis wind turbine

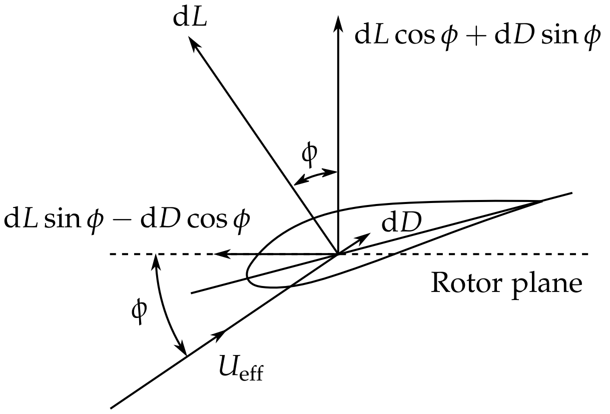

Figure 2.4: Decomposition of the lift and drag on the blade element in the axial and tangential directions

is the local blade solidity.

The BEM method suggests that the aerodynamic loads determined by the blade element method are equivalent to those determined by the momentum theory, thus the axial induction factor is obtained from Eq. (2.19) and Eq. (2.27)

$$a = \frac{1}{\dfrac{4\sin^2\phi}{\sigma C_\mathrm{n}} + 1}, \tag{2.30}$$

where $C_\mathrm{n} = C_L \cos\phi + C_D \sin\phi$. The effective velocity in Eq. (2.27) is replaced by $U_\mathrm{eff} = U_\infty(1-a)/\sin\phi$. Similarly, the rotational induction factor is determined from Eq. (2.20) and Eq. (2.28)

$$a' = \frac{1}{\dfrac{4\sin\phi\cos\phi}{\sigma C_\mathrm{t}} - 1}, \tag{2.31}$$

where $C_\mathrm{t} = C_L \sin\phi - C_D \cos\phi$. One of the effective velocities in Eq. (2.28) is replaced by $U_\mathrm{eff} = U_\infty(1-a)/\sin\phi$ and the other by $U_\mathrm{eff} = r\Omega(1+a')/\cos\phi$.

The azimuthally uniform flow field assumed in the momentum theory contradicts the reality because the discrete rotor blades induce azimuthally distributed flow fields and lead to tip/root loss. The tip/root loss is usually considered in the BEM method by employing Prandtl's loss correction factor

$$F = \frac{2}{\pi}\cos^{-1}(e^{-f}) \tag{2.32}$$

into the axial momentum equation

$$C_T = 4aF(1-a) \tag{2.33}$$

and tangential momentum equation

$$C_Q = 4a'F(1-a) \tag{2.34}$$

(Glauert 1935), where

$$f = \frac{B}{2}\frac{R-r}{r\sin\phi} \tag{2.35}$$

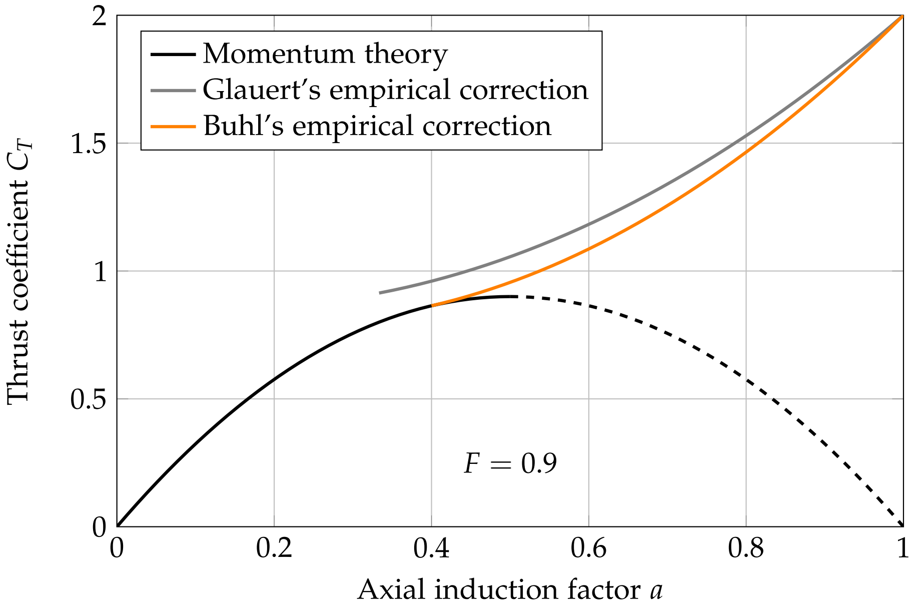

Figure 2.5: The discontinuity of Glauert's empirical correction in turbulent wake states when considering the tip loss correction factor

for the tip loss and

$$f = \frac{B}{2}\frac{r - R_{\text{root}}}{r \sin\phi}, \tag{2.36}$$

for the root loss. R_{root} is the root radius. The overall loss factor considering both the tip and root loss factors is superposed by $F = F_{\text{tip}}F_{\text{root}}$, where F_{tip} and F_{root} are tip and root loss factors, respectively. Thus, the axial and rotational induction factors considering the loss factors become

$$a = \frac{1}{\dfrac{4F\sin^2\phi}{\sigma C_{\text{n}}} + 1} \tag{2.37}$$

and

$$a' = \frac{1}{\dfrac{4F\sin\phi\cos\phi}{\sigma C_{\text{t}}} - 1}, \tag{2.38}$$

respectively.

As mentioned in Sec. 2.1.1, the momentum theory breaks down for $a \geq 0.5$ while the rotor operates in the turbulent wake state. Glauert measured the thrust coefficient in the turbulent wake state and observed that the thrust coefficients exceeded the limitation of the momentum theory. He proposed an empirical relationship fitting the measured data

$$C_T = 0.889 - \frac{0.0203 - (a - 0.143)^2}{0.6427} \tag{2.39}$$

for $a > 1/3$ (Buhl 2005). However, Buhl (2005) observed a discontinuity between Glauert's empirical relationship and the momentum theory when the tip loss correction factor is considered (Fig. 2.5). Buhl proposed another empirical relationship

$$C_T = \frac{8}{9} + \left(4F - \frac{40}{9}\right)a + \left(\frac{50}{9} - 4F\right)a^2 \tag{2.40}$$

for $a > 0.4$ to eliminate this numerical discontinuity (Fig. 2.5).

For a given operating condition and rotor design, the aerodynamic performance of the wind turbine can be calculated iteratively by the BEM method, see e. g. Hansen (2008).

2.1.4 *Determination of angle of attack using inverse BEM methods*

Angle of attack is defined in a 2D flow as the angle between the undisturbed incoming flow and the blade chord. This 2D definition is, however, inappropriate for the 3D flow over wind turbine blades because of induced axial and tangential velocities. Snel et al. (1994) adopted the definition of the angle of attack according to the BEM method as the angle between the effective incoming flow and the blade chord. The effective velocity of the effective incoming flow is the vectorial sum of the undisturbed wind speed, the blade rotational speed, and the induced velocity components. The undisturbed wind speed and the blade rotational speed can be easily measured in field experiments or evaluated from CFD results. The induced velocity components are, however, a challenge to determine.

The existing methods to determine the angle of attack of the 3D flow include the inverse BEM approach (Himmelskamp 1950, Snel et al. 1994, Lindenburg 2003, Bak et al. 2006, Guntur and Sørensen 2015), averaging technique (Hansen et al. 1997, Johansen and Sørensen 2004, Carcangiu et al. 2007, Herráez et al. 2014), bound vortex (Carcangiu et al. 2007, Shen et al. 2009, Vladimir et al. 2012), and the stagnation angle methods (Ronsten 1992, Brand et al. 1997). The inverse BEM method which solves the induction factors is used in this study to determine the angle of attack of the 3D flow.

In contrast to the BEM method which evaluate the wind turbine performance coefficients such as the power coefficient after iteratively solving the momentum equations, the inverse BEM method requires the performance coefficients as basic input information so as to evaluate the induction factors. The wind turbine performance, namely the local thrust coefficient

$$C_T = \frac{B \Delta F_\mathrm{a}}{\frac{1}{2}\rho U_\infty^2 2\pi r \Delta r} \tag{2.41}$$

and local torque coefficient

$$C_Q = \frac{B \Delta F_\mathrm{t} r}{\frac{1}{2}\rho U_\infty^2 2\pi r^2 \Delta r} \tag{2.42}$$

of a rotor with B number of blades are determined by the axial force ΔF_a and tangential force ΔF_t of a blade section of a length Δr. By substituting the known performance coefficients into the momentum equations (Eq. 2.19 and Eq. 2.20), the induced velocities and the angle of attack are obtained.

The iteration steps of the inverse BEM method implemented in this study are based on the approach of Snel et al. (1994) and Lindenburg (2003). First, an initial guess for the axial induction factor, rotational induction factor, and Prandtl's loss correction factor has to be specified, e. g., $a = a' = 0$ and $F = 1$. Then,

1. Evaluate the inflow angle using Eq. (2.24).

2. Evaluate the Prandtl's loss correction factor using Eq. (2.32).

3. Evaluate the new axial induction factor using Eq. (2.33) or the empirical relationship such as Eq. (2.40) when $C_T > C_T(a = 0.4, F)$.

4. Evaluate the new rotational induction factor using Eq. (2.34).

5. Check the relative differences between the new and old induction factors. If the convergence criterion are reached, break the iteration loop and calculate the angle of attack using Eq. (2.23); otherwise go back to step 1 and repeat the iterations.

2.2 3D BOUNDARY LAYERS ON ROTATING BLADES

The governing equations of the 3D boundary layer on a rotating blade are analyzed here in order to estimate the dominant parameters which may be responsible for the 3D effect due to rotation on the boundary layer properties and aerodynamic characteristics. A rotating reference frame attached to a steadily rotating blade is used. The choice of coordinate systems is between either the Cartesian coordinates, e. g., Fogarty (1951), Shen and Sørensen (1999), or the cylindrical coordinates, e. g., Banks and Gadd (1963), Snel et al. (1994). The cylindrical coordinates are chosen in this study since the 3D effect involves changes in radial components (Sec. 1.2.3). The origin of the coordinates is at the center of rotation. The velocity components in directions θ, r, z are v_θ, v_r, v_z, respectively (Fig. 2.6).

The steady, incompressible flow over the rotating blade in the cylinder coordinate system is expressed by the continuity equation

$$\frac{1}{r}\frac{\partial v_\theta}{\partial \theta} + \frac{\partial v_r}{\partial r} + \frac{\partial v_z}{\partial z} + \frac{v_r}{r} = 0, \tag{2.43}$$

θ-momentum equation

$$\begin{aligned} \frac{v_\theta}{r}\frac{\partial v_\theta}{\partial \theta} + v_r\frac{\partial v_\theta}{\partial r} + v_z\frac{\partial v_\theta}{\partial z} + \frac{v_\theta v_r}{r} - 2\Omega v_r = \\ -\frac{1}{\rho}\frac{\partial p}{r\partial \theta} + \frac{\mu}{\rho}\left(\frac{\partial^2 v_\theta}{\partial r^2} + \frac{\partial v_\theta}{r\partial r} + \frac{\partial^2 v_\theta}{r^2\partial \theta^2} + \frac{\partial^2 v_\theta}{\partial z^2}\right), \end{aligned} \tag{2.44}$$

r-momentum equation

$$\begin{aligned} \frac{v_\theta}{r}\frac{\partial v_r}{\partial \theta} + v_r\frac{\partial v_r}{\partial r} + v_z\frac{\partial v_r}{\partial z} - \frac{v_\theta^2}{r} + 2\Omega v_\theta - r\Omega^2 = \\ -\frac{1}{\rho}\frac{\partial p}{\partial r} + \frac{\mu}{\rho}\left(\frac{\partial^2 v_r}{\partial r^2} + \frac{\partial v_r}{r\partial r} + \frac{\partial^2 v_r}{r^2\partial \theta^2} + \frac{\partial^2 v_r}{\partial z^2}\right), \end{aligned} \tag{2.45}$$

and z-momentum equation

$$\frac{v_\theta}{r}\frac{\partial v_z}{\partial \theta} + v_r\frac{\partial v_z}{\partial r} + v_z\frac{\partial v_z}{\partial z} = -\frac{1}{\rho}\frac{\partial p}{\partial z} + \frac{\mu}{\rho}\left(\frac{\partial^2 v_z}{\partial r^2} + \frac{\partial v_z}{r\partial r} + \frac{\partial^2 v_z}{r^2\partial \theta^2} + \frac{\partial^2 v_z}{\partial z^2}\right), \tag{2.46}$$

where v_r/r, $v_\theta v_r/r$ and v_θ^2/r are coordinate curvature terms due to the choice of the cylindrical coordinates; $2\Omega v_r$ and $2\Omega v_\theta$ are Coriolis acceleration terms; $r\Omega^2$ is the centrifugal acceleration.

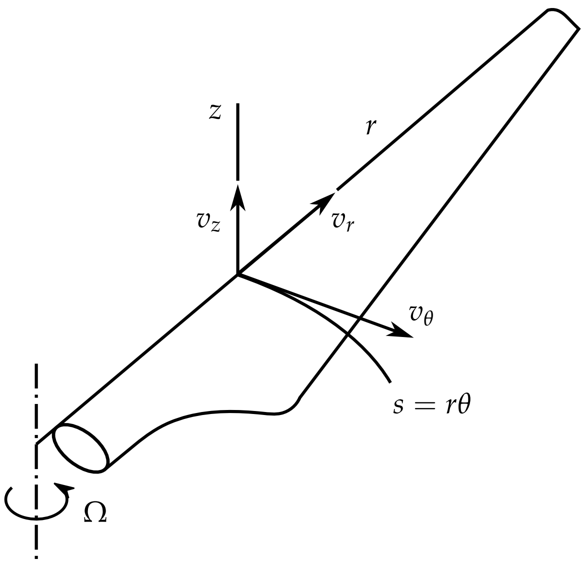

Figure 2.6: Coordinates system attached to a rotating blade. Adapted from "Sectional prediction of lift coefficients on rotating wind turbine blades in stall" by Snel, Houwink and Bosschers, 1994, Technical report ECN-C–93-052. Copyright 1994 by the Energy research Center of the Netherlands (ECN). Adapted with permission.

The occurrence of the centrifugal acceleration over the rotating wind turbine blade is similar to that over a rotating disc as described in Sec. 1.2.3. The appearance of the Coriolis acceleration is only a consequence of the choice of the non-inertial rotating reference frame. The chordwise Coriolis acceleration term plays a decisive role in the profile aerodynamic characteristics, once significant radial velocity components are induced.

The order of magnitude of each term in the governing equations is examined in this study, in order to estimate the dominant parameters in the boundary layer on the rotating blades. For the attached boundary layer, the boundary layer equations are directly used for the order of magnitude analysis (Sec. 2.2.1). For the detached boundary layer, the order of magnitude analysis of Snel et al. (1994) and Corten (2001) model are introduced in Sec. 2.2.2 and Sec. 2.2.3, respectively. Snel et al. (1994) used the boundary layer equations for the order of magnitude analysis by considering the different flow features of the detached flow. Corten (2001), however, dealt with the full set of Navier-Stokes equations because of the invalidity of the boundary layer theory for the flow separation, and proposed a model by neglecting relative small terms.

In the order of magnitude analysis, each equation is divided by a factor which makes the dominant terms, or so-called leading terms, become of the order of 1, i. e., $\mathcal{O}(1)$. The choice of the leading terms is important and decisive in the order of magnitude analysis. The chordwise coordinate $r\theta$ is scaled by the chord length c. The radial coordinate r is scaled by the local radius r. Thus, the azimuthal angle θ is equivalently scaled by the chord-to-radius ratio c/r. The choice of the reference velocities for the attached and separated flow is different, and is described in the following sections, respectively.

2.2.1 *Order of magnitude analysis of attached boundary layers*

The 3D boundary layer equations considering the boundary layer approximations are formulated as followed, see e. g., Fogarty (1951),
continuity equation:

$$\frac{1}{r}\frac{\partial v_\theta}{\partial \theta} + \frac{\partial v_r}{\partial r} + \frac{\partial v_z}{\partial z} + \frac{v_r}{r} = 0, \tag{2.47}$$

θ-momentum equation:

$$\frac{v_\theta}{r}\frac{\partial v_\theta}{\partial \theta} + v_r\frac{\partial v_\theta}{\partial r} + v_z\frac{\partial v_\theta}{\partial z} = -\frac{1}{\rho}\frac{\partial p}{r\partial \theta} + \frac{\mu}{\rho}\frac{\partial^2 v_\theta}{\partial z^2} + \frac{v_r}{r}(2r\Omega - v_\theta), \tag{2.48}$$

r-momentum equation:

$$\frac{v_\theta}{r}\frac{\partial v_r}{\partial \theta} + v_r\frac{\partial v_r}{\partial r} + v_z\frac{\partial v_r}{\partial z} = -\frac{1}{\rho}\frac{\partial p}{\partial r} + \frac{\mu}{\rho}\frac{\partial^2 v_r}{\partial z^2} + \frac{(v_\theta - r\Omega)^2}{r}, \tag{2.49}$$

z-momentum equation:

$$\frac{\partial p}{\partial z} = 0, \tag{2.50}$$

where the coordinate curvature term and Coriolis term in the θ-momentum equation are combined together as a total chordwise Coriolis acceleration, $v_r(2r\Omega - v_\theta)/r$. The coordinate curvature term, Coriolis term, and the centrifugal term in the r-momentum equation are combined together as a total circumpolar velocity $(v_\theta - r\Omega)$ responsible for the total centrifugal acceleration (Snel et al. 1994).

The definition of the total centrifugal acceleration explicitly shows that the maximal total centrifugal force occurs at the wall of a rotating flat disc, and approaches zero at the edge of the boundary layer. Similarly, considering the flow acceleration on the suction side of a rotating profile, the zero total centrifugal acceleration occurs in the boundary layer rather than at the edge of the boundary layer. The maximum total centrifugal acceleration occurs at the profile surface when the circumferential velocity of the external free stream is less than $2r\Omega$. The maximum total centrifugal acceleration occurs at the edge of the boundary layer when the circumferential velocity of the external free stream is higher than $2r\Omega$.

Because of the dominant chordwise flow motion, the chordwise convective term is chosen as the leading term, i. e., $v_\theta \partial v_\theta / r\partial\theta$ is the leading term of the θ-momentum equation. The chordwise velocity in the boundary layer is dominated by the external free stream (Fogarty 1951). The external flow velocity which varies along the blade chord is of the same order as the effective velocity of the flow passing over the blade section at the rotor plane. According to the BEM method (Eq. 2.22), the effective velocity is reformulated as

$$U_{\text{eff}} = r\Omega g, \tag{2.51}$$

where $g = U_{\text{eff}}/r\Omega$ is the ratio of the effective velocity of the flow and the circumferential velocity of the blade section. This velocity ratio approaches one at high local speed ratios, particularly near the blade tip. Eq. (2.51) indicates that the effective velocity is approximately of $\mathcal{O}(r\Omega)$. Thus, the chordwise velocity in the boundary layer

$$v_\theta = \mathcal{O}(r\Omega) \tag{2.52}$$

is scaled with $r\Omega$.

Based on Bernoulli's equation, the pressure is scaled with $(r\Omega)^2$ which leads to the pressure gradient in the θ-momentum equation of the same order as the leading term $v_\theta \partial v_\theta / r\partial\theta$. The pressure gradient in radial direction is of $\mathcal{O}(r\Omega^2)$.

The order of the magnitude of the pressure gradient in the radial direction can be alternatively approximated by considering the profile pressure coefficient (Snel et al. 1994). The pressure coefficient of the rotating blade section is defined as

$$C_p = \frac{p - p_{\text{ref}}}{\dfrac{1}{2}\rho U_{\text{eff}}^2} \tag{2.53}$$

where the static pressure of the undisturbed free stream is chosen as the reference pressure, namely $p_{\text{ref}} = p_\infty$. Thus, the pressure gradient in the radial direction in terms of the pressure coefficient is derived

$$\frac{\partial p}{\rho \partial r} = r\Omega^2 g^2 \left(C_p + \frac{r}{2}\frac{\partial C_p}{\partial r} + C_p \frac{r}{g}\frac{\mathrm{d}g}{\mathrm{d}r} \right). \tag{2.54}$$

At the blade section far away from the rotor axis, the pressure coefficient gradient and the velocity ratio gradient are negligible. Thus, the approximate order of magnitude of the radial pressure gradient is obtained, $\partial p/\rho\partial r \approx r\Omega^2 C_p = \mathcal{O}(r\Omega^2)$, similar to that obtained from Bernoulli's equation.

Because the radial convective motion is substantially driven by the total centrifugal force and the pressure gradient in the radial direction, the leading term in the r-momentum equation should be of the same order as them, i. e.,

$$\frac{v_\theta}{r}\frac{\partial v_r}{\partial \theta} = \mathcal{O}(r\Omega^2). \tag{2.55}$$

Equation (2.52) and Eq. (2.55) yields $v_r = \mathcal{O}(c\Omega)$. Moreover, the shear stress terms and the convective acceleration normal to the wall in the momentum equations are of the same order of magnitude according to boundary layer approximations.

The order of magnitude analysis of the continuity equation

$$\underset{(1)}{\frac{1}{r}\frac{\partial v_\theta}{\partial \theta}} + \underset{\left(\frac{c}{r}\right)^2}{\frac{\partial v_r}{\partial r}} + \underset{(1)}{\frac{\partial v_z}{\partial z}} + \underset{\left(\frac{c}{r}\right)^2}{\frac{v_r}{r}} = 0, \tag{2.56}$$

θ-momentum equation

$$\underset{(1)}{\frac{v_\theta}{r}\frac{\partial v_\theta}{\partial \theta}} + \underset{\left(\frac{c}{r}\right)^2}{v_r \frac{\partial v_\theta}{\partial r}} + \underset{(1)}{v_z \frac{\partial v_\theta}{\partial z}} = -\underset{(1)}{\frac{1}{\rho}\frac{\partial p}{r\partial \theta}} + \underset{(1)}{\frac{\mu}{\rho}\frac{\partial^2 v_\theta}{\partial z^2}} + \underset{\left(\frac{c}{r}\right)^2}{\frac{v_r}{r}(2r\Omega - v_\theta)}, \tag{2.57}$$

and r-momentum equation

$$\underset{\left(\frac{c}{r}\right)}{\frac{v_\theta}{r}\frac{\partial v_r}{\partial \theta}} + \underset{\left(\frac{c}{r}\right)^3}{v_r \frac{\partial v_r}{\partial r}} + \underset{\left(\frac{c}{r}\right)}{v_z \frac{\partial v_r}{\partial z}} = -\underset{\left(\frac{c}{r}\right)}{\frac{1}{\rho}\frac{\partial p}{\partial r}} + \underset{\left(\frac{c}{r}\right)}{\frac{\mu}{\rho}\frac{\partial^2 v_r}{\partial z^2}} + \underset{\left(\frac{c}{r}\right)}{\frac{(v_\theta - r\Omega)^2}{r}} \tag{2.58}$$

is obtained, where the r-momentum equation is compared to the leading term $v_\theta \partial v_\theta / r\partial\theta$ of the θ-momentum equation. The order of magnitude analysis reveals several important facts: the radial momentum equation is basically of $\mathcal{O}(c/r)$ smaller than the predominant chordwise flow, and the chordwise Coriolis acceleration is of the order of $(c/r)^2$ smaller than the predominant chordwise flow. The effect of the pressure gradient in the radial direction and the total centrifugal acceleration relative to the chordwise flow is proportional to c/r, which implies the period of time for the flow passing over the blade.

For the blade sections away from the rotor axis, i. e., $c/r \ll 1$, all the terms equal and higher than the order of $(c/r)^2$ are negligible, which leads to a set of equations identical to that derived by Fogarty (1951). This set of equations shows that the chordwise flow is independent of the radial flow and the 3D boundary layer equations become 2D problems. As the total chordwise Coriolis term no longer effects the chordwise flow, the chordwise velocity distributions as well as separation positions are the same as under the 2D stationary conditions. The radial velocity component v_r can be solved separately from the r-momentum equation once the 2D chordwise velocity distribution is known.

For the blade sections near the rotor axis, i. e., $c/r \sim \mathcal{O}(1)$, the total chordwise Coriolis term in the θ-momentum equation becomes a decisive parameter. Positive total chordwise Coriolis terms accelerate the flow passing over the rotating blade; negative total chordwise Coriolis terms decelerate the flow passing over the rotating blade. Since it is expected to have a chordwise acceleration on the profile suction side and a chordwise deceleration on the pressure side, the total chordwise Coriolis terms on the profile suction and pressure sides should be positive and negative, respectively. In order to estimate the criterion of the total chordwise Coriolis term, the direction of the radial velocity has to be known first.

The direction of the radial flow is determined by the total centrifugal acceleration and the spanwise pressure gradient (Eq. 2.58). The total centrifugal acceleration on both the suction and pressure sides are positive. The spanwise pressure gradient is approximated here by neglecting the pressure coefficient gradient and the velocity ratio gradient in Eq. (2.54). Thus, negative pressure coefficients on the profile suction side lead to spanwise acceleration towards the blade tip. Similarly, positive pressure coefficients on the profile pressure side lead to spanwise acceleration towards the blade root. Since both the total centrifugal acceleration and the spanwise pressure gradient drive the flow on the profile suction side radially towards the blade tip, the induced radial velocity component is supposed to be positive. Considering an expected positive total chordwise Coriolis term in the θ-momentum equation and this positive radial velocity, a criterion of the chordwise velocity distribution on the profile suction is obtained, $v_\theta \leq 2r\Omega$.

Since the flow passing over the profile pressure side decelerates, the chordwise velocity is lower than that of the external free stream, which means that $2r\Omega - v_\theta > 0$. In order to obtain a negative total chordwise Coriolis term in the θ-momentum equation, the radial velocity component on the profile pressure side has to be negative. That is to say, the absolute value of the spanwise acceleration due to the spanwise pressure gradient must be higher than the total centrifugal acceleration, in order to obtain a negative radial velocity component. As a result of that the spanwise pressure gradient on the profile pressure side is partly balanced by the total centrifugal acceleration, the induced radial velocity component on the profile pressure side is much less than that on the profile suction side. Consequently, the 3D rotational effect on the profile pressure side is insignificant, agreeing with the results of former research such as Snel et al. (1994) and Chaviaropoulos and Hansen (2000).

2.2.2 *Snel's order of magnitude analysis of detached boundary layers*

The order of magnitude analysis of detached boundary layers was first proposed by Snel et al. (1994). They considered the very different flow features of detached flows in comparison with those of attached flows.

They assumed that the chordwise velocity in the flow separation region relative to that of the attached flow is very small

$$v_\theta \ll r\Omega. \tag{2.59}$$

In contrast to that the chordwise pressure gradient in the flow separation region of a 2D stationary airfoil is essentially zero, the chordwise pressure gradient of the detached flow over the rotating blade is assumed very small. Thus, the chordwise velocity is supposed to be mainly driven by the chordwise Coriolis acceleration

$$\frac{v_\theta}{r}\frac{\partial v_\theta}{\partial \theta} = \mathcal{O}(\Omega v_r). \tag{2.60}$$

Because of the assumption of the relative small chordwise velocity (Eq. 2.59), the coordinate curvature term $v_\theta v_r/r$ in the θ-momentum equation (Eq. 2.44) is also small relative to the Coriolis term $2\Omega v_r$.

In order to determine the orders of magnitude of the radial and chordwise velocities (Eq. 2.60), Snel et al. (1994) chose the chordwise acceleration in the radial direction as the leading term in the r-momentum equation and scaled it with the centrifugal acceleration

$$\frac{v_\theta}{r}\frac{\partial v_r}{\partial \theta} = \mathcal{O}(r\Omega^2). \tag{2.61}$$

Equation (2.59), Eq. (2.60), and Eq. (2.61) derive

$$v_\theta = \mathcal{O}(c^{2/3}r^{1/3}\Omega), \qquad v_r = \mathcal{O}(c^{1/3}r^{2/3}\Omega), \text{ and } \qquad v_r/v_\theta = \mathcal{O}(c/r)^{-1/3}. \tag{2.62}$$

The derived results imply that the radial velocity component v_r is much greater than the chordwise velocity v_θ for small values of c/r. Consequently, Snel's order of the magnitude analysis of the continuity equation

$$\underset{(1)}{\frac{1}{r}\frac{\partial v_\theta}{\partial \theta}} + \underset{\left(\frac{c}{r}\right)^{2/3}}{\frac{\partial v_r}{\partial r}} + \underset{(1)}{\frac{\partial v_z}{\partial z}} + \underset{\left(\frac{c}{r}\right)^{2/3}}{\frac{v_r}{r}} = 0, \tag{2.63}$$

θ-momentum equation

$$\underset{(1)}{\frac{v_\theta}{r}\frac{\partial v_\theta}{\partial \theta}} + \underset{\left(\frac{c}{r}\right)^{2/3}}{v_r\frac{\partial v_\theta}{\partial r}} + \underset{(1)}{v_z\frac{\partial v_\theta}{\partial z}} = \underset{(1)}{-\frac{1}{\rho}\frac{\partial p}{r\partial \theta}} + \underset{(1)}{\frac{\mu}{\rho}\frac{\partial^2 v_\theta}{\partial z^2}} - \underset{\left(\frac{c}{r}\right)^{2/3}}{\frac{v_\theta v_r}{r}} + \underset{(1)}{2\Omega v_r}, \tag{2.64}$$

and r-momentum equation

$$\begin{array}{cccccc} \frac{v_\theta}{r}\frac{\partial v_r}{\partial \theta} + & v_r\frac{\partial v_r}{\partial r} & + v_z\frac{\partial v_r}{\partial z} = & -\frac{1}{\rho}\frac{\partial p}{\partial r} + & \frac{\mu}{\rho}\frac{\partial^2 v_r}{\partial z^2} + & \frac{(v_\theta - r\Omega)^2}{r} \\ (1) & \left(\frac{c}{r}\right)^{2/3} & (1) & (1) & (1) & (1) \end{array} \tag{2.65}$$

of the detached boundary layer over rotating blades is obtained. Snel et al. (1994) commented that the rotational effect on the detached boundary layer is much stronger than that on the attached boundary layer. For small values of c/r, the terms of the order of $(c/r)^{2/3}$ can be neglected.

2.2.3 *Corten's order of magnitude analysis of detached boundary layers*

Because of the invalidity of the boundary layer theory near the onset of flow separation and in the flow separation region, Corten (2001) argued against Snel's order of magnitude analysis and proposed another model directly dealing with the full set of Navier-Stokes equations, which makes his model even valid for the detached flow. Based on the physics of detached boundary layers, viscous effects are neglected in Corten's model. Thus the Navier-Stokes equations become Euler types.

Because flows in the flow separation region, specifically in the bottom of the detached boundary layer, are nearly motionless in the chordwise direction, all the terms regarding the chordwise velocity except that in the continuity equation are assumed very small and negligible, i. e.,

$$v_\theta \approx 0 \tag{2.66}$$

and

$$v_\theta \frac{\partial v_\theta}{r\partial\theta} \approx v_r \frac{\partial v_\theta}{\partial r} \approx v_z \frac{\partial v_\theta}{\partial z} \approx 0. \tag{2.67}$$

Since the thickness of the detached boundary layer is approximately of the same order as the chord length, the coordinate normal to the wall, z, is scaled by c, and all the derivatives in the z direction except that in the continuity equation are neglected. The radial velocity along the blade chord is assumed approximately constant, thus

$$\frac{\partial v_r}{r\partial\theta} \approx 0. \tag{2.68}$$

The second term of the r-momentum equation (Eq. 2.45) is chosen by Corten (2001) as the leading term rather than the first term as done by Snel et al. (1994) (Eq. 2.61). Equation (2.66) suggests that the radial motion is substantially driven by the centrifugal force, thus this leading term should be of the same order as the centrifugal acceleration

$$v_r \frac{\partial v_r}{\partial r} = \mathcal{O}(r\Omega^2), \tag{2.69}$$

which leads to $v_r = \mathcal{O}(r\Omega)$. Subsequently, the orders of magnitude of the chordwise velocity component

$$v_\theta = \mathcal{O}(c\Omega) \tag{2.70}$$

and the velocity component normal to the wall

$$v_z = \mathcal{O}(c\Omega) \tag{2.71}$$

are obtained from the continuity equation (Eq. 2.43).

By neglecting these very small terms in the full set of Navier-Stokes equations, the detached flow over the rotating blade can be illustrated by the continuity equation

$$\frac{1}{r}\frac{\partial v_\theta}{\partial \theta} + \frac{\partial v_r}{\partial r} + \frac{\partial v_z}{\partial z} + \frac{v_r}{r} = 0, \tag{2.72}$$

θ-momentum equation

$$\frac{1}{\rho}\frac{\partial p}{r\partial \theta} = 2\Omega v_r, \tag{2.73}$$

and r-momentum equation

$$\frac{v_r \partial v_r}{\partial r} = -\frac{1}{\rho}\frac{\partial p}{\partial r} + r\Omega^2. \tag{2.74}$$

Equation (2.73) implies that the chordwise pressure gradient must occur in oder to balance the chordwise Coriolis acceleration due to the significant radial flows. The commonly observed triangular pressure distributions suggest that the radial velocity distributions are constant along the blade chord, agreeing with the assumption of Eq. (2.68). Since the induced triangular pressure distributions are responsible for the lift augmentation, the lift augmentation due to the 3D rotational effect on the detached boundary layer can be estimated from Eq. (2.73) once the radial velocity is known. Equation (2.74) suggests that the radial velocity is determined by the centrifugal acceleration and the spanwise pressure gradient. Corten (2001) estimated the spanwise pressure gradient by neglecting the second and third terms in Eq. (2.54), i. e.,

$$\frac{\partial p}{\rho \partial r} = r\Omega^2 C_p. \tag{2.75}$$

Substituting Eq. (2.75) into Eq. (2.74) gives

$$v_r = r\Omega\sqrt{1 - C_p}. \tag{2.76}$$

Corten considered a case that the pressure coefficient on the suction side of a rotating profile varies from -3 at the separation line to 0 at the trailing edge. He then obtained that the chordwise pressure coefficient gradient varies within

$$\frac{4}{r} < \frac{\partial C_p}{r\partial \theta} < \frac{8}{r}. \tag{2.77}$$

Sicot et al. (2008) chose an empirical value of $C_p = -1$ and derived an expression from Corten's model

$$\frac{\partial C_p}{r\partial \theta} = \frac{1}{r}\frac{4\sqrt{2}}{1 + \lambda_r^{-2}} \tag{2.78}$$

for the prediction of the chordwise pressure coefficient gradient in the flow separation region of a rotating profile. However, this semi-empirical relationship is inaccurate and deviates considerably from their experimental results (Sicot et al. 2008, Fig. 9).

2.2.4 *Pressure distributions in the flow separation regions of rotating blades*

Corten's model gives not only an accurate description of the flow behavior in the flow separation region but also a convincing explanation of the mechanism responsible for the 3D rotational effect. Furthermore, the lift augmentation caused by the triangular pressure distribution due to the 3D rotational effect is able to be estimated from the simplified governing equations, specifically Eq. (2.73) and Eq. (2.74). Although Corten (2001) and Sicot et al. (2008) attempted to predict the pressure distribution in the flow separation region, their prediction deviates considerably from the experimental measurements (Sicot et al. 2008, Fig. 9).

The author of this study supposes, that the inaccuracy of their prediction arises from the inaccurate prediction of the spanwise pressure gradient by using Eq. (2.75). This study thus estimates the spanwise pressure gradient directly Eq. (2.54) directly. The pressure coefficient in the flow separation region on the profile suction side, namely the first term in the parenthesis of Eq. (2.54), is negative. Since the pressure coefficient on the suction side near the rotor axis is usually lower than that away from the rotor axis, the spanwise pressure coefficient gradient, namely the second term in the parenthesis of Eq. (2.54), is supposed to be positive. Because the velocity ratio decreases with the radius, its radial gradient is negative. In consequence, the third term in Eq. (2.54) is positive. By considering all these terms, this study posits that Eq. (2.75) used by Corten (2001) and Sicot et al. (2008) overpredicts the effect of the spanwise pressure gradient, which eventually results in the inaccurate prediction of the radial velocity component and the chordwise pressure gradient.

This study suggests that the spanwise pressure gradient in the flow separation region of the rotating blade is very small and negligible

$$\frac{\partial p}{\rho \partial r} \approx 0. \tag{2.79}$$

Thus, the radial flow is only driven by the centrifugal force (Eq. 2.74) and

$$v_r = r\Omega. \tag{2.80}$$

Substituting Eq. (2.80) into Eq. (2.73) gives the circumferential gradient of the pressure coefficient as followed

$$\frac{\partial C_p}{r\partial \theta} = \frac{1}{r}\frac{4}{g^2}. \tag{2.81}$$

The derivation in the circumferential direction in Eq. (2.81) is then approximated to the derivation in the chord direction by

$$r\partial\theta \approx \cos\beta\,\partial x, \tag{2.82}$$

where β is the blade twist angle (Fig. 2.3 right). Substituting Eq. (2.82) into Eq. (2.81) gives the chordwise pressure coefficient gradient as followed

$$\frac{\partial C_p}{\partial (x/c)} = \frac{c}{r}\frac{4}{g^2}\cos\beta, \tag{2.83}$$

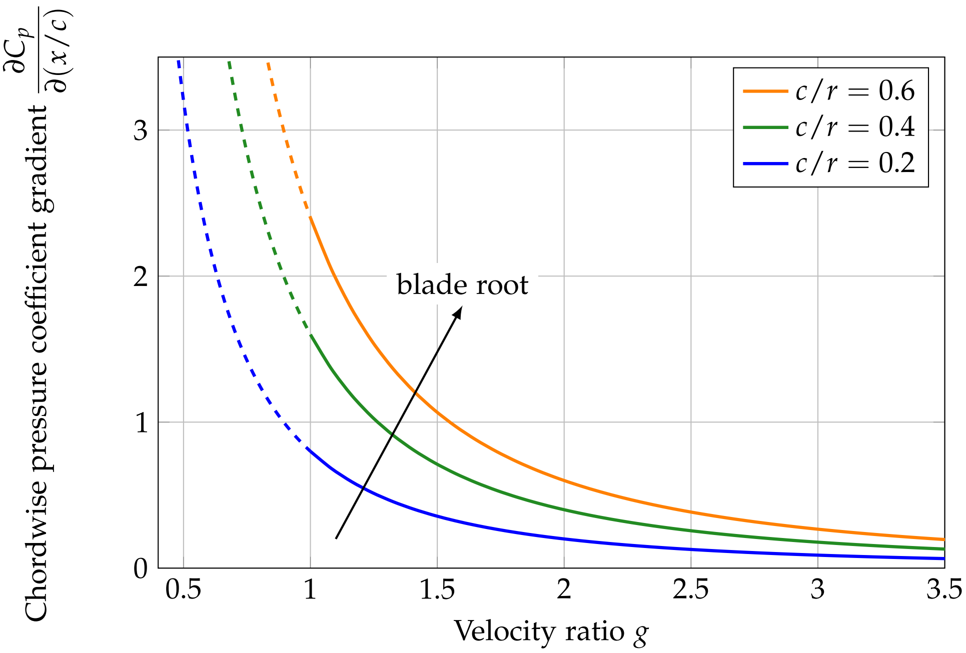

Figure 2.7: The chordwise pressure coefficient gradient in the flow separation region of a rotating profile as a function of the velocity ratio at various chord-to-radius ratios

where the chordwise coordinate x is normalized by the chord length. Since the blade twist angles along wind turbine blades is usually limited, Eq. (2.83) is further simplified as followed

$$\frac{\partial C_p}{\partial(x/c)} = \frac{c}{r}\frac{4}{g^2}. \tag{2.84}$$

The analytical expression Eq. (2.84) used in this study for the prediction of pressure distributions in the flow separation region of a rotating blade has two advantages. First, it is suitable for all types of blade profiles since no specific airfoils and no empirical coefficients are considered. Second, the operating conditions are considered in this analytical expression by the velocity ratio.

For an arbitrary blade section with known chord-to-radius ratio, the chordwise pressure coefficient gradient decrease with increasing velocity ratio (Fig. 2.7). Furthermore, the chordwise pressure coefficient gradient increases with the chord-to-radius ratio, namely approaching the blade root. Since the velocity ratio is higher than one, the curves in Fig. 2.7 for $g < 1$ are plotted with dashed lines. The analytical expression, Eq. (2.84), derived in this study for the prediction of pressure distributions in the flow separation region of rotating blades is verified in Sec. 4.3.2 by comparing with CFD results.

3

COMPUTATIONAL SETUP

This study conducts CFD computations, in order to capture the detailed flow field information over a horizontal axis wind turbine for the investigation of the inboard coherent structures and the 3D effect due to rotation. The computational setup introduced in this chapter is divided into four sections. The first section describes the geometries and the operating conditions of the baseline horizontal axis wind turbine. This is followed by an illustration of the 2D CFD computational setup for the determination of the profile aerodynamic characteristics and the BEM iterations. After that, the 3D CFD setup of the full-scale wind turbine with farfield boundaries is introduced. This section also demonstrates the determination of the streamtube coordinates and the inlet/outlet boundary conditions for the streamtube-based CFD models. The last section describes the CFD setup using these streamtube-based CFD models.

3.1 THE BASELINE WIND TURBINE

This study investigates the flow over the conceptual NREL offshore 5-MW baseline wind turbine of a rotor diameter of 126 m (Jonkman et al. 2009). The rated mechanical power of the baseline horizontal axis wind turbine at the rated wind speed $U_\infty = 11.4$ m/s and the rated rotor speed $\Omega = 12.1$ rpm is 5.30 MW. Its cut-in and cut-out wind speed is 3 m/s and 25 m/s, respectively. This baseline wind turbine is pitch-controlled. The blade pitch angle and the rotor speed vary with the operating conditions. For $U_\infty \leq 11.4$ m/s, the blade pitch angle is zero and the rotor speed varies from 6.9 rpm to 12.1 rpm. For $U_\infty \geq 11.4$ m/s, the rotor operates at the constant rotor speed of $\Omega = 12.1$ rpm, whereas the blade pitch angle varies with the operating conditions (Tab. 3.1). The rotor rotates clockwise when looking downstream.

The rotor blade of the NREL offshore 5-MW baseline wind turbine consists of various profiles (Tab. 3.2). Circular cross-sections are used at the blade root. A series of DU profiles whose thickness relative to their chord length varies from 40% to 21% are used in the inboard and

Table 3.1: The rotor control of the baseline wind turbine

Wind speed U_∞ in m/s	Rotor speed Ω in rpm	Pitch angle in °	Tip speed ratio λ	Note
8	9.16	0	7.55	
11.4	12.1	0	7.00	rated
15	12.1	10.45	5.32	
20	12.1	17.47	3.99	
25	12.1	23.47	3.19	

Table 3.2: The blade geometry of the NREL offshore 5-MW baseline wind turbine (Jonkman et al. 2009)

Rnode in m	Normalized radius r/R	Twist in °	Chord c in m	Chord-to-radius c/r	Pitch axis* -	Airfoil
2.000†	0.0317	0.000	3.542	1.77	0.500	Cylinder
2.867	0.0455	0.000	3.542	1.24	0.500	Cylinder
5.600	0.0889	0.000	3.854	0.688	0.468	Transition
8.333	0.132	0.000	4.167	0.500	0.442	Transition
11.75	0.187	13.31	4.557	0.388	0.403	DU40
15.85	0.252	11.48	4.652	0.294	0.375	DU35
19.95	0.317	10.16	4.458	0.223	0.375	DU35
24.05	0.382	9.011	4.249	0.177	0.375	DU30
28.15	0.447	7.795	4.007	0.142	0.375	DU25
32.25	0.512	6.544	3.749	0.116	0.375	DU25
36.35	0.577	5.361	3.502	0.096	0.375	DU21
40.45	0.642	4.188	3.256	0.080	0.375	DU21
44.55	0.707	3.125	3.010	0.068	0.375	NACA64618
48.65	0.772	2.319	2.764	0.057	0.375	NACA64618
52.75	0.837	1.526	2.518	0.048	0.375	NACA64618
56.17	0.892	0.863	2.313	0.041	0.375	NACA64618
58.90	0.935	0.370	2.086	0.035	0.375	NACA64618
61.63	0.978	0.106	1.419	0.023	0.375	NACA64618
62.90†	0.998	0.000	0.700	0.011	0.375	NACA64618

* The blade pitch axis is a dimensionless length from the blade leading edge to the pitch axis and is evaluated by converting the FAST notations given in Jonkman et al. (2009) to the actual notations

$$\text{BladePitch} - 0.25 = x_{\text{bp}} - x_{\text{ac}},$$

where the terms on the left and right sides are the FAST and actual notations, respectively. x_{ac} is the aerodynamic center, and x_{bp} is the actual blade pitch axis.

† From Bazilevs et al. (2011)

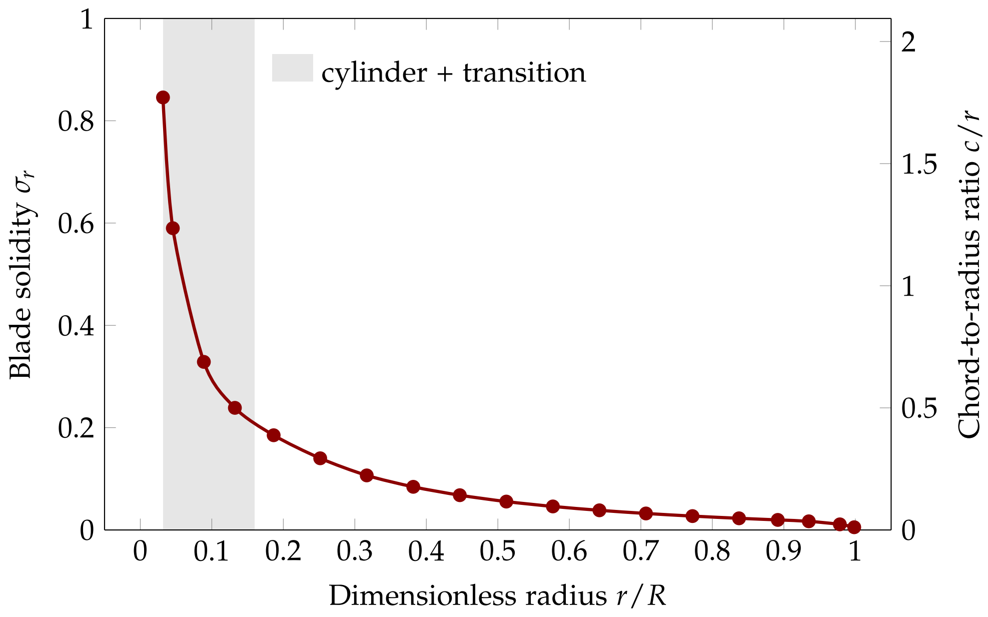

Figure 3.1: The geometrical properties of the baseline wind turbine

midspan region. NACA profiles with a relative thickness of 18% are used in the outboard region. The DU airfoils have blunt trailing edges. The blunt trailing edge thickness relative to the chord length varies from 0.39% to 0.69%, whereas the NACA airfoil has a sharp trailing edge. This sharp trailing edge of the NACA profile is modified into a blunt trailing edge with a relative thickness of 0.1% in order to simplify the mesh generation for the CFD computations.

According to the blade design and the profile coordinates (private communication with N. Timmer, M.Sc., Faculty of Aerospace Engineering, Delf University of Technology), a 3D computer-aided design (CAD) model of the rotor blade is constructed in Solid Edge (Fig. 3.2). The CAD rotor blade ignores the blade sections at Rnode $=$ 5.6 m and 8.3333 m in Tab. 3.2 and has a smooth geometry through all the other sections. Specific cylinder aerodynamic data, used in Jonkman et al. (2009), are also considered in the BEM iterations for these two transition blade sections. The baseline wind turbine has flat blade tips at Rnode $=$ 62.9 m according to the design by Bazilevs et al. (2011).

The baseline wind turbine used in this thesis has an elliptical (EL) spinner and a round-ended nacelle (Fig. 3.3). The spinner and nacelle have cylinder cross-sections when looking downstream. The spinner and nacelle are connected together smoothly. The maximum diameters of their cross-sections are 4.6 m. The total length of the nacelle and spinner of the baseline wind turbine is 17 m.

Due to the variety of the spinner forms used by the wind turbine industry, two other spinner geometries are also considered in this study in order to investigate their influences on the flow near blade roots. They are blunt elliptical (BE) and blunt conical (BC) spinners (Fig. 3.3). The blunt elliptical spinner is designed by trimming off the nose of the elliptical spinner. Thus, the BE spinner has a relative shorter length for the development of the boundary layer. The flow passing over the BE spinner is expected to be disturbed by the sharp edge of the trimmed nose. The blunt conical spinner is two times longer than the BE spinner. The BC spinner has a greater diameter of 5.2 m in order to cover the intersection of the three blade roots. The nacelle length of the BC spinner remains the same as the baseline wind turbine. The total length of the BC spinner and the nacelle is 18.88 m.

3.2 BEM ITERATIONS AND PROFILE AERODYNAMIC DATA

The BEM method is used in this study to evaluate the overall and local aerodynamic performance of the baseline wind turbine so as to identify the power overshoot due to the 3D rotational effect by comparing with the CFD results. The BEM iteration requires the profile aerodynamic data as basic input information. The aerodynamic coefficients of stationary airfoils are obtained in this study by conducting 2D CFD computations. This section consists of two subsections. First, the computational setup for the determination of the profile aerodynamic data is described in Sec. 3.2.1. The computational setup for the BEM iterations is subsequently presented in Sec. 3.2.2.

3.2.1 *Computational setup of 2D stationary profiles*

The aerodynamic data of the 2D stationary profiles used in the BEM iterations, are determined by conducting 2D CFD computations in the commercial CFD solver ANSYS CFX14.5. Since CFX provides only 3D solutions, some specific mesh topologies and boundary domain definitions are considered in order to conduct the 2D computations in the 3D solver. The mesh

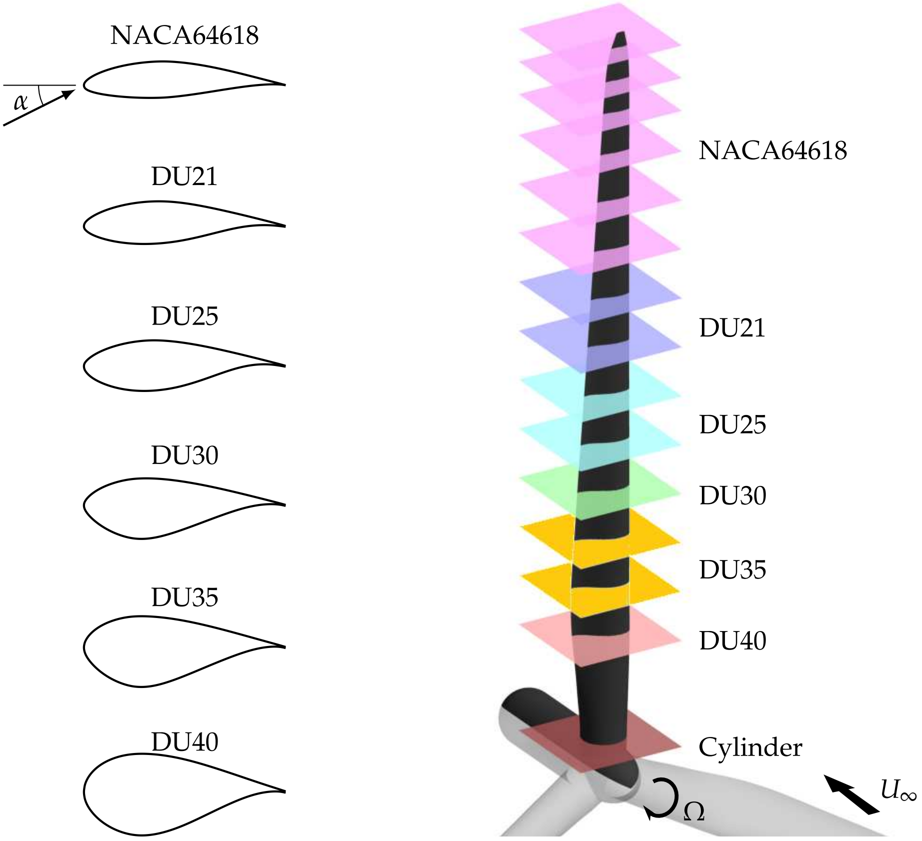

Figure 3.2: The composition of the baseline wind turbine blade

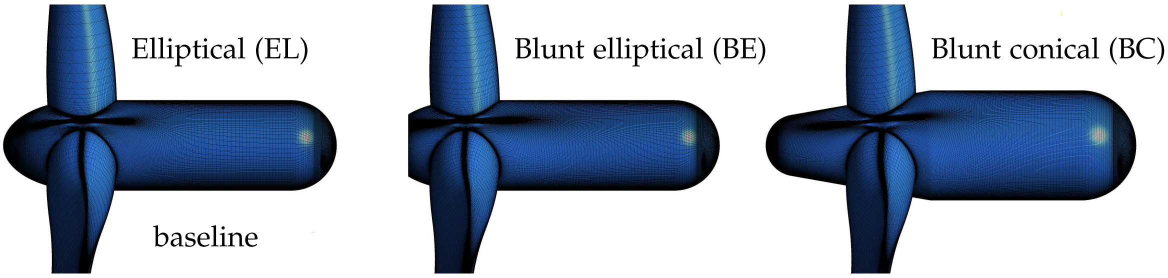

Figure 3.3: Various spinner designs of the baseline wind turbine

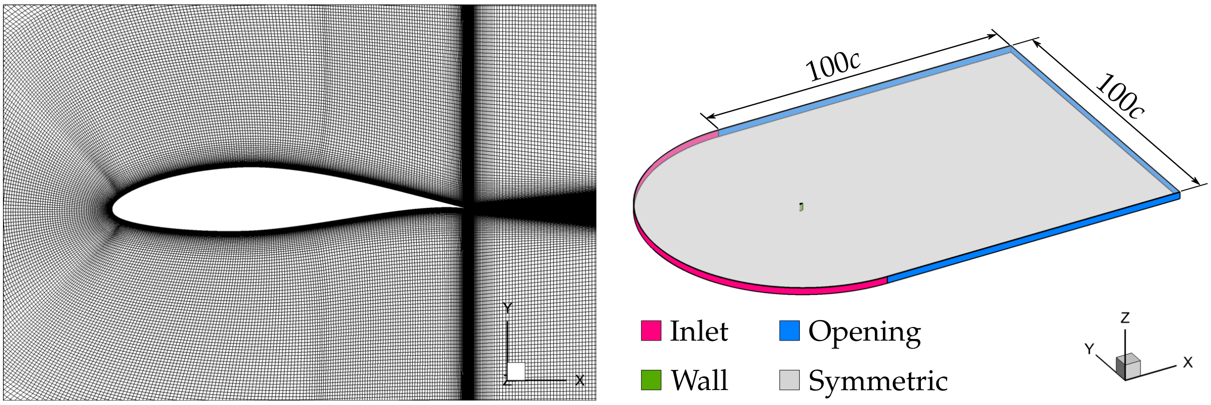

Figure 3.4: The hexahedral mesh grid (left) and boundary conditions (right) of the 2D CFD models for the determination of stationary aerodynamic characteristics

grids are generated in ICEM CFD with hexahedral structures (Fig. 3.4). The total number of elements in the chordwise direction of the profiles is 576. The dimensionless wall distance n^+ of the cell adjacent to the blade surface is less than 3. The cell height above the surface has an expansion ratio of 1.1. This mesh density and its quality are examined by a grid convergence index (GCI) study (Tab. 3.3). Its estimated, extrapolated relative error is less than 0.2%. Thus, the error caused by the mesh grid is under control and limited. The 2D mesh grid is generated in the xy-plane and then extrudes to the z-direction. There is only one element of thickness 0.1 m in the z-direction. The two boundaries parallel the z-plane are set to be symmetric. Using this mesh design and the symmetric boundary conditions, the computations are quasi 2D because all the components in z direction are zero. The half-circle-shaped inlet boundary is placed 50 chord lengths away from the trailing edge of the airfoil. The outlet boundary is placed 100 chord lengths downstream from the trailing edge.

The estimated chord Reynolds numbers

$$\mathrm{Re} = \frac{\rho U_\infty c}{\mu} \tag{3.1}$$

and Mach numbers

$$\mathrm{Ma} = \frac{U_\infty}{a_\mathrm{s}} \tag{3.2}$$

without considering the induced velocities (Fig. 3.5) show that the baseline wind turbine operate in subsonic flows at high Reynolds numbers of $\mathcal{O}(10^6) - \mathcal{O}(10^7)$, where μ is the dynamic viscosity and a_s is the sound speed. Thus, the 2D airfoils are chosen to be operated at the

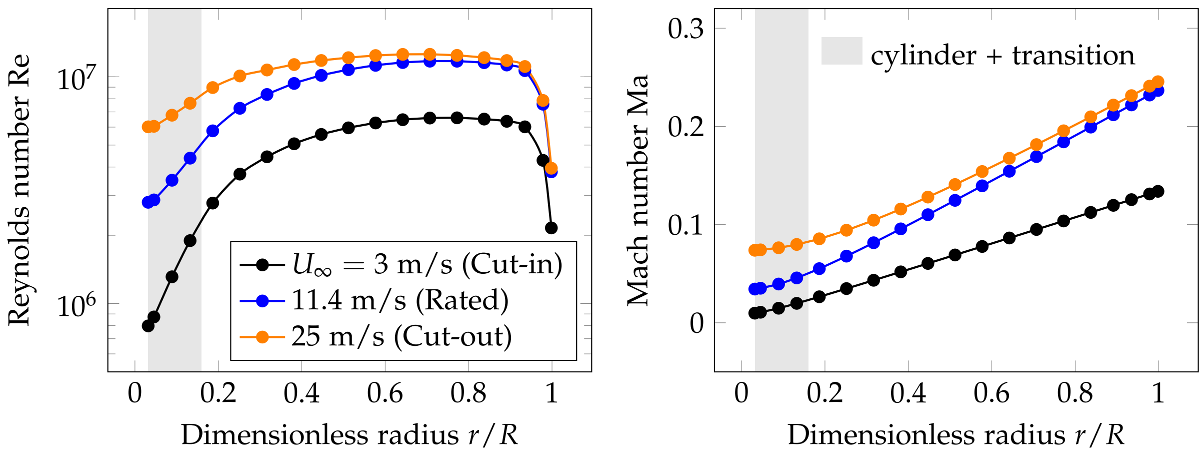

Figure 3.5: Estimated chord Reynolds number and Mach number of the baseline wind turbine without considering induced velocities

Reynolds number of $\mathrm{Re} = 7 \times 10^6$ in isothermal, incompressible air of density $\rho = 1.225$ kg/m^3. Menter's k-ω shear stress transport (SST) turbulence model is used, because it gives an accurate prediction of the onset and the amount of flow separation under adverse pressure gradients (Menter 1994). Since the airfoil operates at a super critical Reynolds number, the transition from laminar to turbulent boundary layer will occur very near the leading edge. Thus, no transition model is considered and fully turbulent boundary layer conditions are employed in all computations.

The angle of attack is controlled by changing the velocity components parallel and perpendicular to the chord at the inlet boundary where a a medium turbulence intensity of 5% is chosen. Angles of attack between −4° and 24° with steps of 2° are considered. The outlet boundary has a constant pressure of 101.325 kPa. The two boundaries parallel to the chord are in phase with each other. No-slip boundary condition is applied on the profile surface.

The flow passing over the airfoil at low angles of attack is attached and steady. In contrast, boundary layer separation occurs at high angles of attack, causing unsteady flow behavior and leading to numerical instability. Thus, for each angle of attack, steady RANS computations are conducted first. If flow separation occurs and leads to periodic aerodynamic loading, unsteady RANS computations are conducted subsequently. The time step of $\Delta t = 0.00125$ s is used in the unsteady computations where the aerodynamic coefficients are averaged over 10 periodic

Table 3.3: The grid independence study of the selected NACA64618 airfoil at $\alpha = 4°$ for the 2D CFD models (The conservative order of $p = 1$ and a safety factor of 1.25 are used.)

Nodes 10^3	C_L	C_D	$EERE_{C_L}$ %	$EERE_{C_D}$ %	GCI_{C_L} %	GCI_{C_D} %	Note
740	0.908	0.0117	0.49	2.88	−0.61	3.50	baseline
190	0.903	0.0120	0.98	5.75	−2.27	15.3	
47	0.887	0.0135	2.75	18.5	−4.51	30.4	

cycles. The steady and unsteady computations are stopped when the residual values less than the convergence criterion of 10^{-5}. The lift coefficient

$$C_L = \frac{L}{\frac{1}{2}\rho U_\infty^2 c} \tag{3.3}$$

and drag coefficient

$$C_D = \frac{D}{\frac{1}{2}\rho U_\infty^2 c} \tag{3.4}$$

of the 2D airfoils are then evaluated, where L and D are force components perpendicular and parallel to the undisturbed incoming flow, respectively. U_∞ is the velocity of the undisturbed free stream and c is the chord length.

3.2.2 *BEM iterations*

The BEM equations are solved iteratively in an in-house Matlab-code. The Matlab-code includes Buhl's empirical relationship and Prandtl's tip/root loss correction factors for the correction of the 3D effects due to turbulent wake states and end effects. No empirical correction model for the rotational augmentation is employed in the BEM computations. The BEM iteration stops when the variation of the axial and rotational induction factors are less than 10^{-5}. An under-relaxation factor is used to avoid numerical divergence. BEM iterations at all the operating conditions listed in Tab. 3.1 are conducted.

3.3 THE FARFIELD CFD MODELS

Steady CFD computations with farfield boundaries are conducted in order to capture the flow fields for the identification of inboard coherent structures and the preparation of the streamtube-based simplified CFD models.

Due to the periodicity of the three bladed rotor, only one rotor blade is considered in this study, i. e., 120° domain. Hexahedral mesh grids with O-grid topologies around the rotor blade are generated in ICEM CFD (Fig. 3.6). Two dimensionless cell heights adjacent to the blade surface of $n^+ \lesssim 2$ and $n^+ \lesssim 30$ are considered. Since the expansion ratio of the cell height normal to the blade surface is kept approximately constant of 1.1, the total number of mesh nodes of $n^+ \lesssim 2$ is 5% higher than that of $n^+ \lesssim 30$. However, the difference of the overall power output between them is less than 0.5%. The mesh grid of $n^+ \lesssim 30$ is thus chosen for the CFD computations with farfield boundaries, in order to reduce computational requirements and accelerate computations. Computations with three different levels of mesh grid are also conducted for the mesh independence study. The fine mesh, whose extrapolated relative error of the overall power coefficient is only approximate 0.1% (Tab. 3.4), is chosen for the computations, because it has also better resolution for capturing the vortical structures in the near wake. The blade of the baseline wind turbine is divided into 272 and 196 elements in the chordwise and spanwise directions, respectively.

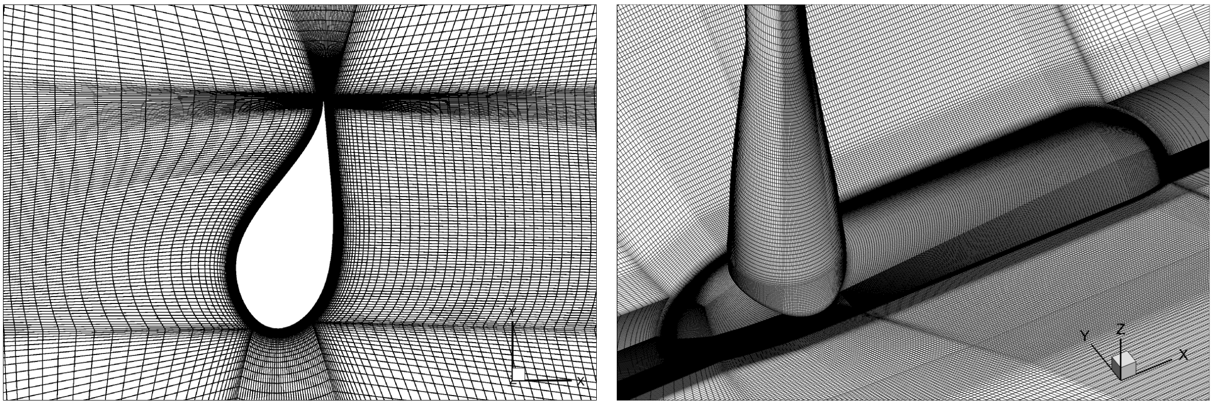

Figure 3.6: The hexahedral mesh grid of the blade section (left) and in the hub region of the farfield CFD models

The computational domain is divided into a rotational domain and a stationary domain in order to model the rotational motion of the rotor blades (Fig. 3.7). The total number of mesh nodes is 29.7×10^6, where the rotational domain has the most mesh nodes of 20.3×10^6 and the stationary domain only has 9.38×10^6 nodes. The rotational and stationary domains are connected by interfaces. The stationary domain is $60R$ and $20R$ wide in the streamwise and radial directions, respectively. The rotor is placed $20R$ downstream from the inlet boundary. The rotational domain is $3R$ and $1.5R$ wide in the streamwise and radial directions, respectively.

The steady CFD computations are conducted in ANSYS CFX14.5 where the same fluid properties and turbulence model as described in Sec. 3.2 are employed. The rotational domain has a constant angular velocity which depends on the operating conditions (Tab. 3.1). All the no-slip walls in the rotating domain rotate together with the rotating domain. This study simplifies the computational setup by neglecting the relative motion between the nacelle and spinner. Similar simplification by rotating the nacelle together with the rotor blades and spinner was also used by Johansen et al. (2006), Laursen et al. (2007), Rauch et al. (2007). Although the nacelle does not rotate in reality, its effect is limited and negligible because the shear induced by the slowly rotating nacelle only occurs near the nacelle surface, having no significant effect on the airfoil sections. The frozen rotor method is applied to the interfaces of the rotational and stationary domains. The inlet boundary has a uniform velocity distribution with a medium

Table 3.4: The grid independence study of the farfield CFD models at the rated operating conditions of $U_\infty = 11.4$ m/s (The conservative order of $p = 1$ and a safety factor of 1.25 are used.)

Nodes 10^6	C_P	C_T	$EERE_{C_P}$ %	$EERE_{C_T}$ %	GCI_{C_P} %	GCI_{C_T} %
29.7	0.475	0.739	0.11	0.01	-0.14	-0.01
12.0	0.474	0.739	0.15	0.01	-3.09	-1.44
3.75	0.469	0.735	1.32	0.62	-4.56	-2.12

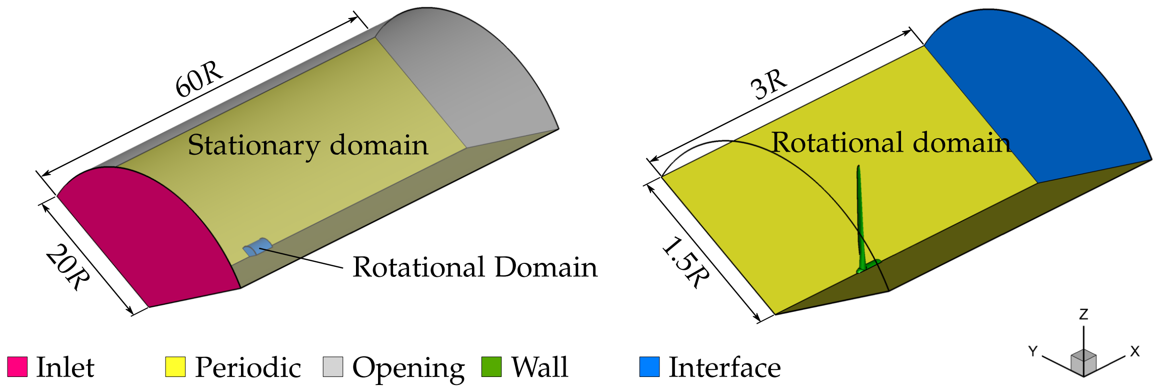

Figure 3.7: The boundary conditions of the 3D CFD models

turbulent intensity of 5%. The opening boundary condition has a static pressure of 101325 Pa. All the operating conditions listed in Tab. 3.1 are considered.

The computations reach convergence when the root mean square (RMS) values of residuals are less than 10^{-5}. However, this stop criterion is difficult to reach because of the occurrence of the unsteady von Kármán vortex street in the blade root region. Thus the computations stop when the mean power output and the mean thrust force of the rotor are stable. The total number of nodes with residual values higher than 10^{-3} is about 0.005%. The CFD setup is thus adequate for the steady computations.

3.4 THE STREAMTUBE-BASED SIMPLIFIED CFD MODELS

3.4.1 *Determination of streamtube coordinates*

Once the CFD computations using farfield boundaries have been conducted, the streamtube coordinates for the simplified models can be determined. An axisymmetric streamtube crossing through the blade midspan is considered, where the flow is fully attached and approximately two-dimensional (Fig. 3.8). This axisymmetric streamtube is generated by revolving a streamline passing through a selected start point (r, θ, x). The radial position of the start points is approximately two times the extent of the flow separation on the suction of the rotor blade. Here, $r = 45$ m is used. The start point is chosen at the azimuthal angle of $\theta = -40°$ and at the rotor plane of $x = 0$.

3.4.2 *Computational setup*

The mesh grids of the streamtube-based CFD models are generated in ICEM CFD by removing the outer blocks and re-associating the edges of the blocks to the curves of the computational domains. Thus, the mesh nodes of the simplified CFD models are almost identical to those of the farfield CFD models. The blade has an unchanged number of chordwise elements. The span-wise number of elements is reduced from 272 to 144. The computational domain is $3R$ in the axial direction. The rotor is placed $1R$ downstream from the inlet boundary. The

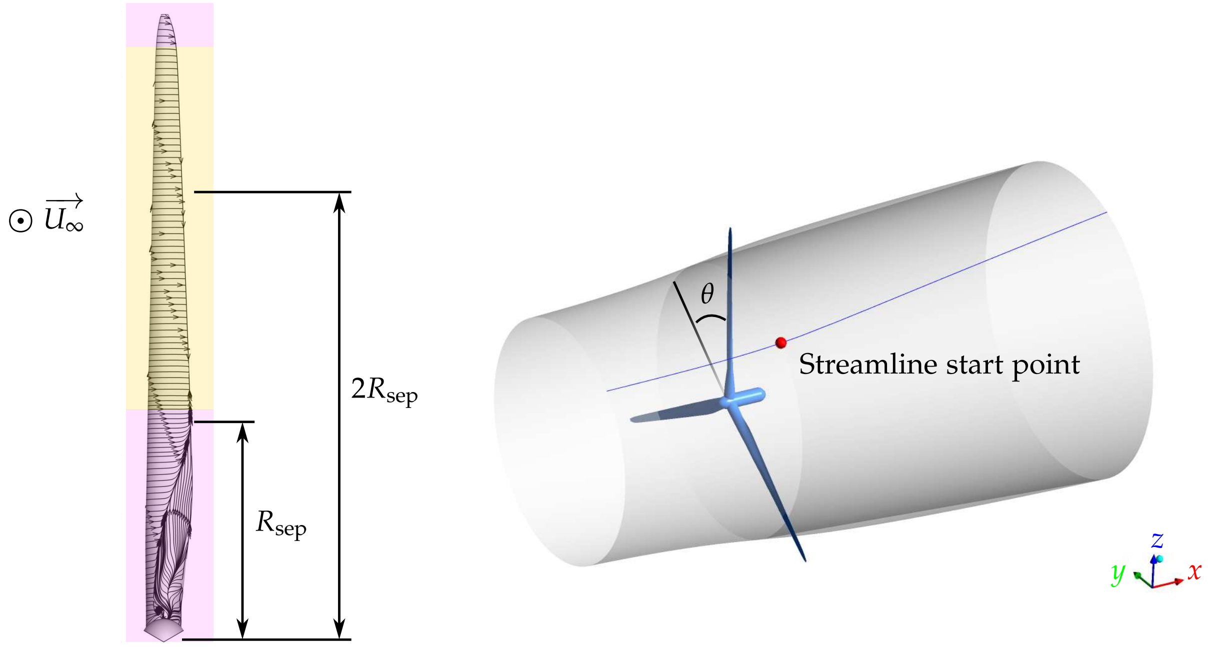

Figure 3.8: Determination of the streamtube coordinates

streamtube-based CFD models have a total number of mesh nodes of approximate 15.1×10^6.

The streamtube-based simplified model only has a rotational domain. The inlet boundary has a medium turbulence intensity and a nonuniform velocity distribution, which is determined by extracting the flow velocities at the same position from the farfield CFD results. The outlet boundary has a nonuniform pressure distribution which is similarly obtained from the farfield CFD results. Because the streamtubes are dependent on the operating conditions, every operating point has its own corresponding streamtube, mesh grids, and boundary conditions. Steady computations of the streamtube-based simplified CFD models are conducted and compared with the farfield CFD results so as to validate the streamtube-based simplified CFD models. The computations of the simplified CFD models using the mesh grids generated in ICEM CFD have similar difficulties as the farfield computations in reaching the convergence criteria. There are approximate 0.00003% nodes whose maximal residual values are higher than 10^{-3}.

Table 3.5: The grid independence study of the streamtube-based CFD models at the rated operating conditions of $U_\infty = 11.4$ m/s (The conservative order of $p = 1$ and a safety factor of 1.25 are used.)

Nodes	C_P	C_T	$EERE_{C_P}$	$EERE_{C_T}$	GCI_{C_P}	GCI_{C_T}	Note
10^6			%	%	%	%	
14.4	0.508	0.672	0.68	0.15	−0.85	−0.19	baseline
2.09	0.505	0.671	1.29	0.29	−24.8	−16.6	
0.27	0.407	0.583	20.5	13.3	−49.1	−32.9	

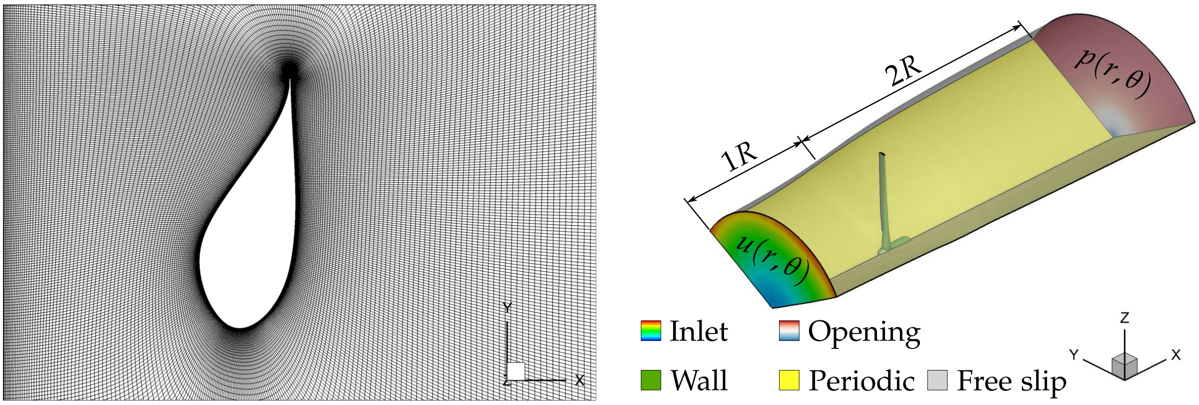

Figure 3.9: The mesh grid generated in AutoGrid5 (left) and the boundary conditions (right) of the streamtube-based CFD models

In order to improve the mesh quality and accelerate the meshing process, AutoGrid5 9.0-1 is used to generate the mesh grids for the streamtube-based simplified CFD models. AutoGrid5 provides many templates, which are called row wizards in AutoGrid5, for different turbomachines. The axial fan wizard is chosen to generate the mesh grids for the streamtube-based simplified models. The hub and shroud defined in the axial fan wizard correspond to the hub and the streamtube of the streamtube-based simplified models.

Computations with three different mesh densities are conducted for the grid independence study. The aerodynamic performance of the baseline wind turbine with different mesh densities and the corresponding grid convergence indexes are presented in Tab. 3.5. The finest mesh which has an estimated extrapolated errors of less than 0.7% is chosen for the simplified models. The blade in this mesh density is discretized into 353 and 129 elements in the chordwise and spanwise direction, respectively (Fig. 3.9). The dimensionless cell height n^+ adjacent to the blade surface is less than 2. The total number of mesh nodes for the simplified model using the mesh grids generated in AutoGrid is 14.4×10^6.

Since two meshing tools are used to generate the mesh grids of the streamtube-based models, the sensitivity of the aerodynamic performance to the mesh quality and the dimensionless cell height adjacent to the blade surface has to be identified. Steady computations of the streamtube-based CFD models using the mesh grids generated in ICEM CFD and AutoGrid are conducted. Figure 3.10 depicts the local performance coefficients of the baseline wind turbine at the rated wind speed of $U_\infty = 11.4$ m/s. The relative differences in the local performance coefficients between the computations using different meshing tools are also depicted in Fig. 3.10 with filled bars. Since the streamtube-based simplified CFD model only includes the domain up to $r = 45$ m, Fig. 3.10 shows the local performance coefficients only up to $r/R = 0.71$. The local performance coefficients of the model using the mesh generated in ICEM CFD is overall lower than those of AutoGrid5. Significant deviation occurs in the blade root region. Because the steady computation is unable to capture the unsteady von Kármán vortex shedding from the cylindrical and blunt blade roots, and the flow state is predominantly determined by the last iteration where the computation stops, the significant deviation in the blade root region is supposed to be caused by this reason. Thus, the sensitivity study focuses only on the positions of $r/R > 0.2$. The relative differences in the local power and

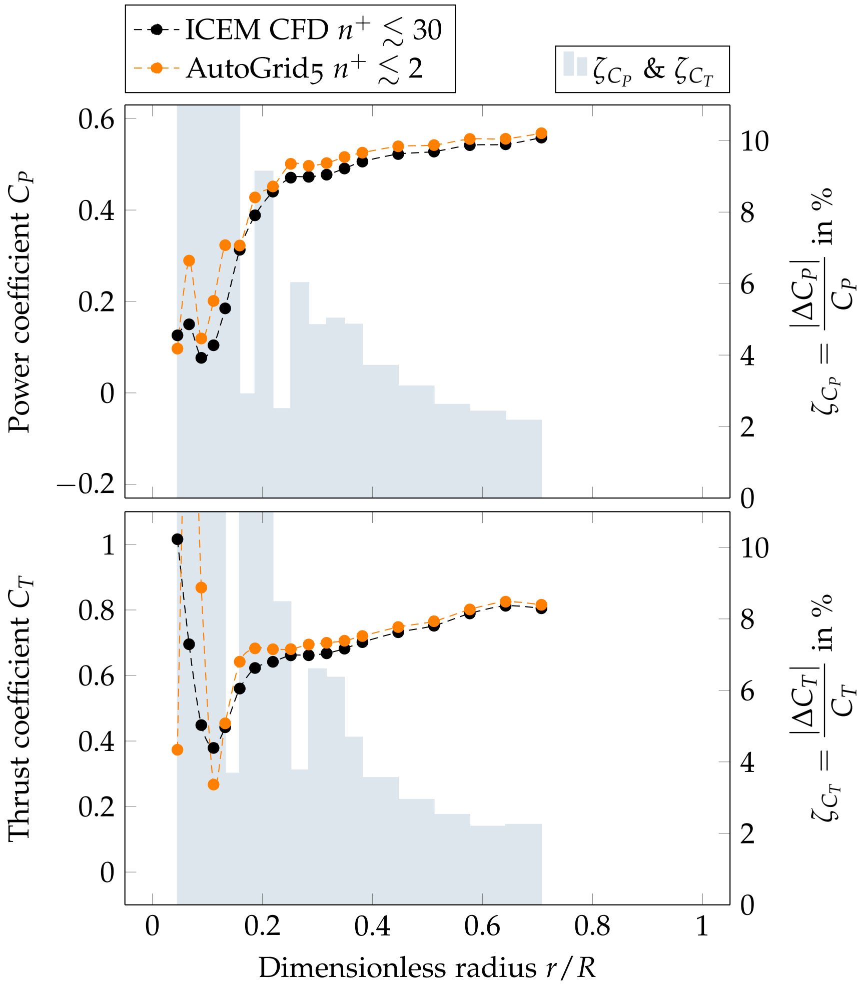

Figure 3.10: Sensitivity study of the local performance coefficients to the mesh quality and dimensionless cell height adjacent to the blade surface of the baseline wind turbine at $U_\infty = 11.4$ m/s by using different mesh tools

thrust coefficients except in the inboard region are within 2% and 6%. This manifests that the mesh quality and dimensionless cell height adjacent to the blade surface have only limited influence on the local aerodynamic performance.

Similar setups are used in the unsteady computations for the investigation of the rotational effects, as well as the influences of the spinner geometries on the flow near the blade roots. The results of steady computations are used as initial conditions. The timestep of the unsteady computation is 0.00138 sec in which the rotor rotates approximate 0.1°. This timestep results in an average Courant number of approximate 4 at $U_\infty = 11.4$ m/s and 20 m/s. The total simulation time is more than 7 revolutions. The variables such as velocity and pressure are averaged over the last four revolutions, while the fluid in the computational domain is completely exchanged by fresh fluid.

The streamtube-based CFD model only has a rotational domain which rotates at a constant rotational speed depending on the operating conditions (Tab. 3.1). The rotational motion of the wind turbine rotor in the simplified model is modeled by using the same method as applied in the farfield models, i. e., rotating all the no-slip walls together with the rotating

Table 3.6: Comparison of the cumulated aerodynamic performance of the baseline wind turbine up to $r = 40$ m/s using the farfield and simplified CFD models at $U_\infty = 11.4$ m/s

	P kW	T kN	$\lvert\Delta P\rvert / P$ %	$\lvert\Delta T\rvert / T$ %	Note
Farfield model	2217.23	286.52	-	-	baseline
Simplified model	2227.02	286.51	0.44	0.0024	

domain. The same fluid properties and turbulence model as used in the farfield computations are employed in the streamtube-based models. The inlet boundary conditions use the velocity distributions obtained from the farfield computations (Fig. 3.9). In a similar way, the opening boundary uses pressure distributions. Two selected operating conditions of $U_\infty = 11.4$ m/s and 20 m/ with the elliptical, blunt elliptical and blunt conical spinners are considered.

3.4.3 *Validation of the simplified CFD models*

This study proposes a streamtube-based simplified CFD model in order to reduce computational requirements and therefore accelerate the unsteady computations. By using the local velocity and pressure distributions as the inlet and outlet boundary conditions, and the free-slip wall as the boundary condition for the axisymmetric streamtube, the simplified CFD model is supposed to represent the flow field of the farfield model. For the purpose of validating the simplified CFD model, the aerodynamic performance and the flow structures of the based wind turbine of the simplified CFD model are compared with those of the farfield model in this section. The errors arisen by using the simplified CFD model are also presented here.

The simplified CFD model is identified by comparing two steady computations using the farfield and streamtube-based simplified CFD models. Both simulations use the mesh grids generated in ICEM CFD of the dimensionless cell height $n^+ \lesssim 30$. Table 3.6 presents the cumulated power and thrust on the baseline wind turbine using the farfield and simplified CFD models at the rated wind speed of $U_\infty = 11.4$ m/s. Because the simplified CFD model only considers the domain up to approximately $r = 45$ m, the aerodynamic performance presented in Tab. 3.6 cumulates only up to $r = 40$ m in order to identify the influence of using the simplified model on the overall aerodynamic performance. Table 3.6 explicitly shows that the relative errors of the overall aerodynamic performance arisen by using the simplified CFD model up to 0.44% are limited.

Although the overall errors arisen by using the simplified CFD model are limited, its effect on local aerodynamic performance and local flow structures is of interest to be further investigated. Figure 3.11 shows the local power and thrust coefficients of the baseline wind turbine using the farfield and simplified CFD models at the rated wind speed of $U_\infty = 11.4$ m/s. The differences in the local performance coefficients between the farfield and simplified CFD models are also depicted in Fig. 3.11 with filled bars. The local performance coefficients of the simplified CFD model in Fig. 3.11 present only up to $r/R = 0.71$ because the simplified model

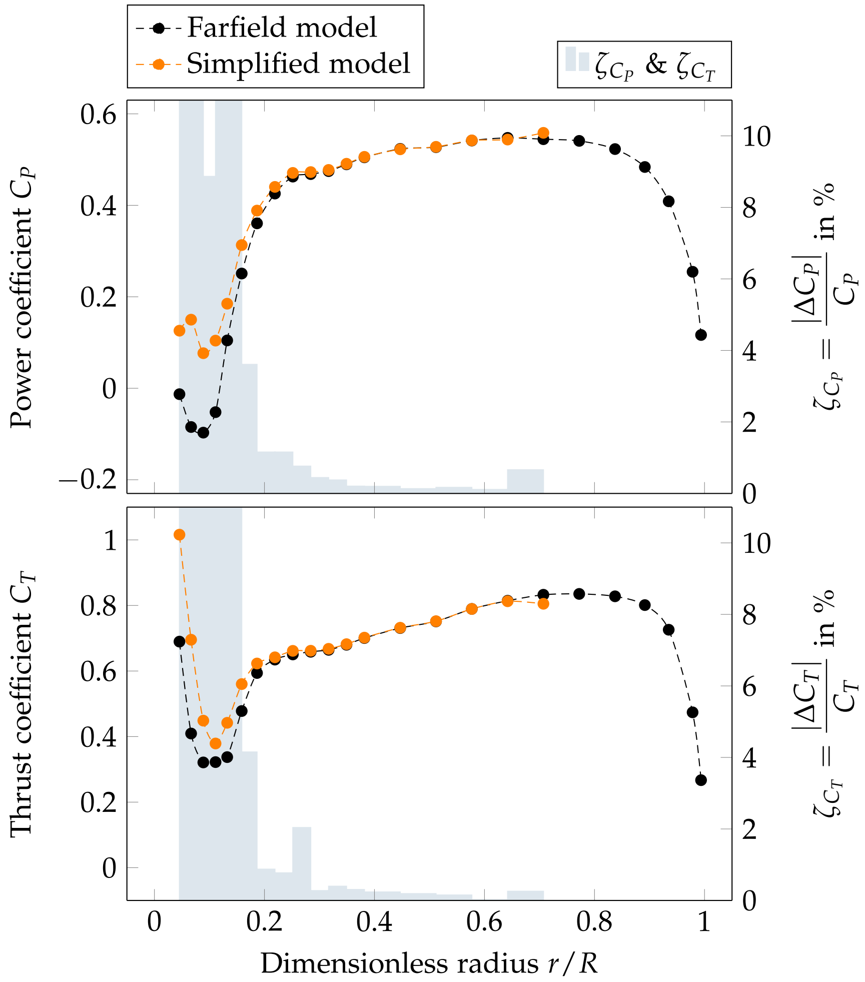

Figure 3.11: Comparison of the local performance coefficients of the baseline wind turbine using the farfield and simplified CFD models at $U_\infty = 11.4$ m/s

only considers the domain up to approximately $r = 45$ m. Figure 3.11 shows an overall good agreement between the simplified model and the farfield model except near the streamtube boundary and in the inboard region. The deviation near the blade roots is substantially caused by unsteady von Kármán vortices shedding from cylindrical blade roots. Due to the insufficient ability to capture the unsteady vortex shedding when using the RANS computations, the differences of the local performance coefficients between the farfield and simplified models are decisively dependent on the last iteration where the simulation stops. Thus, For the validation of the streamtube-based simplified CFD models, only the deviation near the streamtube boundary is of interest. Figure 3.11 shows that the deviation near the streamtube boundary is very limited. The deviation near the streamtube boundary abruptly vanishes at the radial position slightly away from the streamtube boundary. This observation manifests that the errors arisen by using the streamtube-based simplified model is limited and negligible for all the flow slightly away from the streamtube boundary. Thus, the streamtube-based simplified model is validated for the investigation of the flow near the blades roots of the baseline wind turbine.

4

RESULTS AND DISCUSSION

This study utilizes CFD methodology to capture the detailed flow fields over the baseline horizontal axial wind turbine. The computational results are presented and discussed in this chapter. This chapter is further divided into three sections, including the coherent structures near the blade roots, the effect of spinner geometry, and the 3D effect due to rotation.

4.1 COHERENT STRUCTURES NEAR THE BLADE ROOTS

4.1.1 *An overall description of velocity and pressure fields*

A preliminary understanding of the flow field over a horizontal axis wind turbine has been achieved through momentum theory (Sec. 2.1). The momentum theory adopts many assumptions which usually contradict the real flow conditions. With these assumptions, the BEM method loses accuracy in predicting wind turbine aerodynamic performance. This section aims to address the deficiency of the 2D flow fields assumed by the momentum theory. In order to do that, the complex flow field over the 3D baseline wind turbine is presented in the one-dimensional way, the same as the momentum theory. More specifically, the velocity and pressure fields are averaged over an annular plane at radius r of a thickness Δr. This annular plane moves along the rotor axis, in order to gather the flow variation along the rotor axis. The wake expansion is neglected by using this evaluation method, thus the flow through the annular planes at various axial positions is approximate to that through an annular shell. At the rotor plane, the flow is averaged over the effective annular area without the solid rotor blades. Considering the annular planes at different radii, an overall description of the complex flow is obtained (Fig. 4.1), where the wind turbine rotor plane is at $x/R = 0$ and the flow moves from left, $x < 0$, to right, $x > 0$.

The momentum theory assumes that the flow axial velocity decreases smoothly along the rotor axis and the axial velocity at the rotor plane is the arithmetic mean of the axial velocities in the ultimate upstream and downstream. By observing the azimuthally averaged 3D flow over the baseline wind turbine, this description is only valid for the outboard flow (Fig. 4.1 a). In the inboard region, a flow acceleration, which is unexpected by the momentum theory, occurs at the rotor plane and yields a velocity peak. The velocity peak is more significant near the rotor axis. This velocity peak is supposed to be the consequence of the flow acceleration induced by the 2D effect due to the blade cascade.

Figure 4.1 (a) also shows an unusual flow feature that the axial velocity distribution at the innermost radius fluctuates behind the rotor plane. This fluctuated velocity distribution implies complex inboard flow structures and high gradient velocity fields. These complex inboard flows are presented in the following section (Sec. 4.1.2).

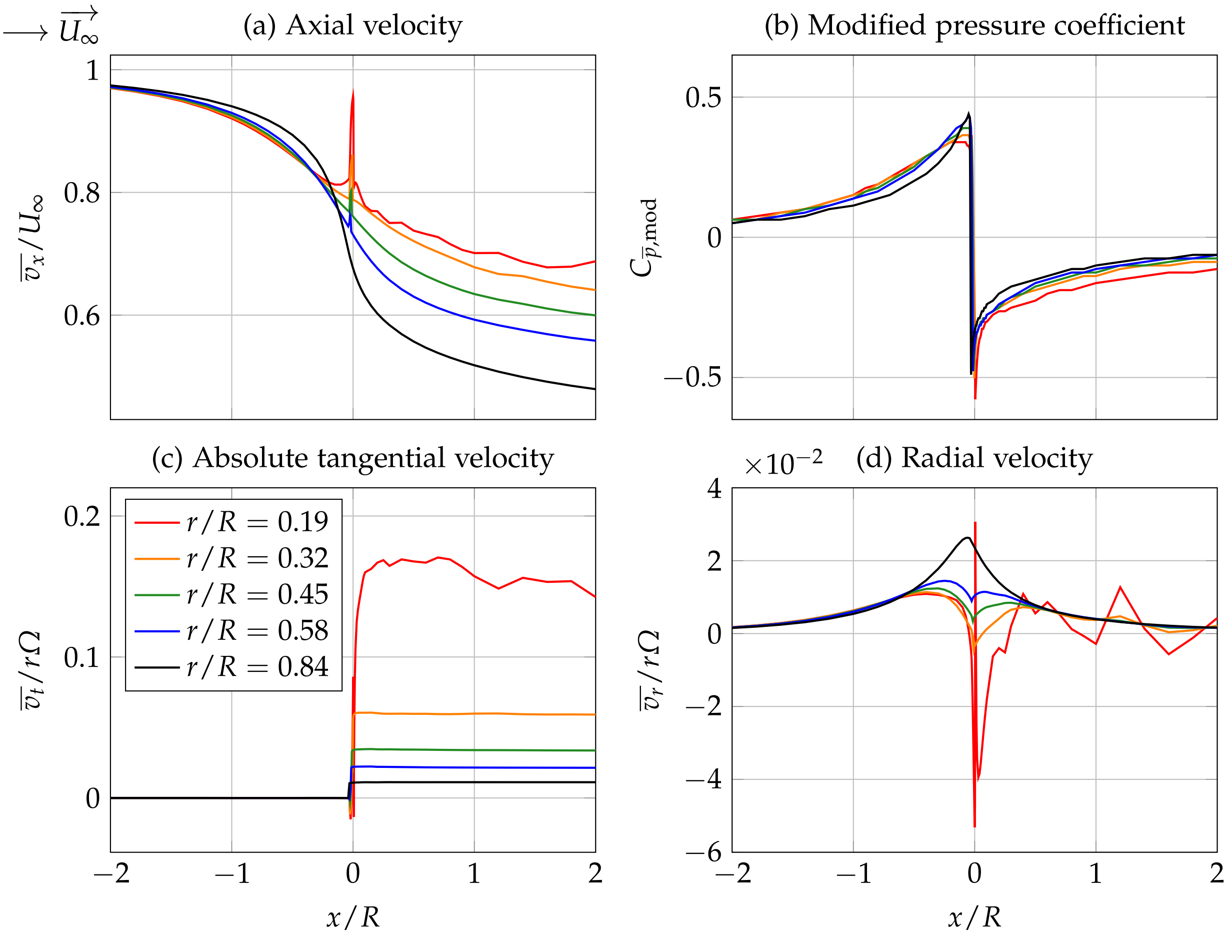

Figure 4.1: Azimuthally averaged velocity components and pressure over the effective annular area as a function of axial position (rotor plane at $x/R = 0$)

As described in the momentum theory (Sec. 2.1), accompanying with the smooth decrease in the axial velocity, the pressure increases smoothly when the flow approaches the rotor plane and drops abruptly at the rotor plane causing the rotor thrust. The flow pressure then regains its initial value in the ultimate downstream. These descriptions regarding the variation of the pressure along the rotor axis agree well with the computational results (Fig. 4.1 b), where the pressure is expressed by the modified pressure coefficient

$$C_{\overline{p},\mathrm{mod}} = \frac{\overline{p} - p_{\mathrm{ref}}}{\frac{1}{2}\rho U_\infty^2}, \tag{4.1}$$

and the pressure of the undisturbed flow is chosen as the reference pressure, $p_{\mathrm{ref}} = p_\infty$.

In contrast to the axial velocity which has a continuous variation along the rotor axis, the tangential velocities are zero before the rotor plane and abruptly increases at the rotor plane (Fig. 4.1 c). The tangential velocity then remains approximately constant in the wake by the principle of the angular momentum conservation. The induced tangential velocity components are more significant near the blade roots, which agrees with the the general momentum theory (Fig. 2.2 left). Similar to the axial velocity, the tangential velocity in the inboard region fluctuates behind the rotor plane.

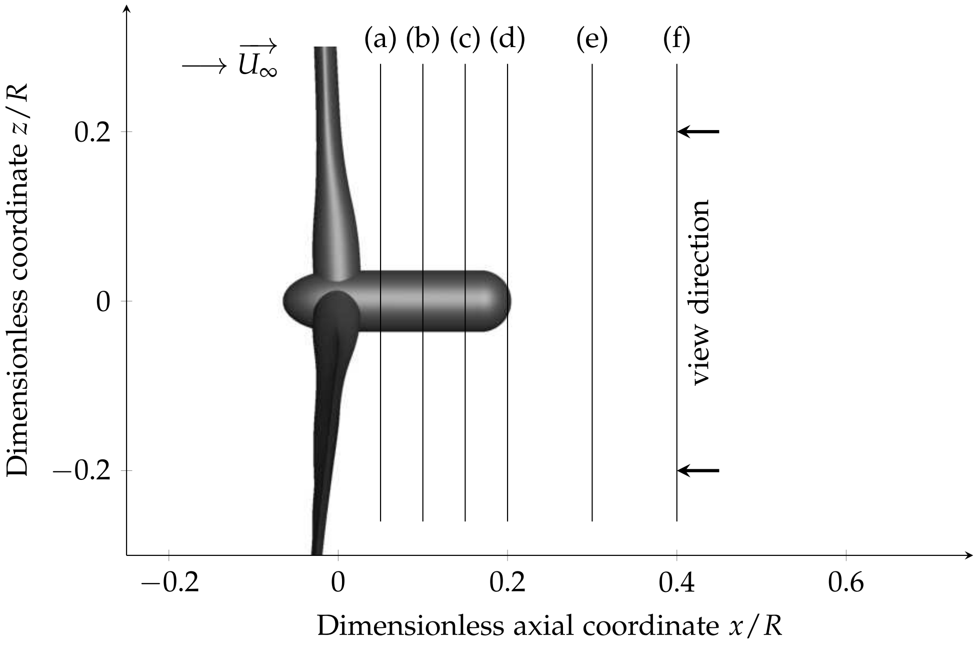
$\longrightarrow \overrightarrow{U_\infty}$
(a) (b) (c) (d)
(e)
(f)
view direction
Dimensionless coordinate z/R
0.2
0
−0.2
−0.2
0
0.2
0.4
0.6
Dimensionless axial coordinate x/R

Figure 4.2: Slice positions and the view direction for studying flow features near the blade roots

Because the lift augmentation caused by the 3D effect due to rotation is closely related to radial flows, the radial velocity components are specifically presented here. Figure 4.1 (d) depicts the azimuthally averaged radial velocity component over the effective annular area and normalized by the tangential velocity of the local blade sections. This figure shows that radial velocity components are induced near the rotor plane and there are no significant radial flow in the ultimate upstream and downstream. Except for the innermost blade section, the radially outwards velocity components increase approaching the blade tip. At the innermost blade section, the annually averaged radial velocity distribution is complex and even becomes negative. This study posits that these radially outwards velocity components are basically induced by the flow expansion due to flow deceleration. With the increasing complexity of the rotor geometry and the blade solidity near the rotor axis, the radial velocity distributions are more complex in the inboard region. Because of the limited quantity of the induced radial velocity components, specifically in the inboard region, this study suggests that these radial flows have no significant contribution to the lift augmentation.

4.1.2 *Flow near the blade roots*

The incoming flow near the rotor axis accelerates when it passes over the spinner and the inboard blade cascade. Since the blade solidity, which represents the blade cascade, is inversely proportional to the radius (Eq. 2.29), the flow acceleration due to the blade cascade is supposed to be more pronounced in the inboard region. In order to observe this flow acceleration, several planes perpendicular to the rotor axis are extracted (Fig. 4.2). The dimensionless velocity magnitude over these planes are depicted. Because the velocity distributions at different

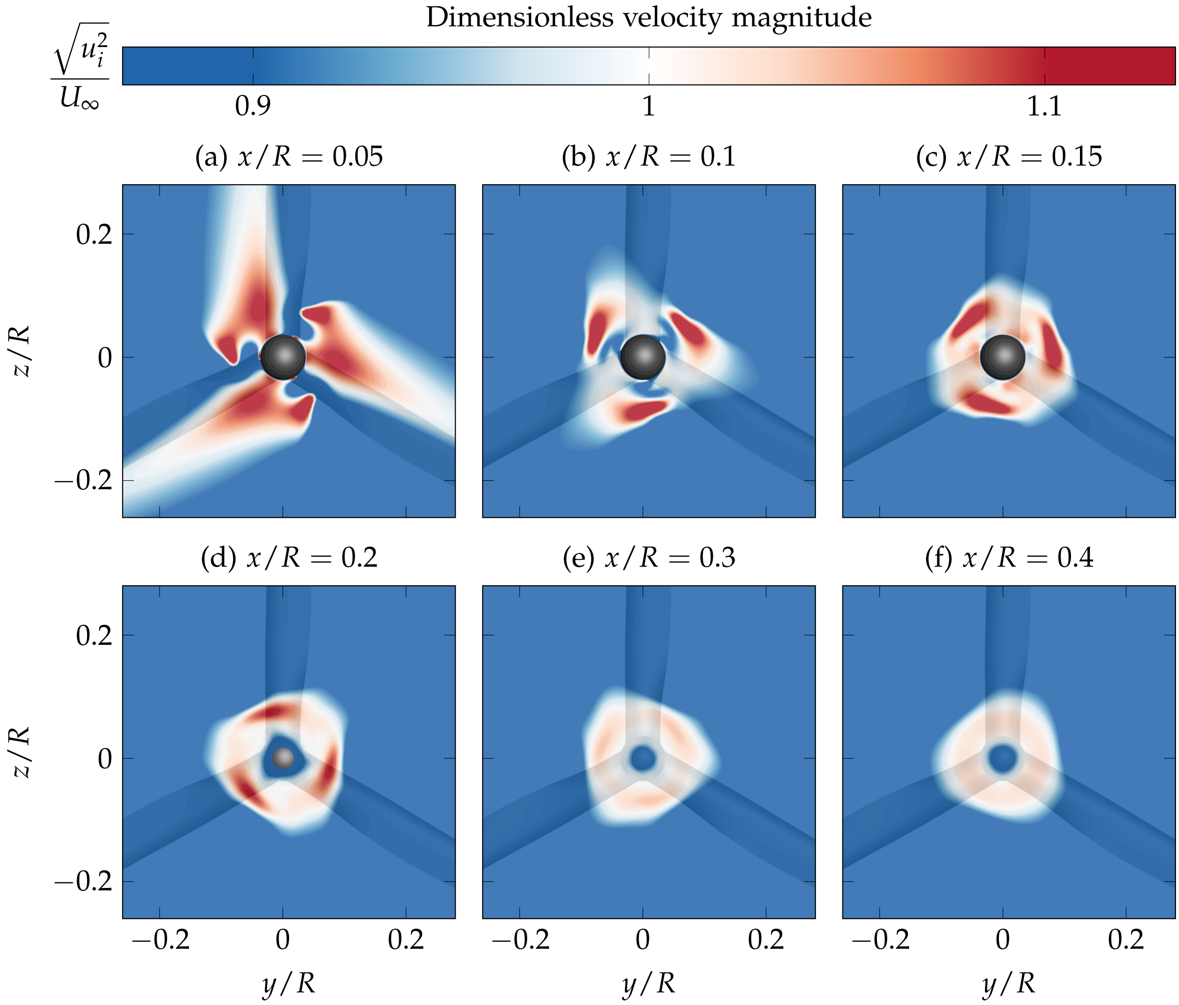

Figure 4.3: Time-averaged velocity distributions of the inboard flow over the baseline wind turbine at the rated wind speed of $U_\infty = 11.4$ m/s.

operating conditions are similar, only the time-averaged velocity fields at the rated wind speed $U_\infty = 11.4$ m/s are presented.

Figure 4.3 shows that a significant flow acceleration occurs in the near wake of the baseline wind turbine. This flow acceleration is more prominent near the rotor axis. In the vicinity of the nacelle surface, low speed shear flows occur due to surface friction (Fig. 4.3 a–d). Moreover, a low speed region forms behind the nacelle (Fig. 4.3 e–f). Because of the azimuthal periodicity, the three-bladed baseline wind turbine induces three azimuthally periodic flow regions.

The flow near the blade roots has high velocity gradients. These gradients decrease as the flow travels downstream and eventually become unnoticeable (Fig. 4.3). The flow at $x/R = 0.4$, whose velocity distribution is nearly azimuthally uniform, is divided into three regions (Fig. 4.3 f). First is the low speed region corresponding to the nacelle wake and aligned with the rotor axis. Second is also a low speed region corresponding to the flow passing through the airfoil-shaped blade sections with a significant loss of kinetic energy. Third is the region where the flow passes through the cylinder blade roots and the blade transition sections and has less kinetic energy loss.

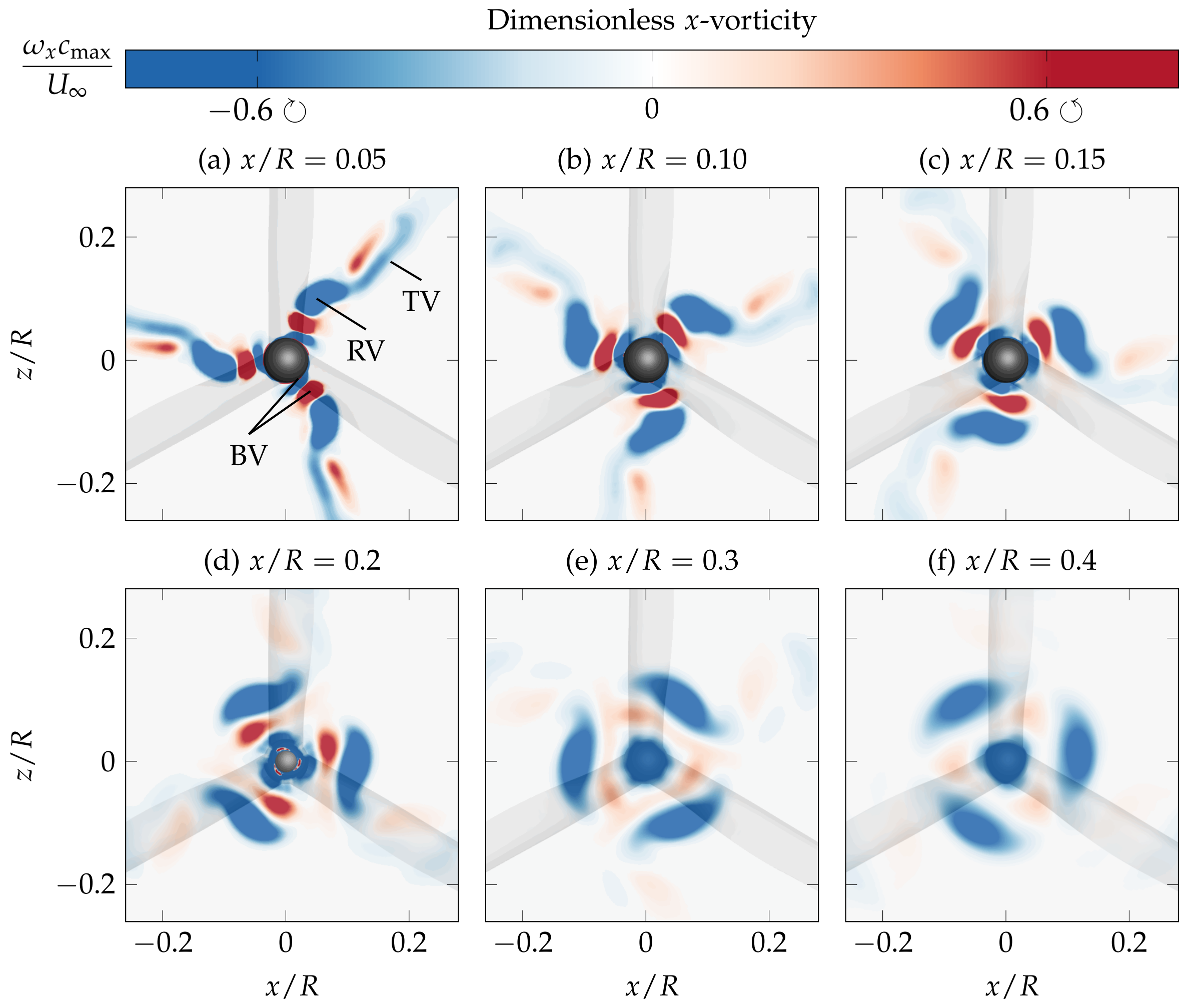

Figure 4.4: The out-of-plane vorticity distributions evaluated from the time-averaged velocity fields over the baseline wind turbine at the rated wind speed of $U_\infty = 11.4$ m/s (The root vortex, base vortices, and trailing vortex are denoted by RV, BV, and TV, respectively.)

In order to accurately characterize the inboard shear flows, the out-of-plane vorticity, namely the vorticity component in the rotor axis direction

$$\omega_x = \frac{\partial v}{\partial z} - \frac{\partial w}{\partial y} \tag{4.2}$$

is evaluated. The dimensionless out-of-plane vorticity based on time-averaged velocity fields is depicted in Fig. 4.4. Kutta-Joukowski theorem (Wislicenus 1947, p.170) and the vortex laws of Helmholtz (Wislicenus 1947, p.295) suggest that horseshoe vortices will shed at both ends of the wind turbine blades due to the abrupt drop of the blade-bound circulation. The vortex which sheds from the blade roots is called root vortex. The root vortex is identified and denoted by RV in Fig. 4.4 . The root vortex shedding from the blade root rotates around its vortex center against the rotor direction. When looking upstream as presented in Fig. 4.4, the baseline wind turbine rotates counter-clockwise, thus the root vortex rotates around its vortex center clockwise with $\omega_x < 0$.

Figure 4.4 also shows other small scale vortices in the near wake of the blade roots, such as the trailing vortices (TV) which shed from the trailing edges of the rotor blade. The formation of the trailing vortices is similar to that of the root vortex due to the change in the blade-bound circulation along the blade. Near the surface of the nacelle, a pair of counter rotating vortices shedding from each blade root are also observed (Fig. 4.4 a–d). This pair of counter rotating vortices are supposed to be similar to that observed by Zahle and Sørensen (2011). Since this pair of vortices are found near the base of the blade root, they are named base vortices and denoted by BV. As a consequence of the periodicity of three-bladed rotor, three root vortices and three pairs of base vortices are observed. As the base vortices move downstream, they merge together at the end of the nacelle and form a vortex along the rotor axis. By the principle of Newton's third law, this counter-rotating wind turbine rotor exerts an adverse angular momentum on the flow, i. e. the wake of the wind turbine rotates against the rotor direction. In consequence, the overall wake flow rotates clockwise around the rotor axis (Fig. 4.4).

4.1.3 *Coherent structures near the blades roots*

As the flow passes over the cylinder blade root and the blunt inboard section, massive flow separation occurs. Streamline topology is used in this study to identify flow separation and critical points (Fiedler 1987). The critical points in the streamline patterns help to efficiently characterize the flow features. Figure 4.5 presents the streamline patterns on the blade suction side at various wind speeds. The attached boundary layer, whose streamline patterns are approximately parallel to the external free stream can be easily identified. Similarly, the detached boundary layer with significant radial flows are also identified from the streamline patterns.

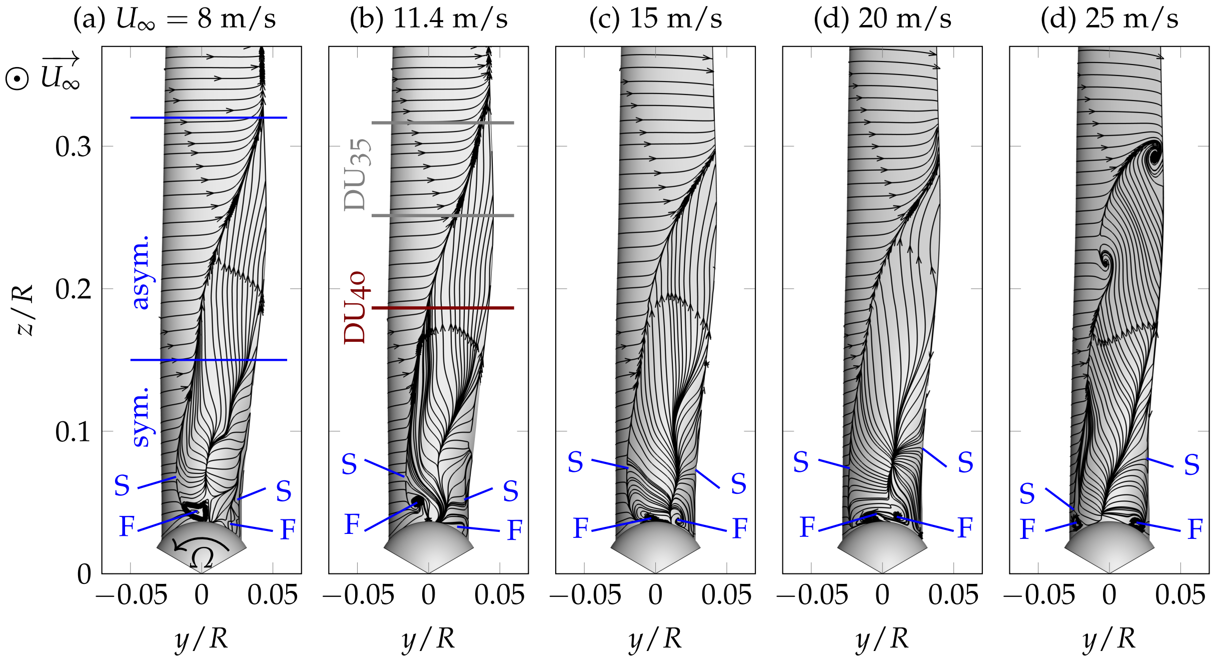

Figure 4.5: The streamline patterns on the blade suction side (The notations F and S imply foci and saddle, respectively.)

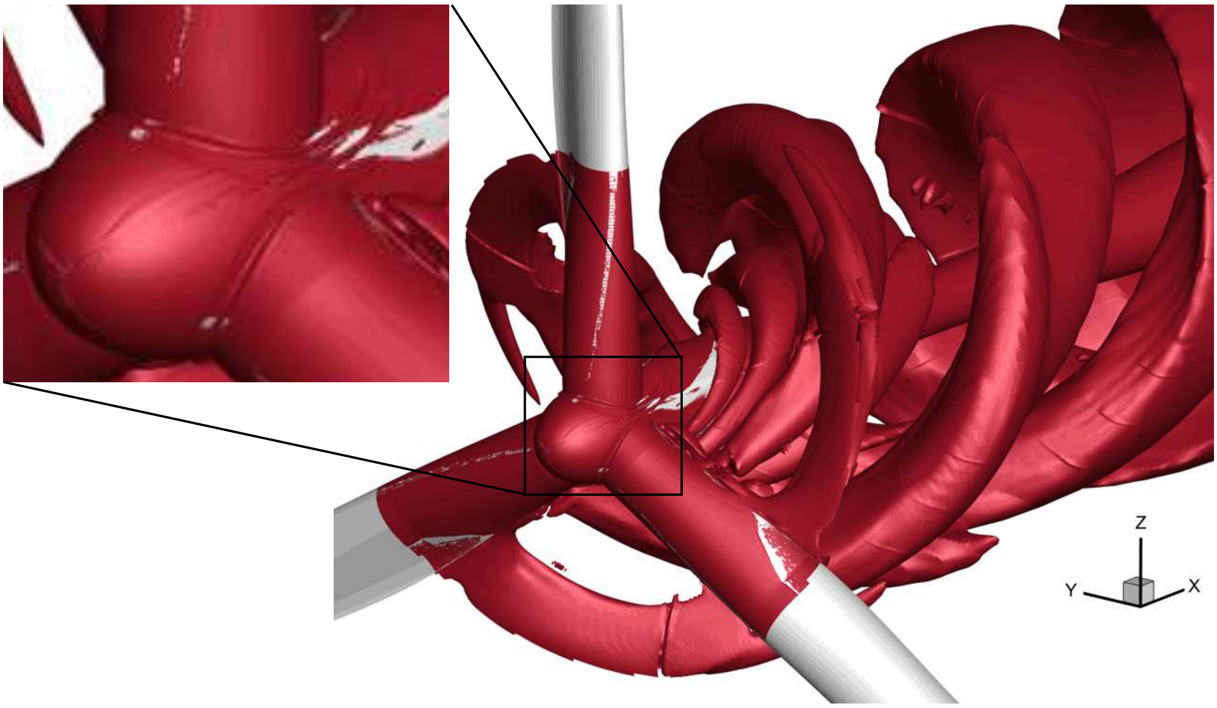

Figure 4.6: The vortex core structures near the blade roots of the baseline wind turbine at $U_\infty = 11.4$ m/s (isosurface of $Q = 0.05$)

The extent of the boundary layer separation is from the blade root up to $z/R = 0.32$. In order to accurately characterize the detached flow, this study further divides the separation region into symmetric and asymmetric parts.

The symmetric flow separation region starts from the base of the cylindrical blade root and ends approximately at $z/R = 0.15$, whereas the asymmetric separation region is from $z/R \approx 0.15$ up to the end of flow separation. The symmetric flow separation region indicates the existence of a von Kármán vortex street which is responsible for the unsteady flow behavior in the near wake. On the base of the symmetric flow separation region, a pair of counter-rotating vortices are received attention. This pair of counter-rotating vortices are supposed to be the origin of the counter-rotating base vortices observed in Fig. 4.4. The centers of the base vortices can be approximately determined by the foci of the streamline patterns, which is denoted by F in Fig. 4.5. The extent of the base vortex is determined by the saddle points which are denoted by S in Fig. 4.5. The occurrence of the base vortices are basically the consequence of the flow passing over the conjunction of the cylinder blade root and the spinner. Similar vortical structures were also observed by Sumner et al. (2004), Pattenden et al. (2005), Ozturk et al. (2009), Wang et al. (2009), Palau-Salvador et al. (2009) in experimental and numerical investigations where the base vortices were induced when flows passed over a cylinder mounted on a flat plate.

The flow behavior in the asymmetric flow separation region is monotonous and significant radial flows are involved. The streamline patterns in the flow separation region slightly vary with the operating conditions, specifically at $U_\infty = 25$ m/s. This change in the streamline patterns with the operating conditions implies the dependency of the detached flow on the operating conditions.

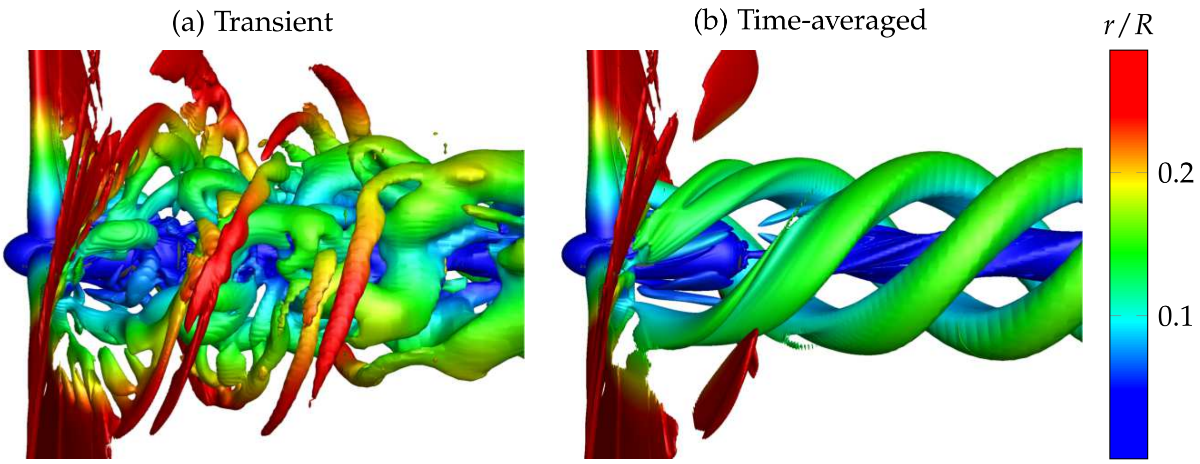

Figure 4.7: The vortex core structures based on (a) the transient and (b) the time-averaged velocity fields near the blade roots of the baseline wind turbine at $U_\infty = 11.4$ m/s (isosurface of $Q = 0.05$)

In order to efficiently identify the vortex cores near the blade roots, the Q-criterion proposed by Hunt (1987)

$$Q := \frac{1}{2}\left(\left|\Omega_{i,j}\right|^2 - \left|S_{i,j}\right|^2\right) > 0 \tag{4.3}$$

is used, where

$$\Omega_{i,j} = \frac{1}{2}\left(\frac{\partial u_i}{\partial x_j} - \frac{\partial u_j}{\partial x_i}\right) \tag{4.4}$$

is vorticity tensor and

$$S_{i,j} = \frac{1}{2}\left(\frac{\partial u_i}{\partial x_j} + \frac{\partial u_j}{\partial x_i}\right) \tag{4.5}$$

is strain-rate tensor. According to the definition of Q-criterion, the vortex core is the spatial volume where the vorticity is more dominant than the strain rate. Q-criterion has been widely used to detect the secondary flow structures in turbomachines, such as by Natkaniec (2012).

Figure 4.6 shows the vortex cores near the blade roots by means of the Q-criterion, where the iso-surface of $Q = 0.05$ is chosen. The prominent root vortex core and its helical structures are easily identified by this method. The pair of base vortices near the surface of the nacelle are also detected. A horseshoe vortex which wraps around the blade root on the surface of spinner is in advance identified (see the zoom-in picture in Fig. 4.6). The size of the horseshoe vortex is substantially dependent on the boundary layer thickness on the spinner. Thus, its influence is supposed to be negligible in comparison with the root vortex and another large scale vortical structures. Most of the small-scale vortical structures diminish at the end of the nacelle. Only the helical root vortex and the nacelle wake exist further downstream. Although Q-criterion provides an easy way to detect the complex vortical structures near the blades roots, the origin of the root vortex is however still difficult to locate.

The Q-criterion can not only be used to detect the vortical structures of the steady flow but also those of unsteady flows. Figure 4.7 (a) presents typical instantaneous vortical structures

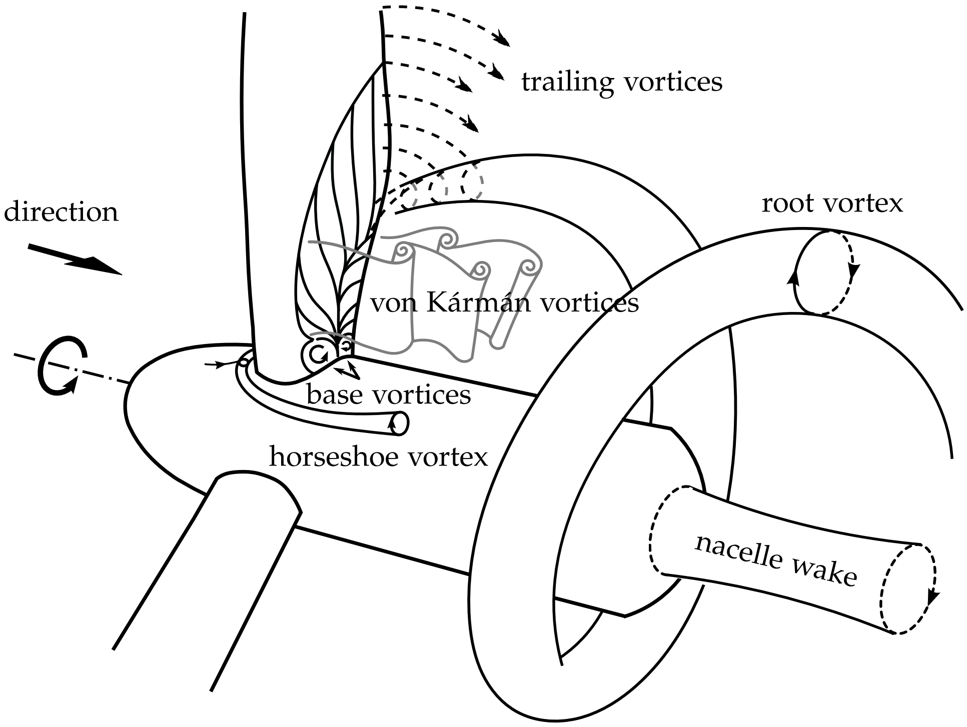

Figure 4.8: The sketch of the coherent structures near the blade roots of a modern wind turbine

near the blade roots of the baseline wind turbine based on the unsteady computational results of the wind speed of $U_\infty = 11.4$ m/s. The instantaneous flow consists of many small scale vortical structures. The helical root vortex structure, as observed in Fig. 4.6 based on the RANS computational results, cannot be easily identified from this instantaneous representation. In order to capture the coherent structures, the unsteady velocity fields are averaged over a period of time and the Q-criterion is applied on the time-averaged velocity fields. Figure 4.7 (b) shows that the helical root vortices based on the time-averaged velocity fields can be explicitly identified. The detected vortical structures are almost identical to those based on the steady simulations (Fig. 4.6). Therefore, the RANS computational results are supposed to be sufficient for the following investigation with respect to the root vortex origin and development.

According to the detected vortical structures, a sketch which summarizes the prominent coherent structures near the blade root of the horizontal axis wind turbine is depicted in Fig. 4.8. It includes the helical root vortex, the trailing vortices which shed from the trailing edges of the rotor blade, the flow separation with significant radial velocity components, the unsteady von Kármán vortex street shedding from the symmetric separation region, the pair of counter-rotating base vortices, the horseshoe vortex, and the low speed nacelle wake.

4.1.4 *Root vortex origin and development*

The root vortex which sheds from the blade root form a helical structure. This helical structure is basically caused by the relative motion between the fluid and the rotor blades. By neglecting the induced axial and tangential velocities which are limited near the blade roots, the spatial distribution of the helical root vortex can be approximately estimated by the wind speed and

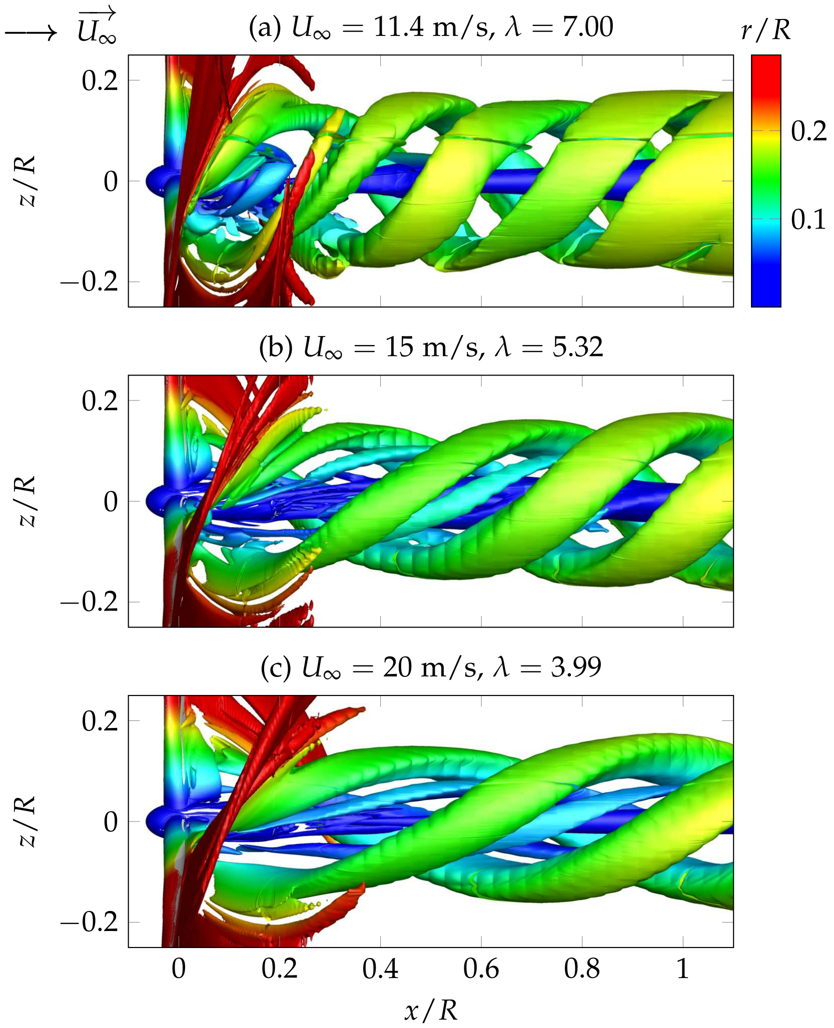
$\longrightarrow \overrightarrow{U_\infty}$
(a) $U_\infty = 11.4$ m/s, $\lambda = 7.00$
r/R
0.2
0.1
z/R
0.2
0
−0.2
(b) $U_\infty = 15$ m/s, $\lambda = 5.32$
z/R
0.2
0
−0.2
(c) $U_\infty = 20$ m/s, $\lambda = 3.99$
z/R
0.2
0
−0.2
0
0.2
0.4
0.6
0.8
1
x/R

Figure 4.9: The dependence of the helical pitch on the wind speeds (isosurface of $Q = 0.05$ based on RANS computational results)

the rotor speed, namely the tip speed ratio. This implies that the helical root vortex structure is simply dependent on the operating conditions. In order to describe the dependence of the helical structures on the operating conditions more efficiently, the pitch of the helix which is defined as the the axial distance for the helix to complete one revolution is considered. Since the pitch of the helical root vortex is inversely proportional to the tip speed ratio, the pitch of the root vortex increases with the wind speeds (Fig. 4.9).

In order to accurately describe the helical root vortex structure in space, vortex lines which represent the center of the vortex core along the vortex filament are considered. This study uses the vortex line detection method proposed by Sahner (2009) who defined the vortex line is the ridge line of the Q-invariant, i. e. the maximum value of Q along the vortex tube. The ridge line of the Q-invariant is determined in this study by detecting the maximal Q-invariant on various planes perpendicular to the rotor axis (Fig. 4.10 a). Since the inboard flow also involves other vortical structures such as the based vortices, only the velocity fields within $0.08 \leq r/R \leq 0.2$ are taken into account.

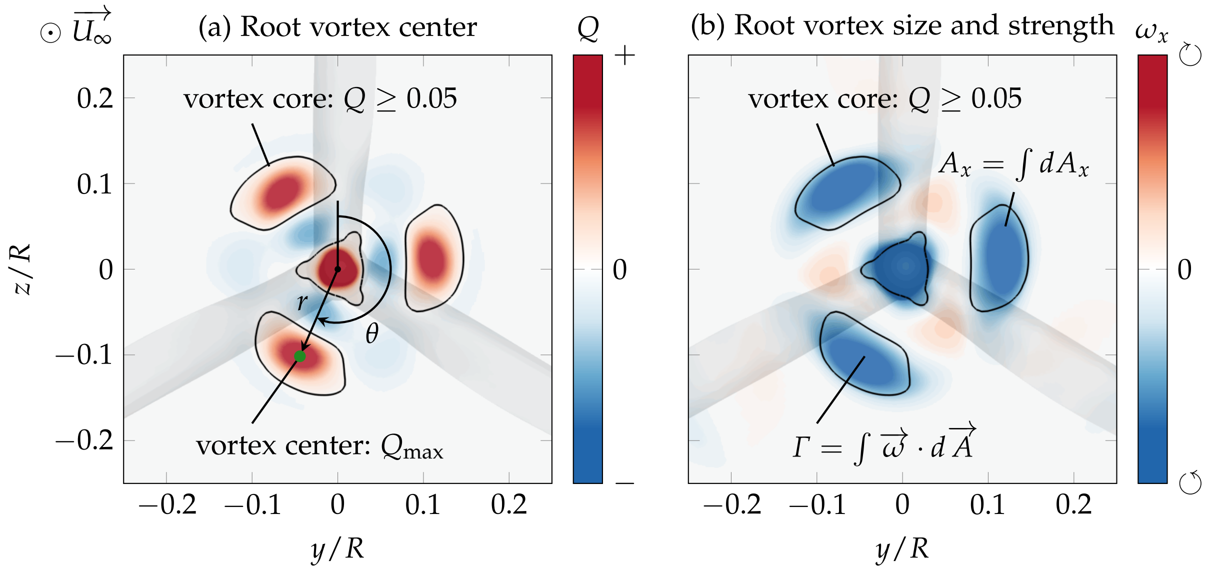
$\odot \overrightarrow{U_\infty}$
(a) Root vortex center
Q
+
0
−
vortex core: $Q \geq 0.05$
vortex center: Q_{max}
r
θ
z/R
0.2
0.1
0
−0.1
−0.2
y/R
(b) Root vortex size and strength
ω_x
vortex core: $Q \geq 0.05$
$A_x = \int dA_x$
$\Gamma = \int \vec{\omega} \cdot d\vec{A}$

Figure 4.10: Determination of (a) the spatial position of the root vortex center and (b) the root vortex size and strength

The spatial distributions of the root vortex line are depicted in Fig. 4.11. Figure 4.11 (a) presents the radial position of the root vortex line along the rotor axis. By extrapolating the data at the rotor plane of $x/R = 0$, it suggests that the root vortex origin of the baseline wind turbine is at the blade transition section of $0.1 < r/R < 0.15$. This estimate of the root vortex origin agrees with the argument of Lindenburg (2003) that the root vortex does not shed from the hub nor the radius of the innermost profile. The estimation of the radial position of the root vortex is relevant because it influences the accuracy of applying the root loss correction factor and consequently the accuracy of the BEM method.

Figure 4.11 (a) also shows a dependence that the radial position of the root vortex core decreases slightly with increasing wind speeds. Furthermore, the root vortex at all the operating conditions moves radially outwards at the end of the nacelle and then slightly contracts at $x/R = 0.4$. For $x/R > 0.4$, the distance of the vortex center from the rotor axis increases again.

The variation of the azimuthal angle of the root vortex line along the rotor axis is also presented in Fig. 4.11 (b), where the azimuthal angle is defined as the angle between the root vortex center and the reference blade (Fig. 4.10 a). By neglecting the induced velocities, the azimuthal position of the helical root vortex along the rotor axis is only dependent on the tip speed ratio

$$\theta = \left(\frac{x}{R}\right) \lambda. \tag{4.6}$$

Figure 4.11 (b) depicts not only the azimuthal angle of the root vortex lines determined from the computational results but also this theoretical relationship (Eq. 4.6). The considerable deviation between the computational results and the theoretical relationship suggests that the root vortex is influenced by the induced velocities.

Because the life span of the root vortex is one of the decisive parameters for the wind park design, the development of the root vortex, specifically its size and strength, is further

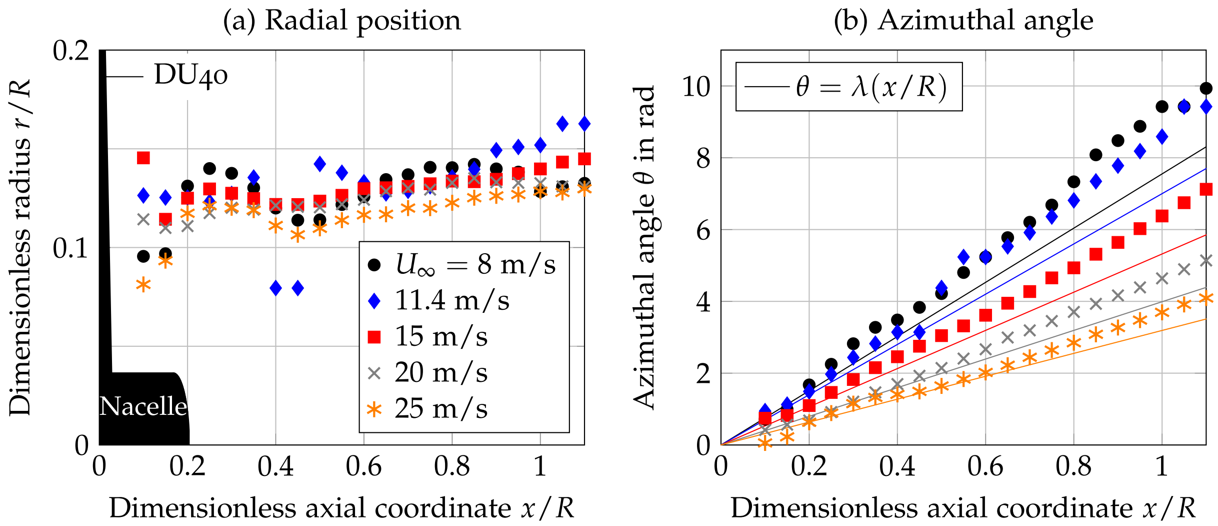

Figure 4.11: The variation of (a) the radial position and (b) the azimuthal angle of the root vortex line as a function of dimensionless axial position

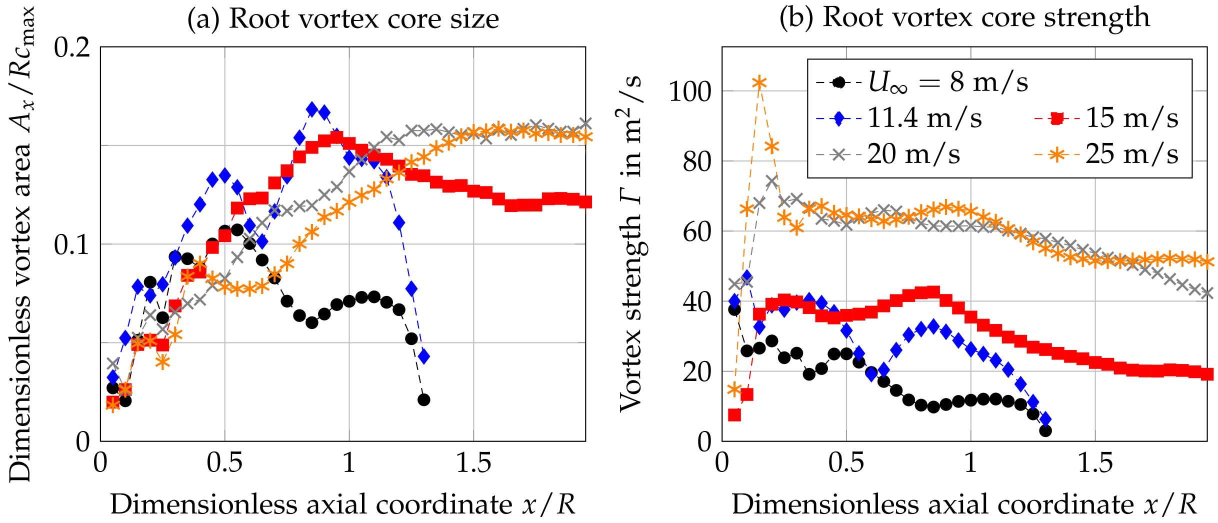

Figure 4.12: The development of the root vortex core in (a) size and (b) strength at various wind speeds

investigated. The size of the root vortex core is determined in this study by evaluating the cross-sectional area enclosed by the Q-criterion at various x-planes (Fig. 4.10 b). The strength of the root vortex core is then determined by integrating the out-of-plane vorticity over this area (Fig. 4.10 b).

Figure 4.12 shows that the development of the root vortex is considerably dependent on the operating conditions. The size of the root vortex core increases gradually when it sheds from the rotor blade, and then decreases gradually in the downstream (Fig. 4.12 a). The strength of the root vortex at various operating conditions shows a similar tendency that the root vortex strength is maximal near the rotor plane and then decreases gradually in the flow direction (Fig. 4.12 b). The development of the root vortex size and strength illustrates the same story that the root vortex dissipates at approximately of $x/R = 1.4$ at the wind speeds of $U_\infty = 8$

m/s and 11.4 m/s. Furthermore, the root vortex at high wind speeds has higher strength and greater size. As a result of that, the influence of root vortices on downstream wind turbines in a wind farm should be taken into account when the wind turbines operate at high wind speeds.

So far, this study gives an insight into the root vortex origin and its development along the rotor axis by analyzing the wake flow directly. However, the information of the wind turbine wake flow is usually unavailable in the design process. As an alternative way, the root vortex origin and its strength is estimated in the design process from the blade-bound circulation, since it is responsible for the vortex shedding. The blade-bound circulation, Γ, along the wind turbine blade is determined in this study according to Kutta-Joukowski theorem (Wislicenus 1947, p.170),

$$\Gamma = \frac{|L|}{\rho U_{\text{ref}}}, \tag{4.7}$$

where L implies lift per unit blade length. The reference wind speed of the 2D stationary profile is the undisturbed wind speed, $U_{\text{ref}} = U_\infty$. The reference wind speed of the 3D rotating wind turbine blade section is the effective wind speed, $U_{\text{ref}} = U_{\text{eff}}$. Figure 4.13 (a) shows that the blade-bound circulation evaluated from the BEM predictions agrees well with that from the CFD results. This supports the basic concept of predicting the root vortex origin and strength from the blade-bound circulation and the following analysis to identify them.

At the wind speeds lower and equal to the rated condition of $U_\infty = 11.4$ m/s, significant drops in the blade-bound circulation at the blade root and the blade tip indicate significant vortex shedding from there (Fig. 4.13 a). Furthermore, a slight increase in the blade-bound circulation in the midspan region indicates slight vortex sheet shedding from the trailing edge.

As the baseline wind turbine operates at the wind speeds higher than $U_\infty = 11.4$ m/s, the blade-bound circulation distributions are significantly different from those at the wind speeds lower and equal to the rated conditions (Fig. 4.13 a). As usual, a significant drop in the blade-bound circulation at the blade root indicates a significant vortex shedding from the blade root. With increasing wind speeds, the blade-bound circulation at the blade tip considerably decreases. Furthermore, the blade-bound circulation decreases gradually from the blade root towards the blade tip. As a result of these blade-bound circulation distributions, the tip vortex weakens and the trailing vortices strengthen at high wind speeds.

In order to explicitly identify the origin and the strength of the vortices, the spanwise gradient of the blade-bound circulation is in advance investigated. Figure 4.13 (b) shows significant peaks at the blade root and blade tip which indicate the root vortex and the tip vortex, respectively. The blade-bound circulation gradient in the blade midspan corresponding the trailing vortices are also observed. This study suggests that the origin of the root vortex is in the inboard region of the maximal blade-bound circulation gradient. Thus, the root vortex origin of the baseline wind turbine determined from the CFD results in Fig. 4.13 (b) is at $0.1 < r/R < 0.15$, agreeing with the vortex line analysis (Fig. 4.11 a). The root vortex origin determined from the BEM predictions is slightly higher at $0.15 < r/R < 0.2$. The discrepancy of the root vortex origins determined from the BEM predictions arises from the inaccurate airfoil data for the blade transition sections (Sec. 3.1). This study further suggests that the

(a) Blade-bound circulation

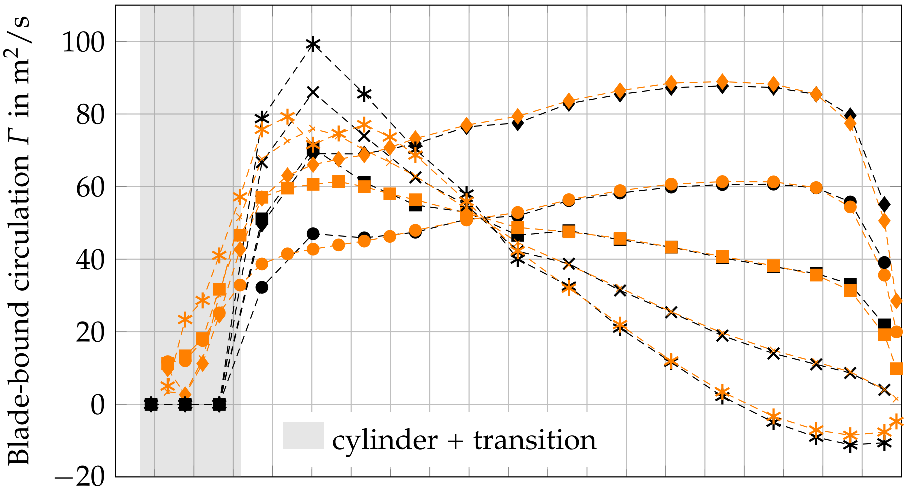

(b) Spanwise gradient of the blade-bound circulation

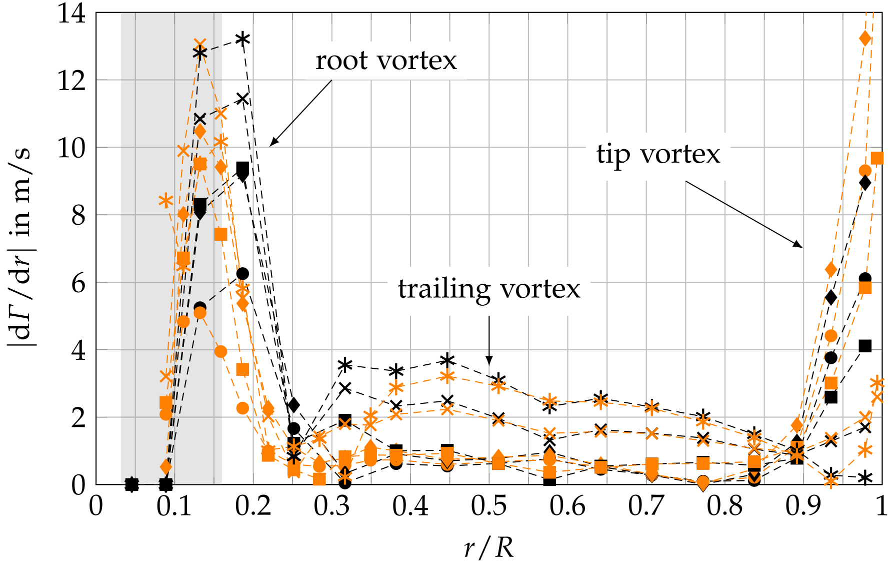

Figure 4.13: Blade-bound circulation and its spanwise gradient evaluated from the BEM predictions in black and CFD results in orange (symbol legend see Fig. 4.12)

strength of the root vortex is proportional to the maximal blade-bound circulation gradient in the inboard region, which derives that the root vortex strength increases with the wind speed, agreeing with the wake flow analysis (Fig. 4.12 b). Figure 4.13 (b) also demonstrates the increase in the strength of the midspan trailing votices and the decline of the tip vortex with the wind speeds.

4.2 EFFECTS OF SPINNER GEOMETRIES

This section presents the sensitivity study of the inboard coherent structures and the aerodynamic performance of the baseline wind turbine to the spinner geometry.

4.2.1 *Coherent structures*

The effect of the spinner geometry on the inboard predominant vortical structures, specifically the root vortices and the nacelle wake, is identified in this study by comparing the vortex core structures by means of Q-criterion based on the time-averaged velocity fields. Figure 4.14 shows that the vortex core structures over different spinners are similar, including the helical root vortices, nacelle wake, and small vortical structures near the surface of the nacelle. One noticeable difference is the size of the nacelle wake (Fig. 4.14 c). Since the nacelle diameter of the blunt conical spinner is greater than the other spinners, the increase in the diameter of the nacelle wake is supposed to closely correlated to the nacelle diameter. With the increase in the nacelle wake diameter, the interference between the root vortices and nacelle wake may occur.

4.2.2 *Aerodynamic performance*

The effect of the spinner geometries on the wind turbine performance is discussed in this section from two aspects, regarding the overall and local aerodynamic performance.

Figure 4.15 shows the relative improvement in the overall power output of the baseline wind turbine with different spinner designs, where the overall performance is evaluated by integrating the loads from the rotor center up to $r/R = 45$ m and the elliptical spinner is chosen as the reference spinner. Figure 4.15 (a) shows no significant improvement or deterioration in the mechanical power output among these different spinner designs. A limited improvement in the power output up to 0.25% is obtained for the wind turbine with the blunt conical spinner. Similarly, the relative increment in the overall rotor thrust is depicted in Fig. 4.15 (b), which shows that using the blunt elliptical spinner and the blunt conical spinner yields an increase in the overall rotor thrust up to 0.7%. This increase in the rotor thrust is supposed to be caused by the increase in the drag due to the blunt nose and the increased nacelle diameter.

Although the effect of the spinner geometry on the overall wind turbine aerodynamic performance is limited, the extent of its influence on the local aerodynamic performance is of importance further investigated. Because of the von Kármán vortex shedding from the thick blade roots, the local power coefficient in the inboard region fluctuates with time. Figure 4.16

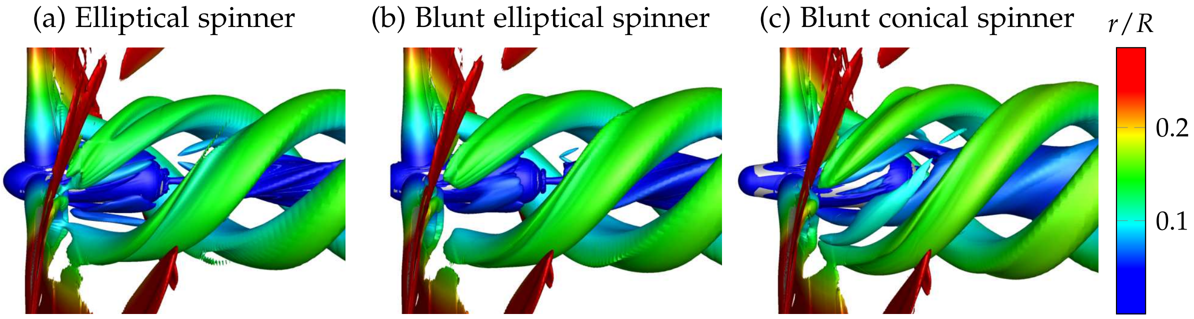

Figure 4.14: The vortex core structures based on the time-averaged velocity fields near the blade roots over various spinner geometries at $U_\infty = 11.4$ m/s (iso-surface of $Q = 0.05$)

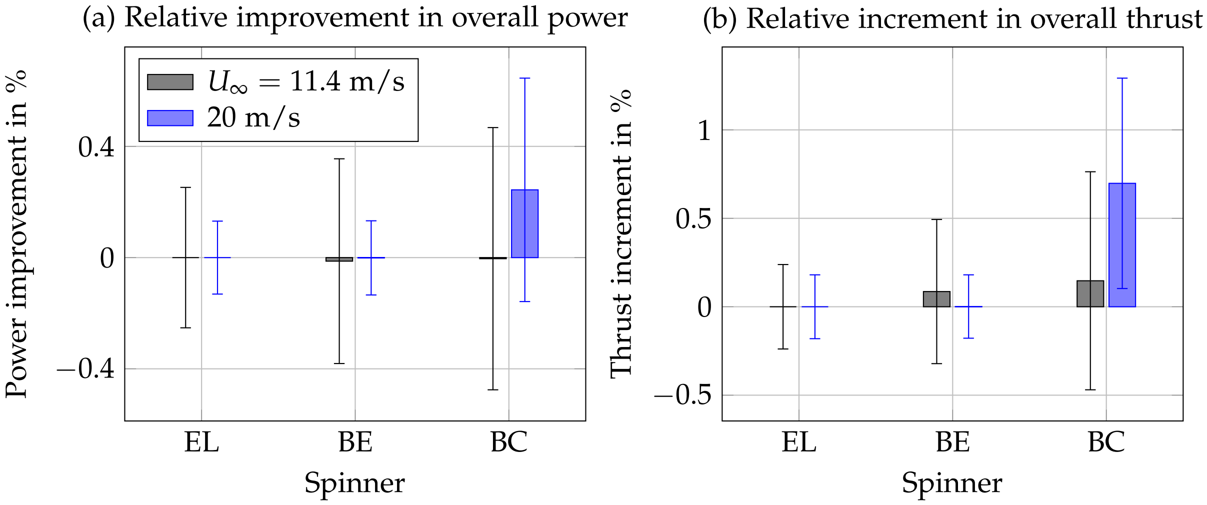

Figure 4.15: The influence of the spinner geometry on (a) the overall power output and (b) the overall rotor thrust

depicts the time-averaged local power coefficients and its standard deviation along the rotor blade at various wind speeds, which shows that the local power coefficients of the baseline wind turbine with different spinners except for the inboard region are identical. In the inboard region, the local power coefficients of the baseline wind turbine with the elliptical spinner and the blunt elliptical spinner are even almost identical. A considerable difference in the local power coefficient occurs in the inboard region of the wind turbine with the blunt conical spinner. Similarly, the effect of the spinner on the local thrust coefficient is also investigated. Figure 4.17 shows that the spinner geometry has only limited effect on the local thrust coefficient in the inboard region. Because the aerodynamic contribution of the local blade section is basically proportional to the radius, this change in the inboard local performance due to the spinner geometries has no significant effect on the overall performance, agreeing with Fig. 4.15. Moreover, since the flow acceleration and the radial velocity components induced by the spinner is limited for $r/R \geq 0.187$ (Fig. 4.16 and Fig. 4.17), the spinner effect on the inboard profile aerodynamics is supposed to be negligible.

4.3 3D EFFECT DUE TO ROTATION

This section, comprehensively and thoroughly investigating the 3D effect due to rotation, is divided into two subsections. In Sec. 4.3.1, the 3D rotational effects on the wind turbine aerodynamic performance, namely power overshoot and lift augmentation, are identified. Section 4.3.2 gives an insight into the 3D rotational effect on the circumferential flow behavior, the profile aerodynamic characteristics, and in particular the boundary layer properties. Based on the computational results presented in this section and the order of magnitude analysis in Sec. 2.2, mechanisms responsible for the 3D rotational effects on the attached and detached boundary layers are subsequently identified. The analytical expression (Eq. 2.84) derived in this study for the prediction of pressure distributions in the flow separation region of rotating blades is validated in the end of Sec. 4.3.2.

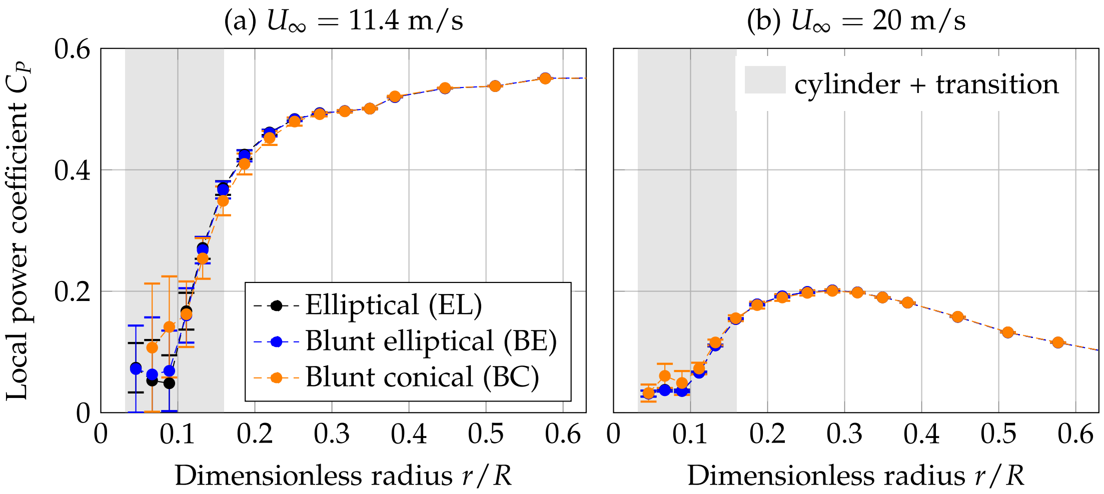

Figure 4.16: Local power coefficients of the baseline wind turbine with various spinner designs

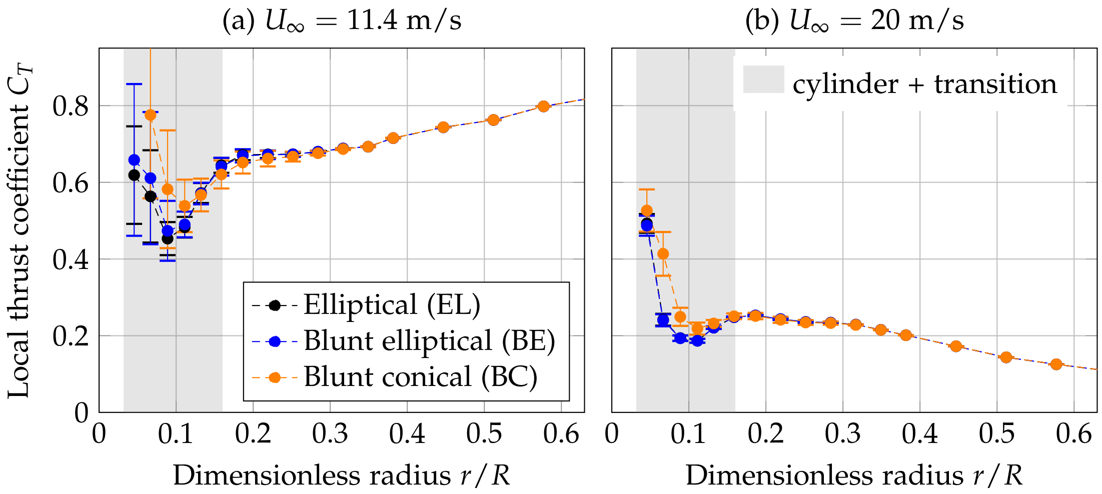

Figure 4.17: Local thrust coefficients of the baseline wind turbine with various spinner designs

4.3.1 *Aerodynamic performance*

The power overshoot due to the 3D rotational effects is identified in this study by comparing the mechanical power evaluated from the 3D CFD results and the BEM predictions. The aerodynamic performance of the 3D CFD results and the BEM predictions corresponds to the aerodynamic performance with and without the 3D rotational effect, since all the other 2D and 3D effects except that due to rotation are considered in the BEM iterations.

The left column of Fig. 4.18 depicts the overall power output and rotor thrust of the baseline wind turbine. The power and thrust evaluated from the CFD results are the mean values over the least one thousand iterations. The CFD results include loads on the spinner and nacelle, whereas the BEM predictions only consider the loads on the rotor blades.

For the wind speed lower than the rated condition of $U_\infty = 11.4$ m/s, the overall power and thrust exerted on the rotor of the baseline wind turbine increase gradually against the wind speed, and reach maximum values at the rated wind speed. For the wind speed higher than the rated condition, the overall power decreases slightly, whereas the overall thrust decreases significantly. At the cut-off wind speed, the overall power decreases by 22% relative to that at the rated condition, while the overall thrust is approximately one-third of that at the rated condition. The overall good agreement between the 3D CFD results and BEM predictions (Fig. 4.18 left column) implies that only limited 3D effects due to rotation on the pitch-controlled wind turbine.

The efficiency of the wind turbine converting the kinetic energy of wind into mechanical power is illustrated by the overall power coefficient and the overall thrust coefficient (Fig. 4.18 right column). It shows that at the wind speed less and equal to the rated condition, the wind turbine performs very well, approaching Betz's limit. The 3D effect due to rotation only results in a slight increase in the overall power coefficient at the wind speed less and equal to the rated condition, while no apparent change in the overall thrust coefficient occurs.

The power deviation factor

$$\zeta_P = \frac{P_{\mathrm{CFD}} - P_{\mathrm{BEM}}}{P_{\mathrm{BEM}}} \times 100\% \tag{4.8}$$

and the thrust deviation factor

$$\zeta_T = \frac{T_{\mathrm{CFD}} - T_{\mathrm{BEM}}}{T_{\mathrm{CFD}}} \times 100\% \tag{4.9}$$

are introduced in this study, in order to quantify the 3D effect due to rotation on the overall aerodynamic performance of the baseline wind turbine (Fig. 4.18 left column). It shows that the 3D effect due to rotation leads to a power overshoot up to 3.8% at the wind speed less and equal to the rated condition and a limited change up to 0.96% in the overall rotor thrust.

The local power, thrust, and torque coefficients as a function of radius, which make it possible to locate the extent of the 3D effect due to rotation, are depicted in Fig. 4.19. It shows that the baseline wind turbine performs very well at the wind speed less and equal to the rated condition, in agreement with Fig. 4.18. The local power coefficient even reaches a maximum value of $0.93\,C_{P,\mathrm{Betz}}$. Abrupt drops in the local coefficients at the blade tip and blade root imply the tip and root losses due to the 3D end effect. At the blade tip, the good agreement of the local performance coefficients with and without the 3D rotational effect indicates that Prandtl's approximation formula (Eq. 2.32) is accurate for the correction of the tip loss.

In the blade root region, the local performance coefficients of the baseline wind turbine evaluated from the 3D CFD results deviate considerably from those of the BEM predictions, specifically at the cylinder blade root and the blade transition section. This study suggests that this considerable deviation in the inboard region is substantially caused by the inaccurate geometrical description and inaccurate profile aerodynamic data given in the BEM iterations rather than the 3D rotational effect. For the innermost airfoil sections at $r/R = 0.187$, the local performance coefficients of the baseline wind turbine with the 3D rotational effect, namely those evaluated from the CFD results, are higher than those without the 3D rotational effect (BEM predictions). This deviation of the local performance coefficient is supposed to be caused by the 3D rotational effect. However, the local performance coefficients without the 3D rotational effect at $r/R \sim 0.25$, near the end of flow separation on the blade suction side are higher than those with the 3D rotational effect (Fig. 4.5). This deviation contradicts the expectation of the 3D rotational effect, and might imply the presence of another 2D or 3D effect.

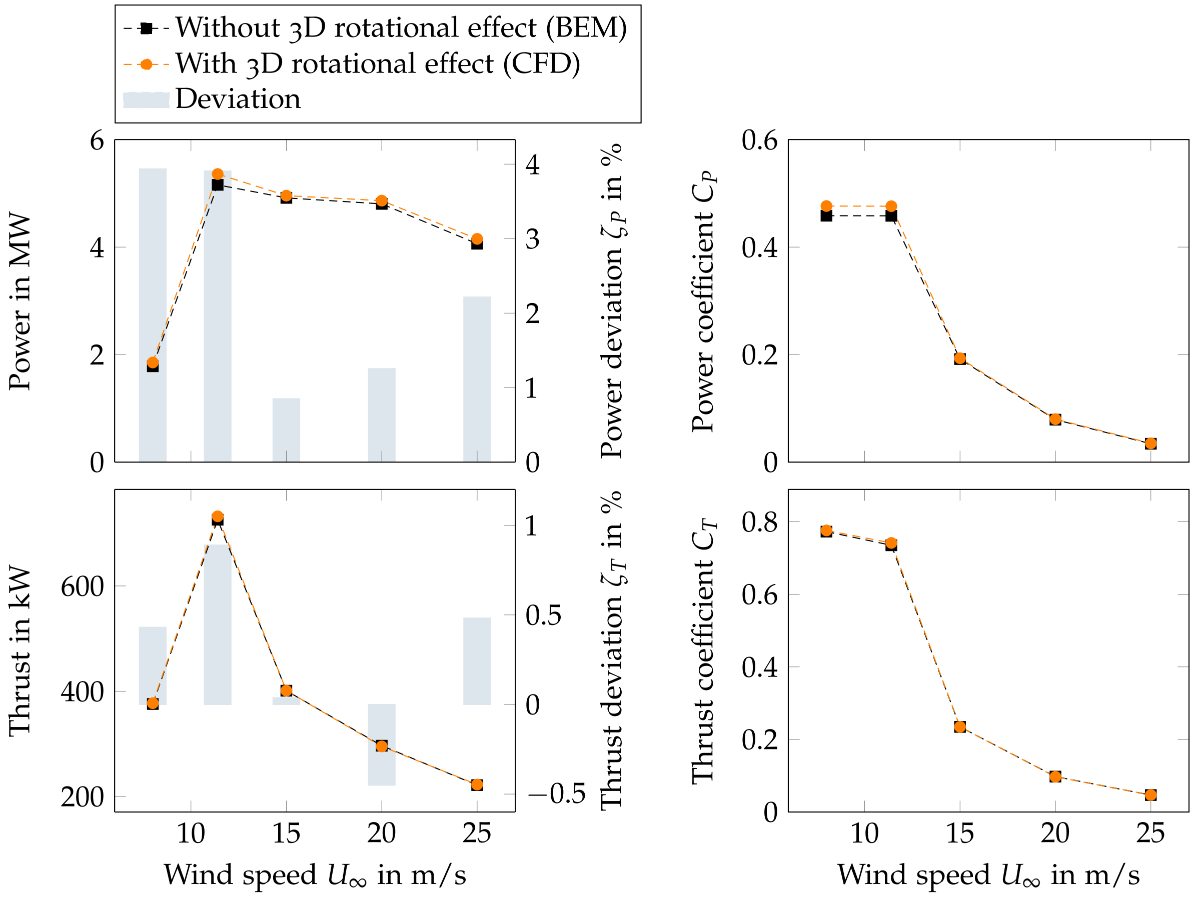

Figure 4.18: Comparison of the overall power and thrust on the baseline wind turbine at various wind speeds predicted by BEM and CFD computations

In order to identify the lift augmentation caused by the 3D effect due to rotation on the baseline wind turbine blades, the angle of attack should be first determined for evaluating the lift and drag coefficients. This study adopts the definition of the angle of attack for the rotating wind turbine blade from the BEM theory (Eq. 2.23 and Eq. 2.24). The axial and rotational induction factors are solved in this study iteratively by means of the inverse BEM method (Sec. 2.1.4).

Figure 4.20 depicts these coefficients evaluated from the CFD results by means of the inverse BEM method and those from the BEM predictions. It shows an overall good agreement between the conditions with and without the 3D rotational effect except the inboard region. Similar to Fig. 4.19, significant deviation is observed at the cylinder blade root and the transition section, which is supposed to be substantially caused by the inaccurate geometrical description and inaccurate aerodynamic data given in the BEM iterations. Furthermore, limited deviation occurs at the inboard profile sections.

The axial induction factor along the rotor blade decreases considerably with the wind speed, whereas the rotational induction factor shows a monotonic trend against the wind speed (Fig. 4.20). The rotational induction factor is approximately inversely proportional to the radius, in agreement with the assumption that the tangential velocity is induced by the trailing vortex

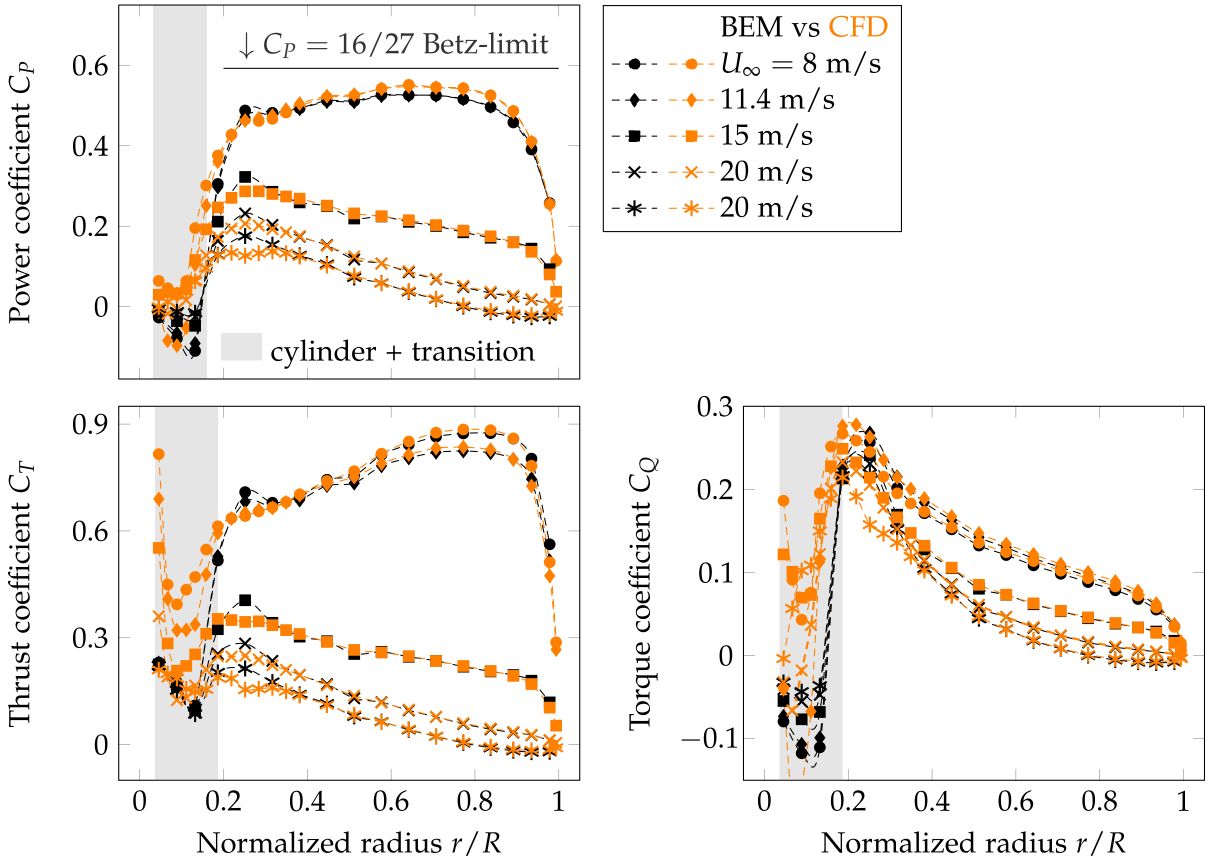

Figure 4.19: Local power, thrust, and torque coefficients as a function of radius at various wind speeds

system (Glauert 1935), or see Fig. 2.2. In addition, the rotational induction factor in the inboard region increase with the wind speed.

The distribution of the loss correction factors in Fig. 4.20 shows the interesting fact that the loss correction factor over the entire rotor blade is lower than one at the wind speeds higher than the rated condition. This implies that the entire rotor blade at high wind speeds undergoes losses due to trailing vortices, in agreement with the increase in the spanwise gradient of the blade-bound circulation against the wind speed (Fig. 4.13).

The good agreement of the angle of attack evaluated from the CFD results by means of the inverse BEM method with that from the BEM prediction in Fig. 4.20 suggests that the inverse BEM method is accurate for determining the angle of attack of the rotating blades. Basically, the angle of attack is higher in the inboard region and then decreases gradually with the radius. The angle of attack at the wind speeds higher than the rated condition even becomes negative in the outboard region. The angle of attack in the inboard region among different operating conditions shows no significant difference. The high values of the angle of attack in the inboard region suggests the occurrence of flow separation, which may be consequently responsible for the power overshoot caused by the 3D effect due to rotation on the baseline wind turbine.

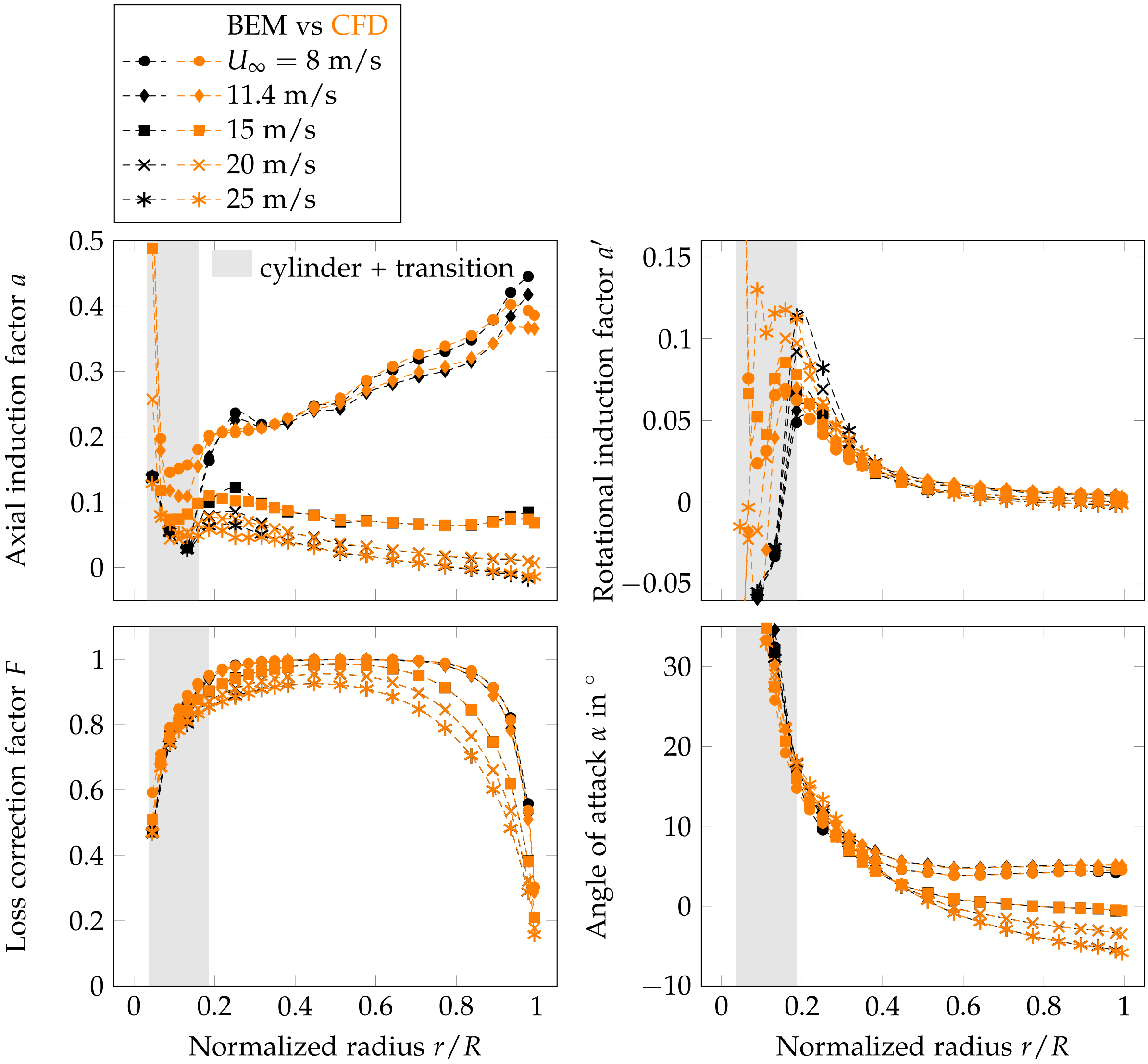

Figure 4.20: The axial, rotational induction factors and loss correction factors as a function of radius at various wind speeds

Because an additional post-processing is needed for the determination of the angle of attack, the geometrical angle of attack

$$\alpha_{\text{geo}} = \tan^{-1}(\lambda_r^{-1}) - \beta, \tag{4.10}$$

which disregards the induced velocities at the rotor plane is commonly used, such as by Eggers et al. (2003), Lindenburg (2003). Due to the regardless of the induced velocities, the geometrical angle of attack is higher than the effective angle of attack. Figure 4.21 shows the significant deviation of the geometrical angle of attack from the effective angle of attack, particularly when the wind turbine performs efficiently.

With the evaluated induction factors, the effective velocity at the rotor plane is then obtained (Eq. 2.22). Figure 4.22 compares the chord Reynolds number, Re $= \rho U_{\text{eff}} c/\mu$, along the wind turbine blade evaluated from the 3D CFD results and the BEM predictions. Because the induction factors evaluated from the CFD results are almost identical to those from the BEM predictions, the chord Reynolds number between them are almost identical. The Reynolds

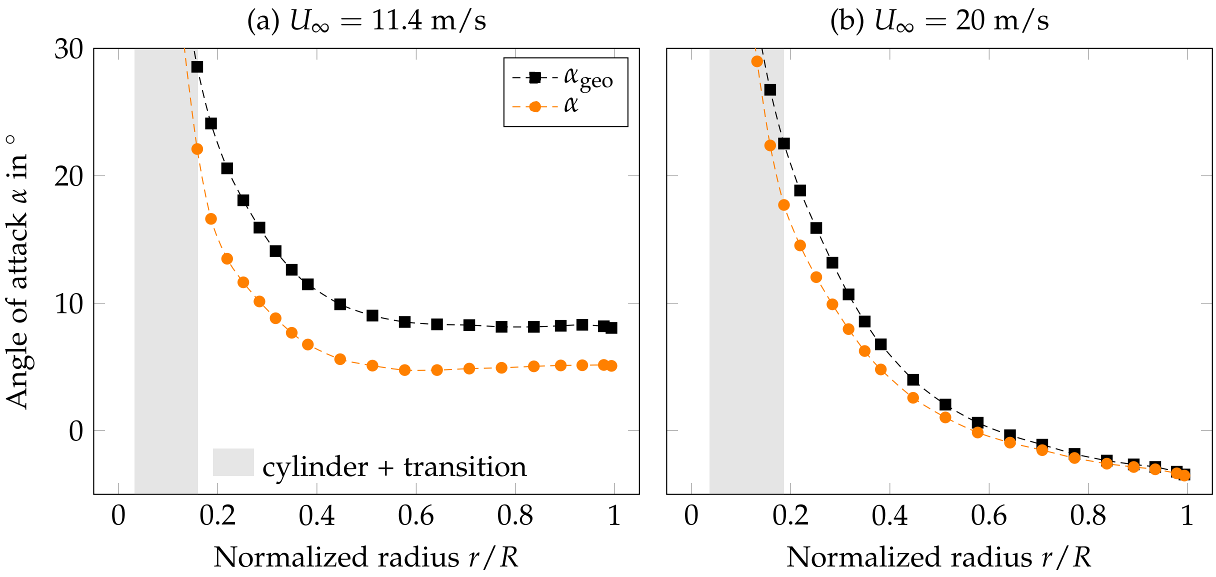

Figure 4.21: Comparison of the geometrical angle of attack α_{geo} and the effective angle of attack α at (a) $U_\infty = 11.4$ m/s and (b) $U_\infty = 20$ m/s

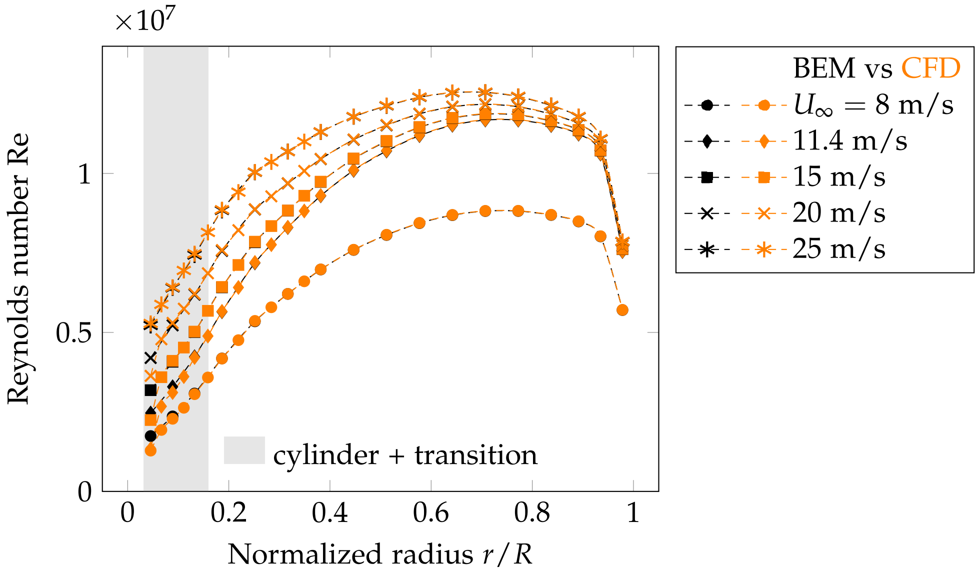

Figure 4.22: Local chord Reynolds number as a function of radius at various wind speeds

number over the whole span at various wind speeds varies within 1×10^6 and 1.3×10^7 which means that the wind turbine blade is in the critical and supercritical flow regime.

The lift and drag forces of the 3D rotating blades are, then, determined based on the effective angle of attack and the effective velocity. In order to verify the lift augmentation due to the 3D rotational effect, the lift and drag coefficients of the profiles along the wind turbine blade are compared with those of the 2D stationary airfoils (Fig. 4.23). This study assumes that the flow over the 3D rotating wind turbine blade and the flow over 2D stationary profile can be regarded as the flows with and without the 3D rotational effect, respectively. Thus, the lift augmentation is able to be identified by comparing the aerodynamic coefficients of the 3D rotating wind turbine blades and those of the 2D stationary profiles.

Figure 4.23 shows a good agreement over the entire rotor blade except the inboard blade sections. The blade sections at $r/R \geq 0.382$, which involves the DU30, DU25, DU21, and NACA64618 airfoils, experience attached flows (Fig. 4.5). This indicates no significant 3D rotational effects on the boundary layer, thus the aerodynamic coefficients agree well with the 2D stationary profile data.

The blade sections in the inboard region regarding the DU40 and DU35 airfoils are at the post-stall and pre-stall conditions based on the 2D profile data (Fig. 4.23). This implies that the inboard blade sections are expected to experience the flow separation, which is verified in Fig. 4.5. The innermost DU40 profile of the 3D rotational blade at $U_\infty = 8$ m/s, 11.4 m/s, and 15 m/s has a significant lift augmentation relative to the 2D airfoil data at deep stall. The rotating DU40 profile has a decrease in the drag coefficient relative to the 2D stationary profile data. The aerodynamic coefficients of the 3D rotating DU35 profile basically agree well with the 2D profile data in the linear attached flow region, however the lift coefficients of the rotating DU35 profile deviate from those of the 2D stationary airfoil at the angles of attack near stall. The drag coefficient of the rotating DU35 profile has no significant change. In order to understand the mechanism responsible for the change in the aerodynamic coefficients, the circumferential flow behavior, the aerodynamic characteristics, and the boundary layer properties of the rotating profiles are in-depth investigated in the following section.

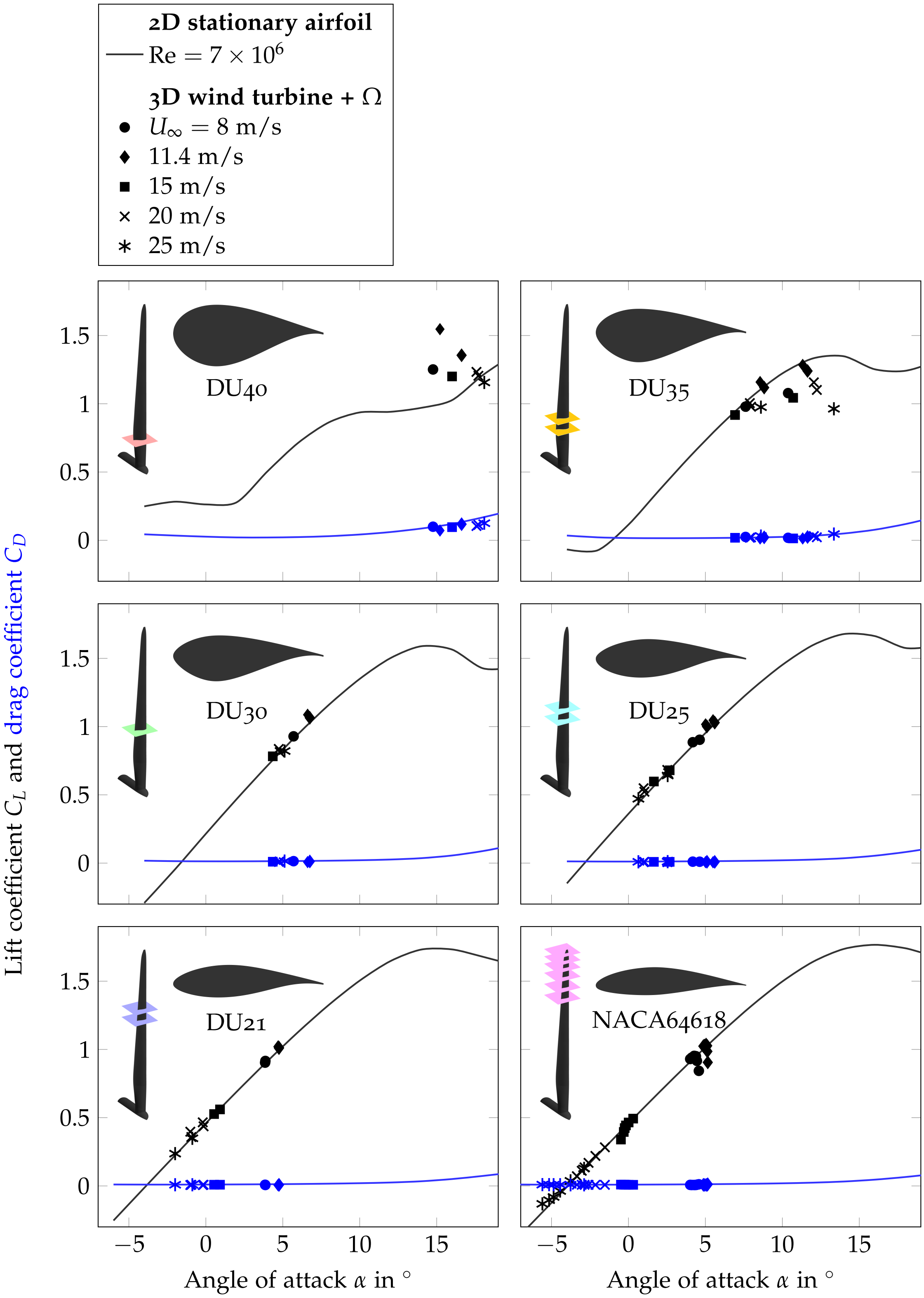

Figure 4.23: The aerodynamic coefficients of the 3D rotating wind turbine blades and the 2D stationary profiles

4.3.2 *Mechanisms of the 3D effect due to rotation*

This section aims to give an insight into the mechanisms responsible for the lift augmentation caused by the 3D effect due to rotation. The accurate 3D effect due to rotation on the circumferential flow behavior, the aerodynamic characteristics, and the boundary layer properties are thus identified by comparing the flow over the 3D rotating wind turbine blade, with that over the 2D stationary profile at the same angle of attack. Since the 2D and 3D effects due to the other mechanisms except rotation are either negligible or have been considered in the inverse BEM iterations for determining the angle of attack of the rotating wind turbine blade, flows over the 3D rotating wind turbine blade and those over the 2D stationary profile are reasonably regarded as the flows with and without the 3D rotational effect, respectively.

The flow which passes after the suction peak of a stationary airfoil undergoes an unfavorable pressure gradient and decelerates. When the flow is unable to overcome this pressure gradient, boundary layer separation occurs. Usually, the pressure distribution in the flow separation region over an airfoil is approximately constant, see e. g., Betz (1935, Fig. 21). Moreover, flows in the separated boundary layer recirculates slowly. So far, all the illustration is based on the observation of the flow over a stationary profile. Thus a question comes up: Whether the flow over a rotating profile has similar behavior as the flow over a stationary profile? The answer to this question is apparently negative since one of the most significant changes caused by the 3D effect due to rotation has been identified in Fig. 4.5, where significant radial flows in the flow separation region over the rotating blade occur. In the following, the 3D rotational effect on the flow features, aerodynamic characteristics, and the boundary layer are comprehensively and thoroughly investigated.

The streamline patterns and the dimensionless velocity magnitude contours of the flow over the 2D stationary profile and those over the 3D rotating blade at the same angles of attack are depicted in the first and second rows of Fig. 4.24 and Fig. 4.25. The velocity magnitude is normalized by a reference wind speed. The reference wind speed of the 2D stationary profile is the undisturbed wind speed in the ultimate upstream, $U_{\mathrm{ref}} = U_\infty$. The reference wind speed of the rotating wind turbine blade which considers the induced velocities is the effective wind speed, $U_{\mathrm{ref}} = U_{\mathrm{eff}}$. The flow separation over the 2D stationary profile can easily be identified by the closed streamline patterns on the upper surface. In contrast, the flow over the 3D rotating blade has no significant flow recirculation, which implies that the identification of the flow separation by means of streamline patterns in the profile planes is not inaccurate. Even though, the flow separation can be approximately identified by the low speed region near the trailing edge in the velocity magnitude contour plots. The size of the trailing edge separation of the 3D rotating blade seems smaller than that of the 2D stationary airfoil.

In order to accurately identify the 3D rotational effect on the size of the trailing edge separation, the boundary layer thickness is in depth investigated. The boundary layer thickness of the 3D boundary layer is the distance from the profile surface to the edge of the boundary layer where the total pressure difference is 99% of the total pressure difference of the undisturbed flow (Kožulović 2007)

$$\delta = n \Big|_{\Delta p_{\mathrm{t}} = 0.99 \Delta p_{\mathrm{t},\infty}} , \tag{4.11}$$

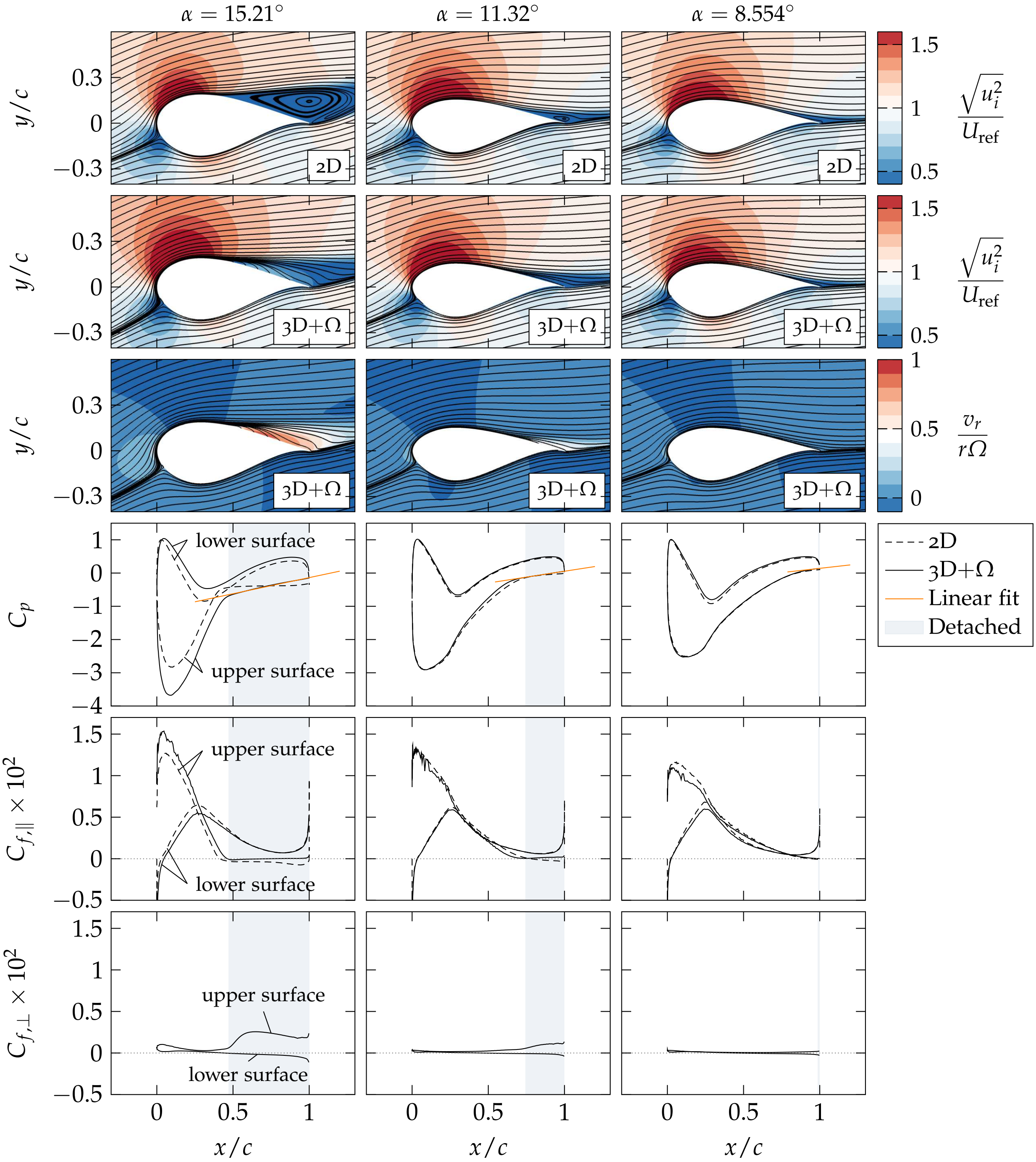

Figure 4.24: The circumferential velocity fields and the aerodynamic characteristics of the 3D rotating wind turbine blades at $U_\infty = 11.4$ m/s and the 2D stationary profiles at the same angles of attack

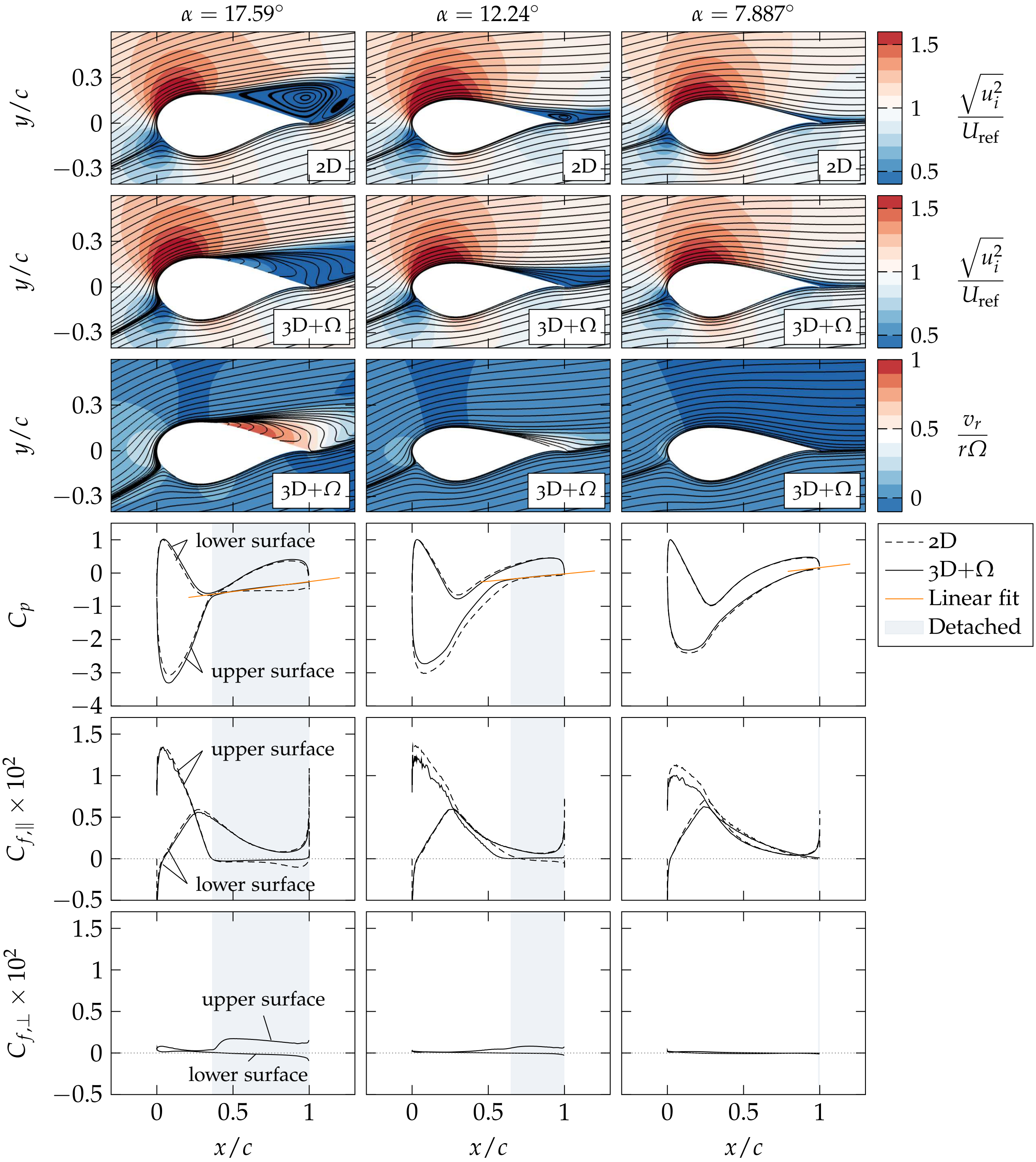

Figure 4.25: The circumferential velocity fields and the aerodynamic characteristics of the 3D rotating wind turbine blades at $U_\infty = 20$ m/s and the 2D stationary profiles at the same angles of attack

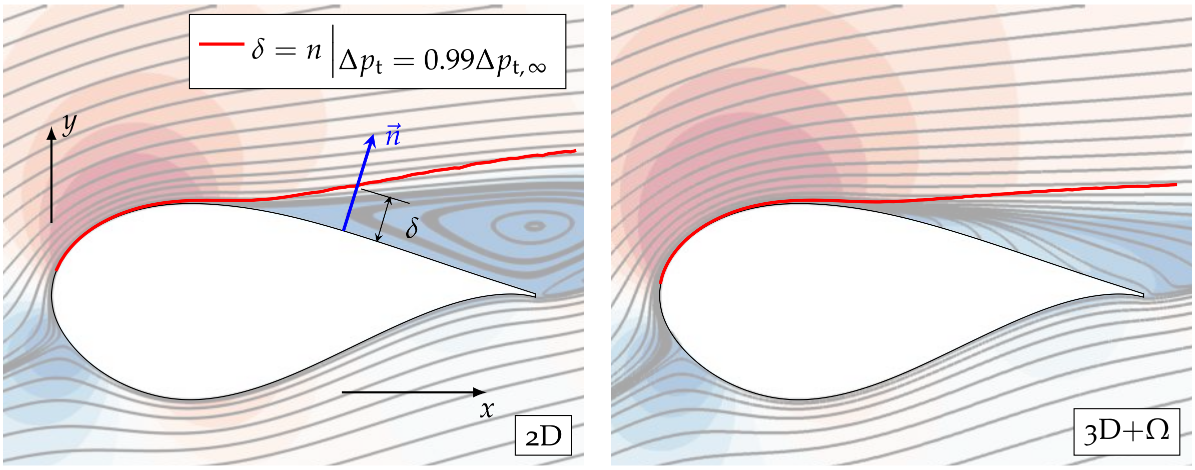

Figure 4.26: Determination of the boundary layer thickness

where n is the coordinate normal to the wall (Fig. 4.26). The total pressure difference is defined as the difference between the total pressure of the flow and the total pressure at the wall, $\Delta p_\mathrm{t} = p_\mathrm{t} - p_{\mathrm{t,w}}$. Similarly, the total pressure difference of the undisturbed flow is the difference between the total pressure of the undisturbed flow and the total pressure at the wall, $\Delta p_{\mathrm{t},\infty} = p_{\mathrm{t},\infty} - p_{\mathrm{t,w}}$.

Figure 4.27 depicts the boundary layer thickness on the suction side of the wind turbine blades, relative to that of the 2D stationary profiles at the same angles of attack. It shows that the detached flow experiences a significant change in the boundary layer thickness, whereas the attached boundary layer except that near the separation line has no significant change. For the innermost blade section of $r/R = 0.187$ at the rated wind speed of $U_\infty = 11.4$ m/s, the boundary layer thickness of the detached flow considerably decreases, which agrees with the common illustration that the 3D rotational effect results in the reduction in the size of the boundary layer separation. The boundary layer thickness at the blade section of $r/R = 0.187$ at $U_\infty = 20$ m/s has no significant change. For the blade sections at $r/R = 0.252$, the boundary layer thickness of the detached flow increases. This study posits that this increase in the size of the separation bubble is substantially caused by the mass flow coming from the blade root. The boundary layer thickness at the blade section of $r/R = 0.317$ slightly decreases near the trailing edge.

Figure 4.27 shows that the boundary layer properties of the attached flow are considerably influenced by the detached flow via viscous and turbulent shear. At the blade section of $r/R = 0.187$, the boundary layer thickness of the attached flow near the separation point decreases with the detached flow. Similarly, the boundary layer thickness of the attached flow near the separation point at $r/R = 0.252$ increases with the detached flow.

Due to the centrifugal acceleration, the flow in the bottom of the boundary layer has additional momentum relative to the stationary condition. This additional momentum in the flow separation region presents in the displacement thickness (Fig. 4.28). In contrast to the boundary layer thickness at the blade section of $r/R = 0.187$ at $U_\infty = 20$ m/s, its displacement thickness considerably decreases indicating the increase in the momentum of the detached boundary layer. Similar to the boundary layer thickness, the increase in the displacement thickness at the blade section of $r/R = 0.252$ is supposed to be caused by mass flow coming from the blade root. Only a slight change in the displacement thickness occurs at the blade section of $r/R = 0.317$ where the boundary layer is attached nearly everywhere.

Another significant difference in the overall velocity distribution around the airfoils, specifically for the innermost DU40 profile, is also observed from the contour plots of the velocity magnitude in the first and second rows of Fig. 4.24 and Fig. 4.25. The maximum velocity magnitude over the upper surface of the 3D rotating profile is considerably higher than that of the 2D stationary profile. The maximum velocity magnitude over the lower surface of the 3D rotating blade is lower than that of the 2D stationary profile. This increase in the velocity magnitude over the profile upper surface indicates a decrease in the pressure; the decrease in the velocity magnitude over the profile lower surface indicates an increase in the pressure. Because the pressure distribution is responsible for the profile aerodynamic characteristics, the pressure coefficient distributions of the 2D stationary profile and the 3D rotating blade are subsequently investigated in order to identify the 3D rotational effect on the profile aerodynamics.

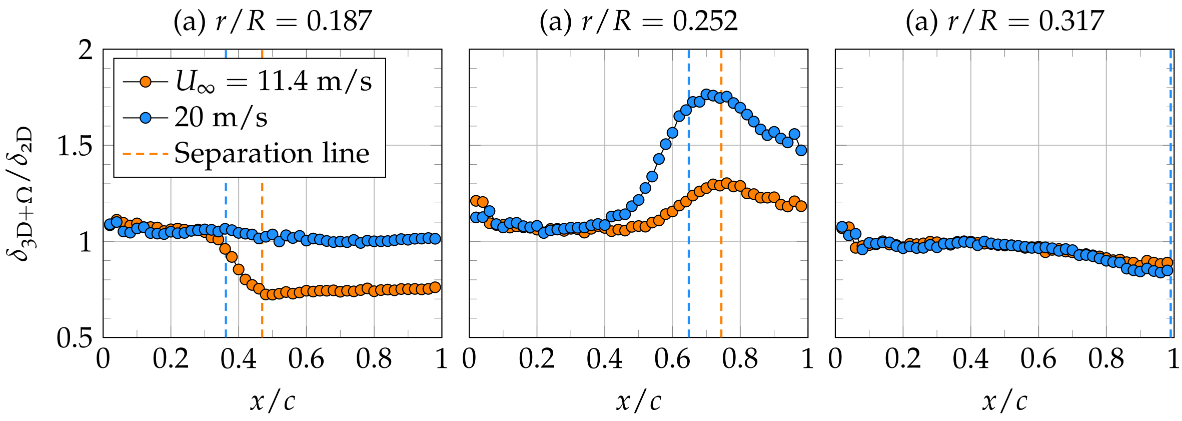

Figure 4.27: Boundary layer thickness on the suction side of the 3D rotating wind turbine blade relative to that of the 2D stationary profile

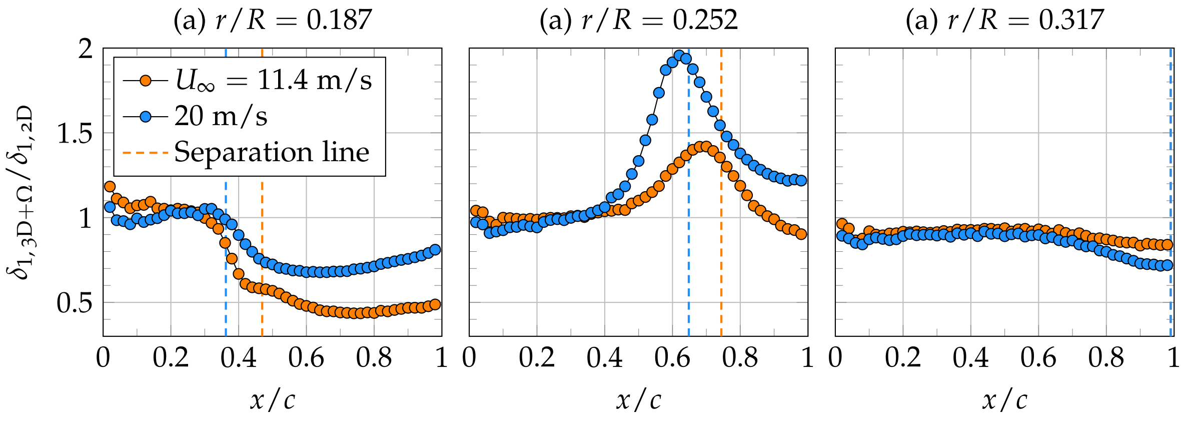

Figure 4.28: Displacement thickness on the suction side of the 3D rotating wind turbine blade relative to that of the 2D stationary profile

The pressure coefficients of the 2D stationary profile and the 3D rotating blade at the same angle of attack are depicted in the fourth rows of Fig. 4.24 and Fig. 4.25. The profile upper surface, which corresponds to the suction side has negative pressure coefficients; the profile lower surface which corresponds to the pressure side usually has positive pressure coefficients. The pressure coefficient of the 3D rotating blades is different from that of the 2D stationary profile, specifically for the innermost DU40 profile. Since the flow features of the attached and detached boundary layers are substantially different, the subsequent discussion of the change in the pressure coefficient of the attached and detached boundary layers due to the 3D rotational effect is separated.

For the attached boundary layer, the pressure coefficients on the profile upper and lower surfaces of the innermost rotating profiles decrease and increase, respectively. These changes in the pressure coefficients correspond to the change in the velocity fields, which has been discussed in the preceding paragraph. The pressure coefficient distribution also shows that the stagnation point of the 3D rotating blade shifts slightly towards the trailing edge, see the pressure peaks of the profile lower surfaces. This shift of the stagnation point agrees with the increase in the blade-bound circulation, namely the lift augmentation, due to the 3D rotational effect (Fig. 4.13 and Fig. 4.23). Because the spanwise gradient of the blade-bound circulation in the inboard region is responsible for the strength of the root vortex, this increase in the blade-bound circulation due to the 3D rotational effect may lead to an increase in the root vortex strength. In some research, such as Ronsten (1992) and Brand et al. (1997), the stagnation point is used to determine the angle of attack of the rotating blades. However, the stagnation angle method is inaccurate, specifically in the inboard region when the 3D effect due to rotation dominates the profile aerodynamics.

The pressure coefficient on the upper surface of the innermost rotating DU40 profile is considerably lower than that of the 2D stationary airfoil (see the fourth rows of Fig. 4.24 and Fig. 4.25). The pressure distributions of the rotating DU35 profiles, which are slightly further away from the rotor axis relative to the DU40 profiles, are almost identical to those of the 2D stationary profiles. This suggests that the change in the pressure distribution of the attached boundary layer due to the 3D rotational effect may be very sensitive to the radial position, or that there is another significant 2D or 3D effect dominates the aerodynamic performance of the innermost DU40 profile.

The 3D boundary layer equations (Sec. 2.2.1) show that the change in the pressure coefficients of the attached boundary layer is caused by the chordwise Coriolis acceleration due to the radial velocity components. In order to understand the correlation of the change in the pressure distribution with the chordwise Coriolis acceleration due to the radial velocity components, the radial velocity distributions over the 3D rotating blades are investigated.

The third rows of Fig. 4.24 and Fig. 4.25 show that the radial velocity components over the attached boundary layer are limited. The maximum radial velocity component takes place near the leading edge of the rotating profile, where the flow moves radially towards the blade tip. The chordwise Coriolis acceleration caused by these limited radial velocity components on the profile suction side may be responsible for the decrease in the pressure coefficients near the suction peak on the upper surface. Similarly, an increase in the pressure coefficient on the profile lower surface requires a corresponding chordwise Coriolis deceleration. This

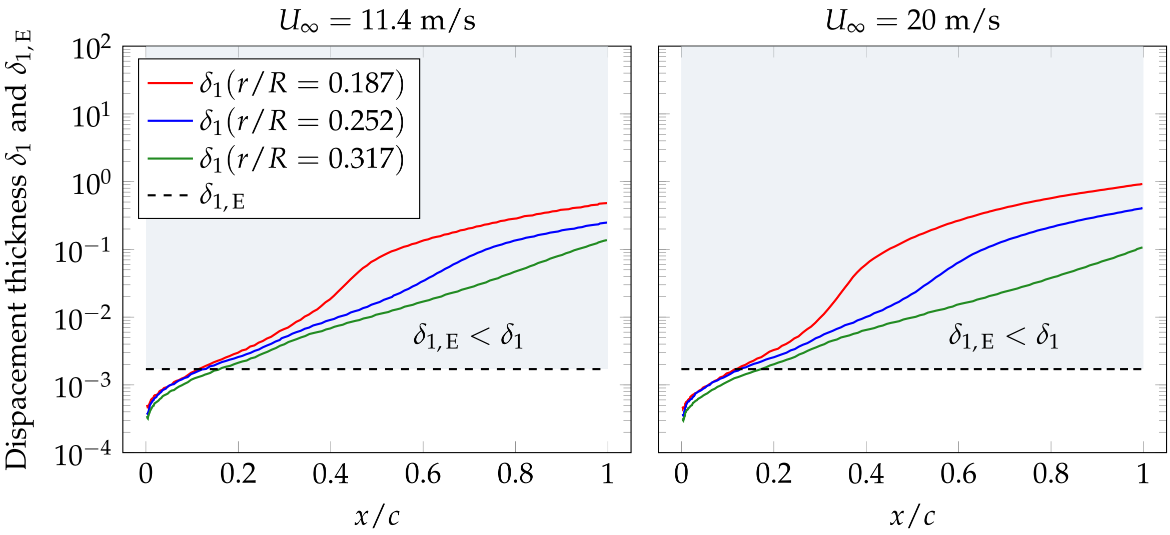

Figure 4.29: Displacement thickness of the Ekman layer and the 3D boundary layer on the suction side of the wind turbine blade

indicates that negative radial velocity components, namely radial flow towards the blade root, are essential for the cause of this deceleration. However, no significant, negative radial velocity component over the profile lower surface is observed. This suggests that there might be another significant 2D or 3D effect which influences the flow features over the 3D rotating blade.

According to the order of magnitude analysis of the attached boundary layer, the radial velocity components of the attached flow are driven by the spanwise pressure gradient and the total centrifugal acceleration. The contribution of the centrifugal acceleration on the attached boundary layer is estimated using the criterion of Früh and Creech (2015), who suggested that the rotational augmentation occurs

$$\text{if and only if } \delta_{1,\mathrm{E}} < \delta_1, \tag{4.12}$$

where

$$\delta_{1,\mathrm{E}} = \frac{1}{2}\sqrt{\frac{\nu}{\Omega}} \tag{4.13}$$

is the displacement thickness of the Ekman layer and δ_1 is the displacement thickness of the boundary layer. The displacement thickness of the Ekman layer is dependent only on the fluid properties and the rotational speed, and is approximately $1.71 \times 10^{-3} \sim 1.96 \times 10^{-3}$ for the baseline wind turbine. The displacement thickness of the 3D boundary layer on the suction side of the rotating profile is evaluated and depicted in Fig. 4.29. Except the region near the leading edge, almost the entire profile satisfies Früh's criterion. This suggests that these wind turbine blade sections experience the 3D rotational effect considerably. However, the limited change in the lift coefficient (Fig. 4.23) and the pressure coefficient distribution (the fifth rows of Fig. 4.24 and Fig. 4.25) of the rotating profiles at $r/R = 0.252$ and 0.317 contradict this statement.

The fourth rows of Fig. 4.24 and Fig. 4.25 also show that the pressure coefficients of the 3D rotating profiles increase gradually from the separation point towards the trailing edge, whereas the 2D stationary airfoils have typically flat pressure distributions in the flow separation region. This chordwise pressure gradient in the flow separation of the rotating blade indicates a failure to identify the flow separation region by means of the flat pressure distribution. Thus a reliable method for determining the onset of the flow separation is required.

The flow in the detached boundary layer over the 2D stationary profile recirculates due to the momentum transported from the external flow via the viscous and turbulent shear near the edge of the boundary layer. This shear flow drives the upper part of the detached boundary layer to move chordwise towards the trailing edge. Meanwhile, the lower part of the detached boundary layer moves chordwise towards the leading edge. This reverse flow on the bottom of the detached boundary layer then departs from the profile surface near the separation point, and joins to the upper part of the detached boundary layer. This reverse flow on the bottom of the detached boundary layer leads to negative skin friction coefficients, which is defined as positive towards the trailing edge. Although the detached boundary layer over the rotating blade has no significant reverse flow (the second rows of Fig. 4.24 and Fig. 4.25), the skin friction coefficient is in any case investigated.

In this study, the skin friction coefficient is divided into two components. The component parallel to the profile plane is called the in-plane skin friction coefficient $C_{f,\parallel}$. The other component perpendicular to the profile plane is called the out-of-plane skin friction coefficient $C_{f,\perp}$. The in-plane skin friction coefficient of the 2D stationary airfoil and the 3D rotating airfoil are depicted in the fifth rows of Fig. 4.24 and Fig. 4.25. The increase in the in-plane skin friction coefficient on the upper surface of the 3D profiles, relative to the 2D stationary profiles represents an increase in the chordwise velocity, agreeing with the decrease in the pressure coefficient. Similarly, the decrease in the in-plane skin friction coefficient of the lower surface of the rotating profiles corresponds to the decrease in the velocity magnitude and the increase in the pressure coefficients on the pressure side.

The in-plane skin friction coefficients of the detached flow over the 2D stationary airfoil are slightly negative due to the reverse flow, whereas the in-plane skin friction coefficients of the detached flow over the 3D rotating profiles are approximately zero and have no significant negative quantities. The in-plane skin friction coefficient of the detached flow becomes even positive near the trailing of the rotating DU35 profiles. Similar positive values of the chordwise skin friction coefficients were also observed by Guntur and Sørensen (2015, Fig. 7). These positive in-plane skin friction coefficients agree with the streamline patterns adjacent to the suction side of the baseline wind turbine blade (Fig. 4.5), showing that the detached flow moves radially outwards, accompanying with slightly chordwise movement towards to the trailing edge.

This positive in-plane skin friction coefficient implies the uncertainty of using the in-plane skin friction coefficient criterion, $c_{f,\parallel} \leq 0$, to identify the flow separation over the 3D rotating blades. Thus this study proposes a new criterion

$$\frac{\mathrm{d}C_{f,\parallel}}{\mathrm{d}x} = 0 \qquad \text{and} \qquad \frac{\mathrm{d}^2 C_{f,\parallel}}{\mathrm{d}x^2} > 0, \tag{4.14}$$

as an alternative way to determine the onset of the boundary layer separation when the conventional criterion, $C_{f,\parallel} \leq 0$, fails. The first relationship of this new criterion indicates that the flow separation point is at the position where the chordwise gradient of the in-plane skin fric-

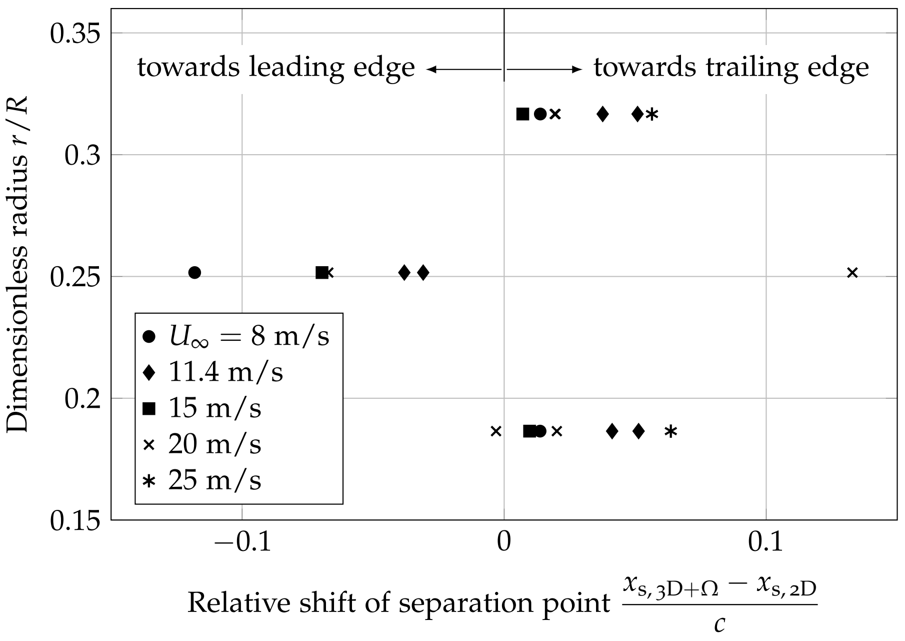

Figure 4.30: Comparison of the separation points on the 3D rotating wind turbine blade relative to those of the 2D stationary profiles at the same angles of attack

tion coefficient on the profile suction side is equal to zero. The second relationship is specified in order to exclude the suction peak.

The significant out-of-plane skin friction coefficients in the flow separation region (the sixth rows of Fig. 4.24 and Fig. 4.25) agree with the significant radial flows observed in Fig. 4.5. The spanwise skin friction coefficient increases abruptly after entering the flow separation region, and then decreases slightly toward the trailing edge. There are also slight skin friction coefficients in the attached boundary layer which agrees with the slight radial velocity component over the attached boundary layer (the third rows of Fig. 4.24 and Fig. 4.25).

In order to verify the common description that the 3D rotational effect leads to the shift of the separation point towards the trailing edge, the separation point is in depth investigated. Figure 4.30 depicts the position of the separation point of the rotating blade relative to that of the stationary profile at the same angle of attack. It shows that the separation points of the blade sections at $r/R = 0.187$ and 0.317 slightly shift towards the trailing edge up to 6% of the blade chord, agreeing with the common illustration that the 3D rotational effect results in the delay of separation lines. However, the separation points of the blade sections at $r/R = 0.252$ shift towards the leading edge up to 10% of the blade chord. The advance of the separation point toward the leading edge might be, as Corten (2001) suggested, caused by the significant radial flow in the detached boundary layer from the blade root.

In the preceding paragraph, it has been shown that there are limited radial velocity components of the attached flow and significant radial velocity components in the detached boundary layer (the third rows of Fig. 4.24 and Fig. 4.25). According to the order of magnitude analysis of the attached and detached boundary layers (Sec. 2.2.1 and Sec. 2.2.3), the total centrifugal acceleration and the spanwise pressure gradient are the sources responsible for the radial velocity components. The predominant source among them is discussed in the following paragraphs.

The spanwise pressure gradient is estimated by Corten (2001) by neglecting the second and the third terms of Eq. (2.54). The accuracy of this estimation is verified in this study. The first column of Fig. 4.31 presents pressure coefficient distributions on the profile suction sides without and with the 3D rotational effect. The pressure coefficient without the 3D rotational effect is obtained by interpolating the 2D stationary profile data at the same angles of attack as the 3D rotating wind turbine blade; the pressure distribution with the 3D rotational effect is obtained from the 3D CFD results. The separation line is also depicted in Fig. 4.31 with a dashed line. The pressure coefficient distributions show that the suction peak is more significant in the inboard region. The estimation of the spanwise pressure gradient by neglecting the second and the third terms of Eq. (2.54) is quite accurate in the outboard region since the spanwise gradient of the pressure coefficient, $\partial C_p/\partial r$, is very small and negligible (the second column of Fig. 4.31). However, this estimation is inaccurate in the inboard region where the considerable spanwise gradient of the pressure coefficient should be taken into account (the second column of Fig. 4.31). Thus this study does not suggest to use the method adopted by Corten (2001) to estimate the spanwise pressure gradient, particularly in the inboard region.

In order to avoid any loss of the accuracy of illustrating the spanwise pressure gradient, a modified pressure coefficient

$$C_{p,\,\mathrm{mod}} = \frac{p - p_{\mathrm{ref}}}{\frac{1}{2}\rho U_\infty^2}, \tag{4.15}$$

which uses the free-stream wind speed to define the reference dynamic pressure is considered. Since the spanwise pressure gradient can be described by the spanwise gradient of the modified pressure coefficient

$$\frac{\partial p}{\partial r} = \frac{1}{2}\rho U_\infty^2 \frac{\partial C_{p,\,\mathrm{mod}}}{\partial r}, \tag{4.16}$$

the spanwise gradient of the modified pressure coefficient is accurate to present the spanwise pressure gradient.

The modified pressure coefficient distribution shows that the pressure on the profile suction near the blade tip is much lower than the inboard region (the third column of Fig. 4.31). Aside from the flow separation region and near the trailing edge, almost the entire profile suction side undergoes negative spanwise pressure gradients (the fourth column of Fig. 4.31), which indicates that the flow passing over the profile suction side accelerates radially towards the blade tip. However, the order of magnitude analysis of the attached boundary layer (Sec. 2.2.1) shows that the influence of the spanwise pressure gradient relative to the predominant, chordwise convective term is of the order of c/r. This fraction of c/r represents the period of time for the flow to pass over the profile, thus the effect of the spanwise pressure gradient is inversely proportional to the radius and only significant near the blade root. The fourth column of Fig. 4.31 also shows an important fact that the spanwise pressure gradient of the 3D rotating blades in the inboard region is more moderate than that of the 2D prediction. This moderation in the spanwise pressure gradient is the consequence of the decrease in the pressure on the profile suction side (the fourth rows of Fig. 4.24 and Fig. 4.25).

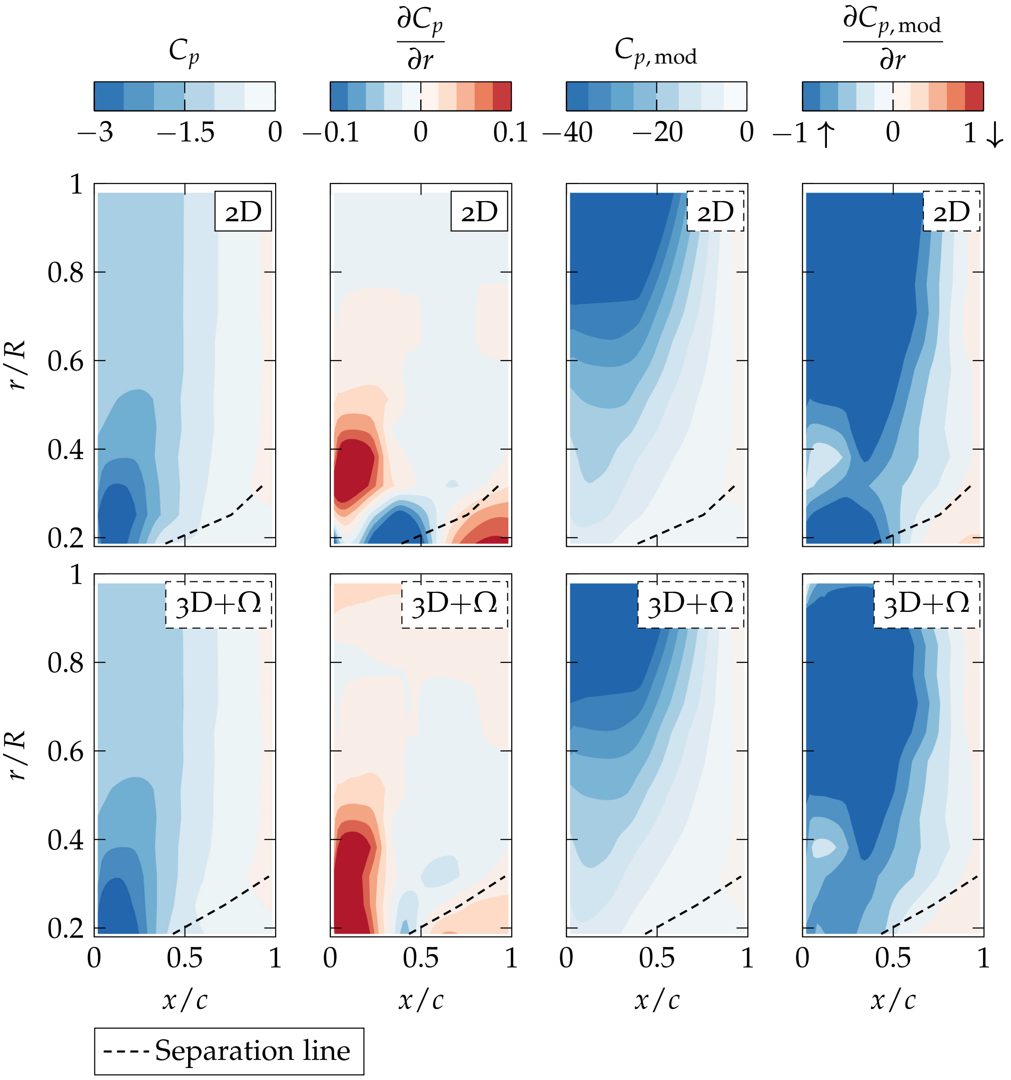

Figure 4.31: The pressure distribution on the blade suction side estimated from the 2D stationary profile data and evaluated from the 3D rotating wind turbine blade at $U_\infty = 11.4$ m/s

The positive spanwise pressure gradient in the flow separation region indicates radially-inward acceleration (the fourth column of 4.31). Thus the radial velocity in the flow separation region driven by the centrifugal acceleration and the limited spanwise pressure gradient should be less than $r\Omega$, agreeing with the contour plots of the radial velocity components in the third rows of Fig. 4.24 and Fig. 4.25. This positive spanwise pressure gradient in the flow separation region also indicates the inaccuracy of Corten (2001) model, who simply used the pressure coefficient to estimate the spanwise pressure gradient and derived that the radial velocity in the separation region of the rotating profile is $v_r = r\Omega\sqrt{1 - C_p}$. Since the pressure coefficient in the flow separation region is negative, the radial velocity component is over-predicted by Corton and higher than $r\Omega$.

In order to accurately identify the predominant source resulting in the radial flow on the profile suction side, this study explicitly investigates the spanwise acceleration due to the spanwise pressure gradient and the total centrifugal force in the r-momentum equation. Since

(a) Spanwise acceleration at the edge of the boundary layer

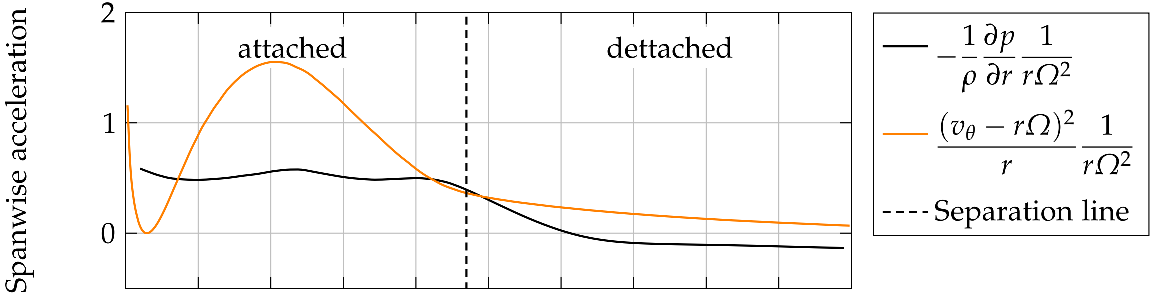

(b) Total centrifugal acceleration in the boundary layer

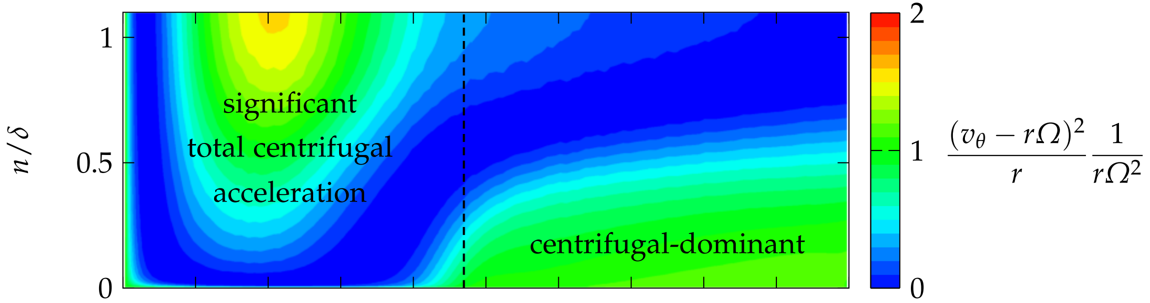

(c) Circumferential velocity in the boundary layer

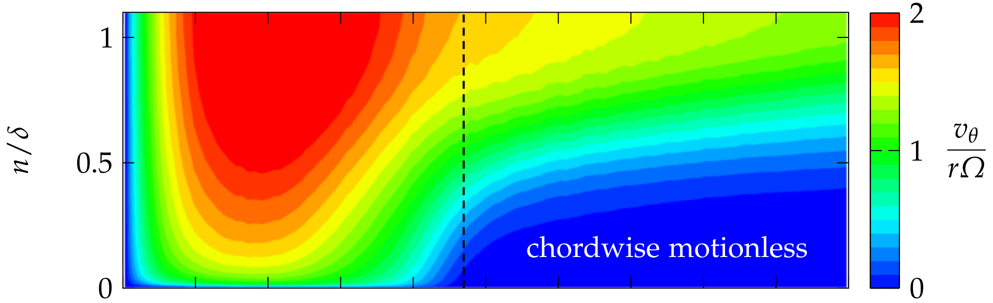

(d) Radial velocity in the boundary layer

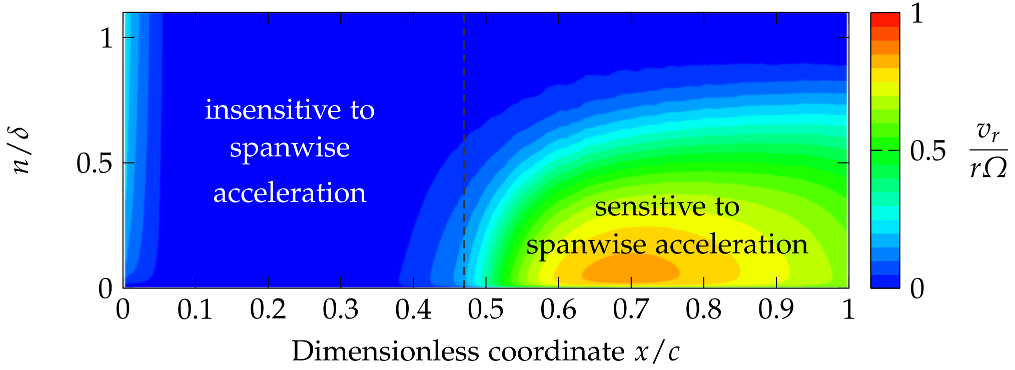

Figure 4.32: Spanwise acceleration and velocity components in the boundary layer on the suction side of the wind turbine blade at $r/R = 0.176$ and $U_\infty = 11.4$ m/s

the mechanisms responsible for the 3D rotational effect on the boundary layers at different blade sections are similar (Appendix B), this section only presents the boundary layer of the blade section at $r/R = 0.187$ at the wind speed of $U_\infty = 11.4$ m/s.

Figure 4.32 (a) depicts the spanwise accelerations due to the spanwise pressure gradient and the total centrifugal force at the edge of the boundary layer, where the spanwise accelerations are normalized by the centrifugal acceleration, $r\Omega^2$. Because the pressure gradient normal to the profile surface is approximately zero in the boundary layer, the spanwise acceleration due to the spanwise pressure gradient at the edge of the boundary layer also represents that in the boundary layer.

Figure 4.32 (a) shows that at the edge of the attached boundary layer the total centrifugal acceleration is higher than the spanwise acceleration due to the spanwise pressure gradient, thus the total centrifugal acceleration is supposed to be a more dominant source contributing to the radial velocity components in the attached boundary layer. At the edge of the detached boundary layer, both the spanwise accelerations are very small. The spanwise acceleration due to the spanwise pressure gradient is even negative, which has been demonstrated in Fig. 4.31, indicating radially inward acceleration. These limited spanwise accelerations due to the total centrifugal force and the spanwise pressure gradient at the edge of the detached boundary layer cannot explain the significant radial flow in the flow separation region. The spanwise acceleration in the boundary layer are further investigated.

Figure 4.32 (b) depicts the total centrifugal acceleration in the boundary layer and shows that the total centrifugal acceleration in the attached boundary layer decreases gradually approaching the profile surface. The total centrifugal acceleration in the detached boundary layer, however, shows a totally different distribution. The lower part of the detached boundary layer has a significant total centrifugal acceleration, whereas the upper part of the detached boundary layer has no significant total centrifugal acceleration.

The total centrifugal acceleration comprises the centrifugal acceleration, the coordinate curvature acceleration, and the Coriolis acceleration (see Sec. 2.2.2). Except the centrifugal acceleration, all the other terms involve the circumferential velocity. The circumferential velocity components in the boundary layer are depicted in Fig. 4.32 (c). The good correlation between the total centrifugal acceleration and the circumferential velocity in the boundary layer explicitly demonstrates that the circumferential velocity, or more specifically the coordinate curvature term, dominates the total centrifugal acceleration in the attached boundary layer. Additionally, the flow in the lower part of the detached boundary layer is only driven by the centrifugal acceleration because of the negligible chordwise velocity. This evidence supports the validity of Corten's model which neglects the coordinate curvature term and the Coriolis terms in the r-momentum equation (Eq. 2.74).

Although both the attached and detached boundary layers have significant spanwise acceleration, the effects of the spanwise acceleration on the attached and detached boundary layers are substantially different. Figure 4.32 (d) shows that the significant spanwise acceleration in the attached boundary layer yields no significant radial velocity. In contrast, the centrifugal acceleration effectively yields significant radial velocity components in the detached boundary layer. Because of the limited radial velocity components in the attached boundary layer, this

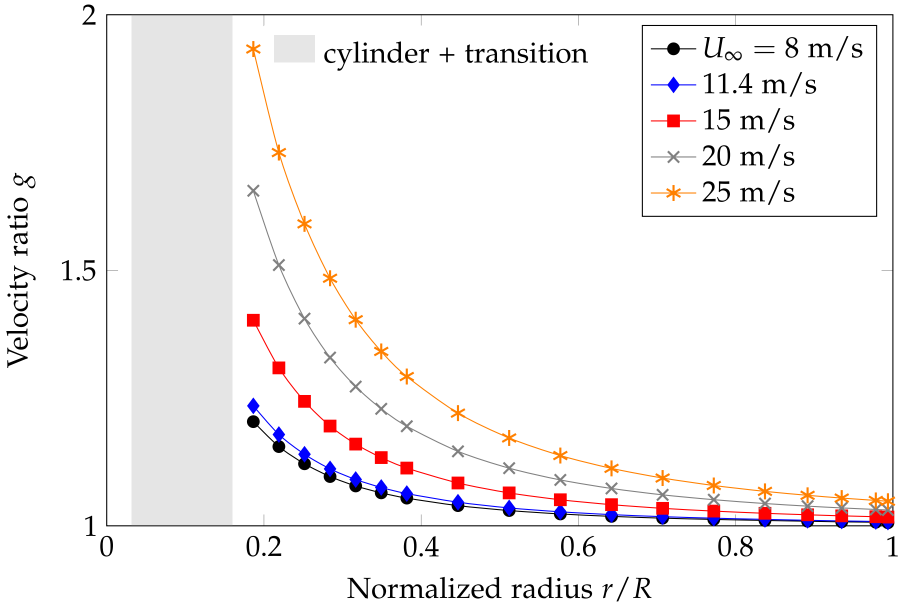

Figure 4.33: The velocity ratio as a function of normalized radius (RANS computations)

study rationally posits that the significant change in the pressure distribution in the attached boundary layer (the fourth rows of Fig. 4.24 and Fig. 4.25) are caused by other 2D or 3D effects.

The remainder of this section is the verification of the analytical expression (Eq. 2.84) derived in this study for the prediction of the pressure distribution in the flow separation region. Since it has been shown that the spanwise pressure gradient in the flow separation region is limited (Fig. 4.31), it is valid to neglect the spanwise pressure gradient in the r-momentum equation for deriving Eq. (2.84).

The fourth rows of Fig. 4.24 and Fig. 4.25 show that the pressure coefficient distribution along the blade chord in the flow separation region is nearly a linear relationship. This study determines the chordwise gradient of the pressure coefficient in the flow separation region by finding the slope of a fitted line through the pressure coefficients in the flow separation region (the orange lines in the fifth rows of Fig. 4.24 and Fig. 4.25).

Equation (2.84) shows that the chordwise gradient of the pressure coefficient is dependent on the chord-to-radius ratio and the velocity ratio. The velocity ratio along the rotor blade is evaluated and depicted in Fig. 4.33. Basically, the velocity ratio decreases with radius and approaches one near the blade tip. The velocity ratio varies with the operating condition, and reaches the maximum value up to 2 at the innermost blade section of the baseline wind turbine. With the given chord-to-radius ratio, the chordwise gradient of the pressure coefficient in the flow separation region as a function of the velocity ratio is depicted in Fig. 4.34 according to Eq. (2.84). Figure 4.34 also depicts the chordwise gradient of the pressure coefficient in the flow separation region of the rotating blade sections at at $r/R = 0.187$ and 0.252 evaluated from the 3D CFD results. The overall good agreement between the 3D CFD results and the analytical expression supports the explanation of the mechanism responsible for the pressure gradient in the flow separation region caused by the 3D effect due to rotation: The centrifugal force accelerates the chordwise motionless flow in the bottom of the detached boundary layer radially towards the blade tip. A chordwise Coriolis acceleration is then induced by Coriolis

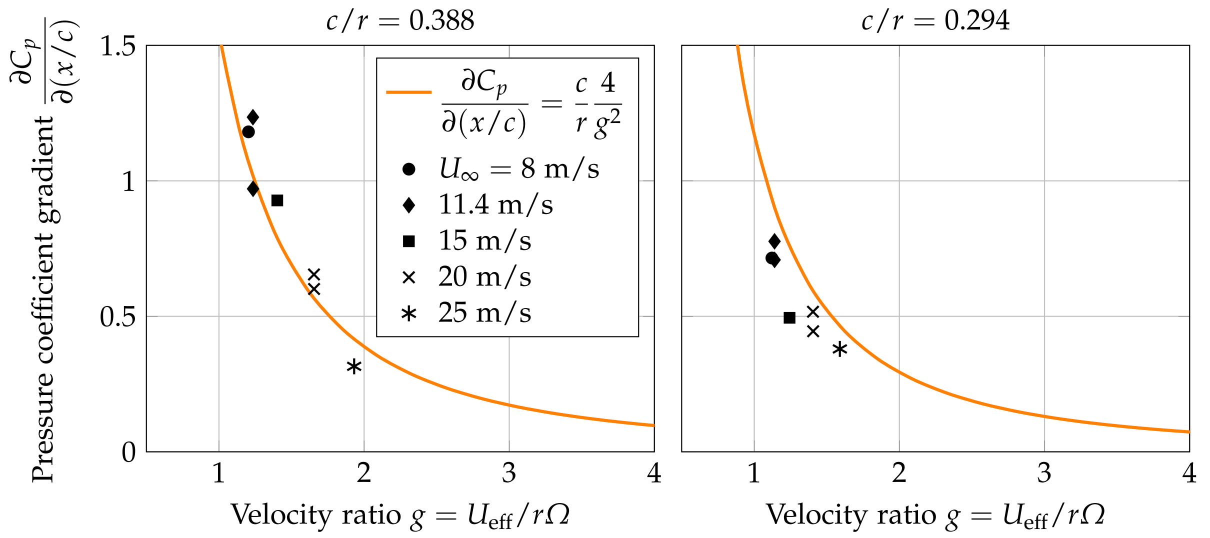

Figure 4.34: The chordwise gradient of the pressure coefficients in the flow separation region of the 3D rotating wind turbine blade in comparison with the analytical expression

effect on the radial velocity component. However, the chordwise Coriolis acceleration is balanced by a chordwise pressure gradient. This chordwise pressure gradient leads to a pressure drop on the profile suction side and results in lift augmentation.

5

CONCLUSIONS AND FUTURE WORK

5.1 CONCLUSIONS

This section draws conclusions from this work contributing to the understanding of the inboard complex flows, the 3D effect due to rotation, and its mechanisms based on a numerical investigation of the inboard flow of a horizontal axis wind turbine.

Not only helical root vortices, trailing vortices, flow separation, unsteady von Kármán vortex streets, pairs of counter-rotating vortices, and a low-speed nacelle wake but also the horseshoe vortices which wrap around the blade roots adjacent to the spinner are identified in this study. The origin of the root vortex of the baseline wind turbine is at the blade transition section, rather than at the blade section of maximum chord length. This thesis demonstrates that the formation of the root vortex is closely associated with the sudden drop in the blade-bound circulation. The strength and life span of the root vortex are substantially dependent on the tip speed ratios. The origin of the pair of counter-rotating vortices is identified at the base of the blade roots, similar to the base vortices of a cylinder adjacent to a flat plate.

The hub design only has limited influence on the overall and local wind turbine aerodynamic performance, agreeing with prior publications.

The 3D effect due to rotation only results in limited power overshoot of the pitch-controlled horizontal axis wind turbine. The lift augmentation caused by the 3D effect due to rotation is significant in the inboard region where flow separation with significant radial flows towards the blade tip occurs. This study shows that the 3D rotational effect on the flow features, aerodynamic characteristics, and boundary layer properties of the attached boundary layer is distinctly different from those of the detached boundary layer.

The 3D effect due to rotation only yields the limited radial velocity components, which are basically driven by the total centrifugal acceleration and the spanwise pressure gradients. These induced radial velocity components then induce chordwise Corolis acceleration which may eventually result in changes in aerodynamic characteristics such as the decrease in pressure on the profile suction side. This decrease in pressure mitigates the spanwise pressure gradient, whose effect is carefully studied in the present work.

In contrast to attached flow, the 3D effect due to rotation yields significant radial velocity components in the bottom of the flow separation reigon, which are substantially driven by the centrifugal force and the negligible spanwise pressure gradients. These radial velocity components then induce chordwise Coriolis acceleration. However, a chordwise pressure gradient occurs which balances this chordwise Coriolis acceleration.

This study specifically contributes to the accurate prediction of the pressure distribution in the flow separation region of a rotating blade. An analytical expression of the chordwise gradient of the pressure coefficient as a function of the chord-to-radius ratio and the velocity ratio is derived from Corten's model by a physically based simplification.

This study also demonstrates that the 3D rotational effect may result in the shift of separation point towards the leading edge, due to the significant radial flow in the bottom of the detached boundary layer as Corten posited. Furthermore, it is possible that the 3D rotational effect leads to an increase in the boundary layer thickness, due to the increasing mass flow in the flow separation region from the blade root.

5.2 FUTURE WORK

This work is concluded by putting forward a number of further research suggestions to build on the existing work. These suggestions stem from the findings and recommendations of this study. Researchers may choose to pursue some of these suggestions to further contribute to the wind turbine aerodynamics. Those are discussed below.

The current work reconsiders as many as possible 2D/3D effects and estimates the extent of their effects on the flows over horizontal axis wind turbines. Based on this estimation, the 3D rotational effects could be identified accurately by comparing the flows over the 3D rotating wind turbine blades and those over the 2D stationary profiles. However, the current results show that the significant change in the inboard aerodynamic performance, specifically in the attached boundary layers, is far beyond the extent of the 3D effect due to rotation. The 2D/3D effects due to the blade cascade and blade solidity may be prominent in the inboard region and need to be addressed by future studies, in order to develop a more reliable engineering correction model.

Although the analytical expression derived in this study agrees well with the computational results, it still needs to be verified by experimental measurements. The current CFD model assumes that the boundary layer over the baseline wind turbine is fully turbulent. Thus, further research seeking to identify the sensitivity of laminar separation bubbles and laminar-turbulent transition to the 3D rotational effects is needed.

BIBLIOGRAPHY

Akay, B.; Ragni, D.; Ferreira, C.J. Simao and van Bussel, G.J.W. (2013): Experimental investigation of the root flow in a horizontal axis wind turbine. In: Wind Energy, Vol. 17(7):pp. 1093–1109.

Bak, C.; Johansen, J. and Andersen, P.B. (2006): Three-dimensional corrections of airfoil characteristics based on pressure distributions. In: Proceedings of the European Wind Energy Conference and Exhibition (EWEC). Athens, Greece.

Banks, W.H.H. and Gadd, G.E. (1963): Delaying effect of rotation on laminar separation. In: AIAA journal, Vol. 1(4):pp. 941–942.

Bazilevs, Y.; Hsu, M.C.; Akkerman, I.; Wright, S.; Takizawa, K.; Henicke, B.; Spielman, T. and Tezduyar, T.E. (2011): 3D simulation of wind turbine rotors at full scale. Part I: Geometry modeling and aerodynamics. In: International Journal for Numerical Methods in Fluids, Vol. 65(1-3):pp. 207–235.

Betz, A. (1935): Applied Airfoil Theory. In: Durand, W. (editor) Aerodynamic Theory, Berlin Julius Springer, Vol. IV.

Björck, A.; Thor, S.-E.; Fiddes, S.P.; Brand, A.J. and Rasmussen, F. (1994): Dynamic stall and 3D effects. In: 5th European Wind Energy Association Conference and Exhibition. Thessaloniki, Greece.

Boorsma, K. and Schepers, J. (2003): Description of experimental setup MEXICO measurements. Technical report ECN-X-11-120, The Energy Research Center of the Netherlands ECN.

Brand, A.; Dekker, J.; de Groot, C. and Spaeth, M. (1997): Field rotor-aerodynamics: The rotating case. In: 35th Aerospace Sciences Meeting and Exhibit. American Institute of Aeronautics and Astronautics, Reno, NV, USA.

Breton, S.P.; Coton, F.N. and Moe, F. (2008): A study on rotational effects and different stall delay models using a prescribed wake vortex scheme and NREL phase VI experiment data. In: Wind Energy, Vol. 11(5):pp. 459–482.

Buhl, M.L. (2005): A new empirical relationship between thrust coefficient and induction factor for the turbulent windmill state. Technical report NREL/TP-500-36834, National Renewable Energy Laboratory, USA.

Burton, T.; Jenkins, N.; Sharpe, D. and Bossanyi, E. (2011): Wind Energy Handbook. John Wiley & Sons, Ltd, second edition.

Butterfield, C.P.; Simms, D.A.; Musial, W.P. and Scott, G.N. (1990): Spanwise aerodynamic loads on a rotating wind turbine blade. Technical report SERI/TP-257-3983, Solar Energy Research Institute, USA.

Carcangiu, C.E.; Sørensen, J.N.; Cambuli, F. and Mandas, N. (2007): CFD–RANS analysis of the rotational effects on the boundary layer of wind turbine blades. In: Journal of Physics: Conference Series, Vol. 75(012031).

Chaviaropoulos, P.K. and Hansen, M.O.L. (2000): Investigating three-dimensional and rotational effects on wind turbine blades by means of a quasi-3D Navier-Stokes solver. In: Journal of Fluids Engineering, Vol. 122:pp. 330–336.

Chow, R. and van Dam, C.P. (2012): Verification of computational simulations of the NREL 5 MW rotor with a focus on inboard flow separation. In: Wind Energy, Vol. 15(8):pp. 967–981.

Chow, R. and van Dam, C.P. (2013): Computational investigations of blunt trailing-edge and twist modifications to the inboard region of the NREL 5 MW rotor. In: Wind Energy, Vol. 16(3):pp. 445–458.

Corbetta, G.; Pineda, I.; Moccia, J. and Guillet, J. (2014): The European offshore wind industry - key trends and statistics 2013.

Corten, G.P. (2001): Flow Separation on Wind Turbine Blades. PhD dissertation, Utrecht University Netherlands.

Du, Z. and Selig, M.S. (1998): A 3-D stall-delay model for horizontal axis wind turbine performance prediction. In: 1998 ASME Wind Energy Symposium. Reno, NV, USA, AIAA-98-0021, pp. 9–19.

Du, Z. and Selig, M.S. (2000): The effect of rotation on the boundary layer of a wind turbine blade. In: Renewable Energy, Vol. 20:pp. 167–181.

Dumitrescu, H. and Cardoş, V. (2009): Inboard boundary layer state on wind turbine blades. In: ZAMM Zeitschrift für Angewandte Mathematik und Mechanik, Vol. 89(3):pp. 163–173.

Dumitrescu, H. and Cardoş, V. (2010): The turbulent boundary layer on wind turbine blades. In: Proceedings of the Romanian Academy, Series A. Vol. 11, pp. 125–136.

Dumitrescu, H.; Cardoş, V. and Dumitrache, A. (2007): Modelling of inboard stall delay due to rotation. In: Journal of Physics: Conference Series, Vol. 75(012022).

Dwyer, H.A. and McCroskey, W.J. (1970): Crossflow and unsteady boundary-layer effects on rotating blades. In: AIAA 8th Aerospace Sciences Meeting. New York.

Ebert, P.R. and Wood, D.H. (2001): The near wake of a model horizontal-axis wind turbine - Part 3: properties of the tip and hub vortices. In: Renewable Energy, Vol. 22:pp. 461–472.

Eggers, A.J.; Chaney, K. and Digumarthi, R. (2003): An assessment of approximate modeling of aerodynamic loads on the UAE rotor. In: 41st Aerospace Sciences Meeting and Exhibit. Reno, Nevada, AIAA-2003-0868.

European Wind Energy Association (2013): 2030: the next steps for EU climate and energy policy.

Fiedler, H.E. (1987): Coherent structures. In: Advances in Turbulence, pp. 320–336.

Fogarty, L.E. (1951): The laminar boundary layer on a rotating blade. In: Journal of the Aeronautical Sciences, Vol. 18(4):pp. 247–252.

Früh, W.G. and Creech, A.C.W. (2015): A criterion for rotational augmentation based on a boundary-layer analysis. In: International Conference on Renewable Energies and Power Quality. La Coruna, Spain.

Gasch, R. and Twele, J. (2010): Windkraftanlagen. Springer Vieweg, 6. edition.

Glauert, H. (1935): Division L: Airplane Propellers. In: Durand, W.F. (editor) Aerodynamic Theory, Berlin Julius Springer, Vol. IV.

Goldstein, S. (1948): On laminar boundary-layer flow near a position of separation. In: Quarterly Journal of Mechanics and Applied Mathematics, Vol. 1(1):pp. 43–69.

Guntur, S. and Sørensen, N.N. (2015): A study on rotational augmentation using CFD analysis of flow in the inboard region of the MEXICO rotor blades. In: Wind Energy, Vol. 18(4):pp. 745–756.

Gutsche, F. (1940): Versuche an umlaufenden Flügelschnitten mit abgerissener Strömung.

Hand, M.M.; Simms, D.A.; Fingersh, L.J.; Jager, D.W.; Cotrell, J.R.; Schreck, S. and Larwood, S.M. (2001): Unsteady Aerodynamics Experiment Phase VI : Wind Tunnel Test Configurations and Available Data Campaigns. Technical report NREL/TP-500-29955, National Renewable Energy Laboratory, USA.

Hansen, M.O.L. (2008): Aerodynamics of Wind Turbines. Earthscan, second edition.

Hansen, M.O.L.; Michelsen, J.A. and Sorensen, N.N. (1994): Navier-Stokes solver for rotating wing. In: 5th European Wind Energy Association conference and exhibition. Thessaloniki, Greece.

Hansen, M.O.L.; Sørensen, N.N.; Sørensen, J.N. and Michelsen, J.A. (1997): Extraction of lift, drag and angle of attack from computed 3-D viscous flow around a rotating blade. In: European Wind Energy Conference. Dublin, pp. 499–502.

Herráez, Iván; Stoevesandt, Bernhard and Peinke, Joachim (2014): Insight into Rotational Effects on a Wind Turbine Blade Using Navier–Stokes Computations. In: Energies, Vol. 7(10):pp. 6798–6822.

Himmelskamp, H. (1950): Profiluntersuchungen an einem umlaufenden Propeller. Mitteilungen aus dem Max-Planck-Institut für Strömungsforschung, Max-Planck-Institut für Strömungsforschung, Göttingen.

Hu, D.; Hua, O. and Du, Z. (2006): A study on stall-delay for horizontal axis wind turbine. In: Renewable Energy, Vol. 31(6):pp. 821–836.

Hunt, J. (1987): Vorticity and vortex dynamics in complex turbulent flows. In: Proc. CANCAM, Trans. Can. Soc. Mec. Engrs. Vol. 11, pp. 21–35.

Jeong, J. and Hussain, F. (1995): On the identification of a vortex. In: Journal of Fluid Mechanics, Vol. 285:pp. 69–94.

Johansen, J.; Aagaard Madsen, H.; Sørensen, N.N. and Bak, C. (2006): Numerical investigation of a wind turbine rotor with an aerodynamically redesigned hub-region. In: European Wind Energy Conference and Exhibition. Athens, Greece.

Johansen, J.; Gaunaa, M. and Bak, C. (2009): Design of a wind turbine rotor for maximum aerodynamic efficiency. In: Wind Energy, Vol. 12(3):pp. 261–273.

Johansen, J. and Sørensen, N.N. (2004): Aerofoil characteristics from 3D CFD rotor computations. In: Wind Energy, Vol. 7(4):pp. 283–294.

Jonkman, J.; Butterfield, S.; Musial, W. and Scott, G. (2009): Definition of a 5-MW Reference Wind Turbine for Offshore System Development. Technical report NREL/TP-500-38060, National Renewable Energy Laboratory, USA.

Kožulović, Dragan (2007): Modellierung des Grenzschichtumschlags bei Turbomaschinenströmungen unter Berücksichtigung Mehrerer Umschlagsarten. PhD dissertation, Ruhr-Universität Bochum.

Lakshminarayana, B. (1996): Fluid dynamics and heat transfer of turbomachinery. John Wiley & Sons, Inc., New York.

Laursen, J.; Enevoldsen, P. and Hjort, S. (2007): 3D CFD Quantification of the Performance of a Multi-Megawatt Wind Turbine. In: Journal of Physics: Conference Series, Vol. 75(012007).

Le Balleur, J.C. (1981): Strong matching method for computing transonic viscous flows including wakes and separations. In: Lifting airfoils, La Recherche Aérospatiale, Vol. 3:pp. 21–45.

Lindenburg, C. (2003): Investigation into rotor blade aerodynamics: Analysis of the stationary measurements on the UAE phase-VI rotor in the NASA-Ames wind tunnel. Technical report ECN-C-03-025, The Energy Research Center of the Netherlands ECN.

Lindenburg, C. (2004): Modelling of rotational augmentation based on engineering considerations and measurements. In: European Wind Energy Conference. London.

Manwell, J.F.; McGowan, J.G. and Rogers, A.L. (2009): Wind Energy Explained: Theory, Design and Application. Second edition.

McCroskey, W.J. and Yaggy, P.F. (1968): Laminar boundary layers on helicopter rotors in forward flight. In: AIAA journal, Vol. 6(10):pp. 1919–1926.

Menter, F.R. (1994): Two-equation eddy-viscosity turbulence models for engineering applications. In: AIAA journal, Vol. 32(8):pp. 1598–1605.

Narramore, J.C. and Vermeland, R. (1992): Navier-Stokes calculations of inboard stall delay due to rotation. In: Journal of Aircraft, Vol. 29(1):pp. 73–78.

Natkaniec, C.K. (2012): Sekundärströmung in Turboladerturbinen mit variabler Turbinengeometrie. PhD dissertation, Leibniz Universität Hannover.

Ozturk, N.A.; Akcayoglu, A. and Sahin, B. (2009): Downstream particle image velocimetry measurements of a circular cylinder–plate junction. In: Proceedings of the Institution of Mechanical Engineers, Part C: Journal of Mechanical Engineering Science, Vol. 223(8):pp. 1837–1849.

Palau-Salvador, G.; Stoesser, T.; Fröhlich, J.; Kappler, M. and Rodi, W. (2009): Large eddy simulations and experiments of flow around finite-height cylinders. In: Flow Turbulence and Combust, Vol. 84(2):pp. 239–275.

Pattenden, R.J.; Turnock, S.R. and Zhang, X. (2005): Measurements of the flow over a low-aspect-ratio cylinder mounted on a ground plane. In: Experiments in Fluids, Vol. 39(1):pp. 10–21.

Ramos-García, N.; Sørensen, J.N. and Shen, W.Z. (2014): A strong viscous-inviscid interaction model for rotating airfoils. In: Wind Energy, Vol. 17(12):pp. 1957–1984.

Rauch, J.; Krämer, T.; Heinzelmann, B.; Twele, J. and Thamsen, P.U. (2007): 3D numerical simulation and evaluation of the air flow through wind turbine rotors with focus on the hub area. In: Wind Energy: Proceedings of the Euromech Colloquium. pp. 227–230.

Ronsten, G. (1992): Static pressure measurements on a rotating and a non-rotating 2. 375 m wind turbine blade. Comparison with 2D calculations. In: Journal of Wind Engineering and Industrial Aerodynamics, Vol. 39:pp. 105–118.

Sahner, J. (2009): Extraction of vortex strucutes in 3D flow fields. PhD dissertation, Otto-von-Guericke-Universität Magdeburg.

Savino, J.M. and Nyland, T.W. (1985): Wind turbine flow visualization studies. In: AWEA Wind Energy Conference. San Francisco, pp. 559–564.

Schlichting, H.T. (1979): Boundary-Layer Theory. McGraw-Hill Book Company, 7. edition.

Schreck, S. and Robinson, M. (2002): Rotational augmentation of horizontal axis wind turbine blade aerodynamic response. In: Wind Energy, Vol. 5(2-3):pp. 133–150.

Schreck, S.J.; Sørensen, N.N. and Robinson, M.C. (2007): Aerodynamic structures and processes in rotationally augmented flow fields. In: Wind Energy, Vol. 10(2):pp. 159–178.

Shen, W.Z.; Hansen, M.O.L. and Sørensen, J.N. (2009): Determination of the angle of attack on rotor blades. In: Wind Energy, Vol. 12(1):pp. 91–98.

Shen, W.Z. and Sørensen, J.N. (1999): Quasi-3D Navier-Stokes model for a rotating airfoil. In: Journal of Computational Physics, Vol. 150:pp. 518–548.

Sherry, M.; Sheridan, J. and Jacono, D.L. (2013): Characterisation of a horizontal axis wind turbine's tip and root vortices. In: Experiments in Fluids, Vol. 54(1417).

Sicot, C.; Devinant, P.; Loyer, S. and Hureau, J. (2008): Rotational and turbulence effects on a wind turbine blade – Investigation of the stall mechanisms. In: Journal of Wind Engineering and Industrial Aerodynamics, Vol. 96:pp. 1320–1331.

Snel, H.; Houwink, R. and Bosschers, J. (1994): Sectional prediction of lift coefficients on rotating wind turbine blades in stall. Technical report ECN-C–93-052, The Energy Research Center of the Netherlands ECN.

Sørensen, J.N. (2011): Aerodynamic Aspects of Wind Energy Conversion. In: Annual Review of Fluid Mechanics, Vol. 43(1):pp. 427–448.

Sørensen, N.N. and Schreck, S. (2012): Computation of the National Renewable Energy Laboratory Phase-VI rotor in pitch motion during standstill. In: Wind Energy, Vol. 15:pp. 425–442.

Sumner, D.; Heseltine, J.L. and Dansereau, O.J.P. (2004): Wake structure of a finite circular cylinder of small aspect ratio. In: Experiments in Fluids, Vol. 37(5):pp. 720–730.

Tachos, N.S. and Filios, A.W. (2009): A computational aerodynamics simulation of the NREL phase II rotor. In: The Open Mechanical Engineering Journal, Vol. 3(1):pp. 9–16.

Van Kuik, G.A.M. (2007): The Lanchester–Betz–Joukowsky limit. In: Wind Energy, Vol. 10(3):pp. 289–291.

Vermeer, L.J.; Sørensen, J.N. and Crespo, A. (2003): Wind turbine wake aerodynamics. In: Progress in Aerospace Sciences, Vol. 39(6-7):pp. 467–510.

Vladimir, C.; Horia, D.; Florin, F. and Alexandru, D. (2012): Determination of angle of attack for rotating blades. In: Incas Bulletin, Vol. 4(2):pp. 37–42.

Wang, H.; Zhou, Y.; Chan, C. and Zhou, T. (2009): Momentum and heat transport in a finite-length cylinder wake. In: Experiments in Fluids, Vol. 46(6):pp. 1173–1185.

Whale, J.; Anderson, C.G.; Bareiss, R. and Wagner, S. (2000): An experimental and numerical study of the vortex structure in the wake of a wind turbine. In: Journal of Wind Engineering and Industrial Aerodynamics, Vol. 84(1):pp. 1–21.

White, F.M. (1991): Viscous Fluid Flow. McGraw-Hill, Inc., second edition.

Wislicenus, G.F. (1947): Fluid Mechanics of Turbomachinery. McGraw-Hill Book Company, Inc., first edition.

Zahle, F. and Sørensen, N.N. (2011): Characterization of the unsteady flow in the nacelle region of a modern wind turbine. In: Wind Energy, Vol. 14(2):pp. 271–283.

A

APPROXIMATE SOLUTIONS OF IDEAL ROTOR DISCS

Glauert's general momentum theory (Sec. 2.1.2) derives that the aerodynamic performance of a rotor disc in an inviscid and incompressible flow is only dependent on the axial and rotational induction factors, and the local speed ratio (Eq. 2.19, Eq. 2.20, and Eq. 2.21). An alternative expression of the thrust coefficient

$$C_T = 4a'(1 + a')\lambda_r^2 \tag{A.1}$$

is obtained from Eq. (2.15) and Eq. (2.16). Since the thrust coefficients (Eq. 2.16 and Eq. A.1) must be equivalent, a relationship as a function of the axial induction factor, the rotational induction factor, and the local speed ratio is derived

$$a(1 - a) = a'(1 + a')\lambda_r^2. \tag{A.2}$$

Glauert (1935) suggested that for an ideal rotor disc with minimum energy loss due to wake rotation, the efficiency factor

$$\eta = \frac{1 + a'}{1 - a} = \frac{a}{\lambda_r^2 a'} \tag{A.3}$$

is constant all over the disc. Substituting Eq. (A.3) into Eq. (2.17) and Eq. (2.18), the axial induction factor

$$a = \frac{\lambda_r^2 \eta(\eta - 1)}{1 + \lambda_r^2 \eta^2} \tag{A.4}$$

and the rotational induction factor

$$a' = \frac{\eta - 1}{1 + \lambda_r^2 \eta^2}, \tag{A.5}$$

are reformulated. Thus, the thrust of an ideal annular rotor disc

$$dT = \pi R^2 \rho U_\infty^2 \frac{2(\eta - 1)}{\lambda^2 \eta^2} G(\lambda_r, \eta) \tag{A.6}$$

and the power of the ideal annular rotor disc

$$dP = \pi R^2 \rho U_\infty^3 \frac{2(\eta - 1)}{\lambda^2 \eta^3} G(\lambda_r, \eta) \tag{A.7}$$

are obtained by substituting Eq. (A.4) into Eq. (2.19) and Eq. (2.21), where

$$G(\lambda_r, \eta) = \frac{2\lambda_r^3 \eta^3 (1 + \lambda_r^2 \eta)}{(1 + \lambda_r^2 \eta^2)^2}$$

is a particular function, chosen in this study similarly to Glauer's approach for propellers. Therefore, the overall thrust coefficient

$$C_T = \frac{\int^{A_{\mathrm{D}}} dT}{\frac{1}{2}\rho U_\infty^2 \pi R^2} = \frac{4(\eta - 1)}{\eta^2} H(\lambda, \eta) \tag{A.8}$$

and the overall power coefficient

$$C_P = \frac{\int^{A_\mathrm{D}} dP}{\frac{1}{2}\rho U_\infty^3 \pi R^2} = \frac{4(\eta - 1)}{\eta^3} H(\lambda, \eta) \tag{A.9}$$

of the ideal rotor disc as a function of the efficiency factor and the tip speed ratio are obtained, where

$$\begin{aligned} H(\lambda, \eta) &= \frac{1}{\lambda^2} \int_0^\lambda G d\lambda_r \\ &= 1 - \frac{2 - \eta}{\lambda^2 \eta^2} \ln\left(\lambda^2 \eta^2 + 1\right) + \frac{1 - \eta}{\lambda^2 \eta^2 + 1}. \end{aligned} \tag{A.10}$$

The maximum energy output of the ideal rotor disc occurs when $\eta = 1.5$. At this condition, the axial induction factor and the rotational induction factor approach $1/3$ and 0 with increasing local speed ratios (Fig. 2.2).

B

3D BOUNDARY LAYERS ON THE WIND TURBINE BLADE

(a) Spanwise acceleration at the edge of the boundary layer

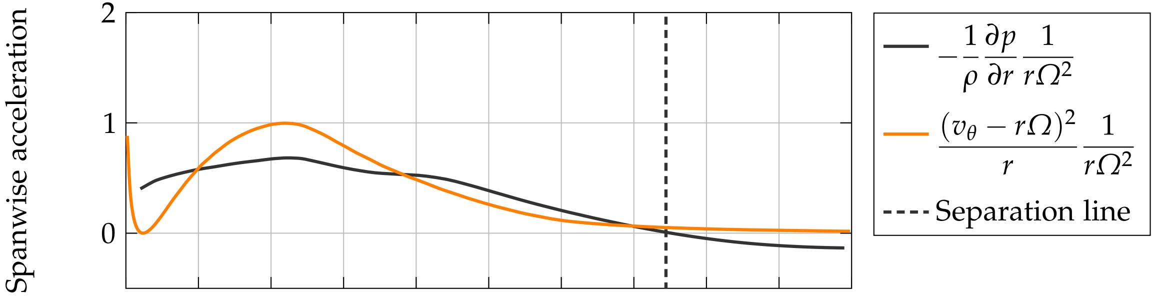

(b) Sapnwise acceleration in the boundary layer

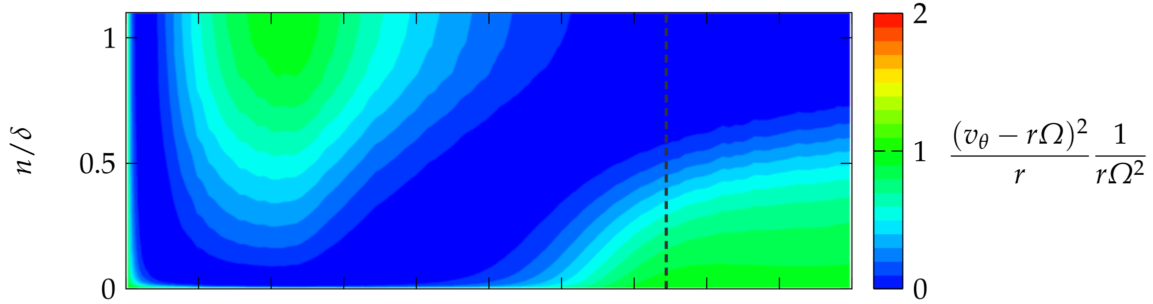

(c) Circumferential velocity in the boundary layer

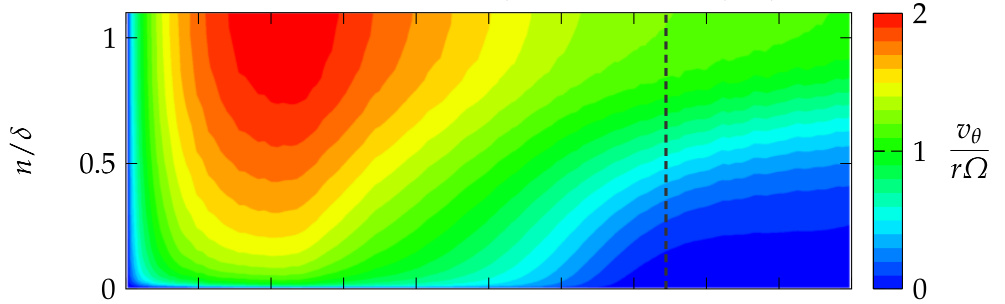

(d) Radial velocity in the boundary layer

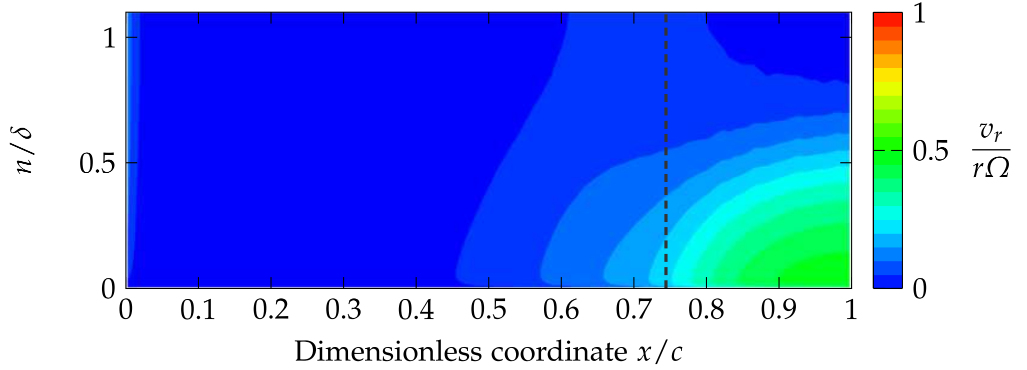

Figure B.1: Spanwise acceleration and velocity components in the boundary layer on the suction side of the wind turbine blade at $r/R = 0.252$ and $U_\infty = 11.4$ m/s

(a) Spanwise acceleration at the edge of the boundary layer

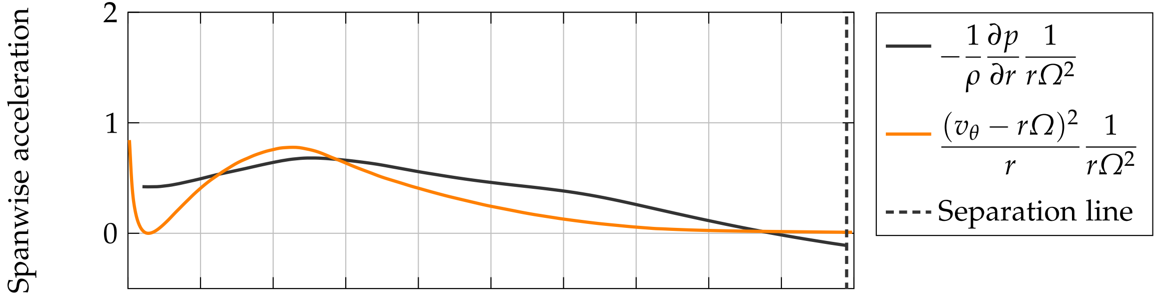

(b) Sapnwise acceleration in the boundary layer

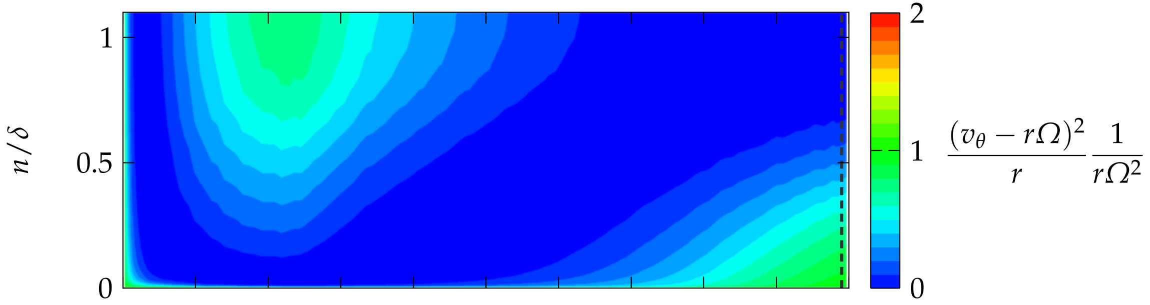

(c) Circumferential velocity in the boundary layer

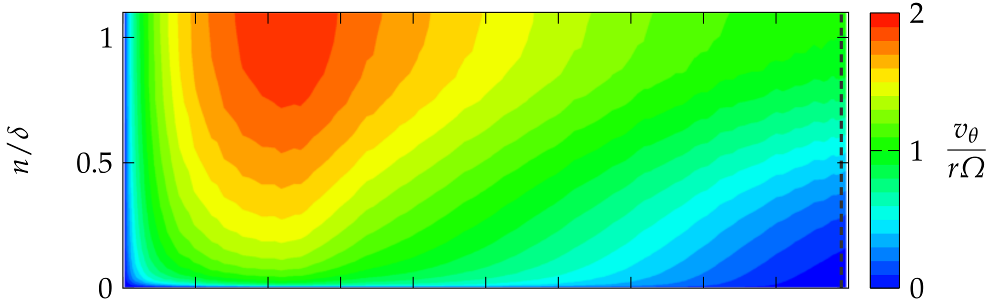

(d) Radial velocity in the boundary layer

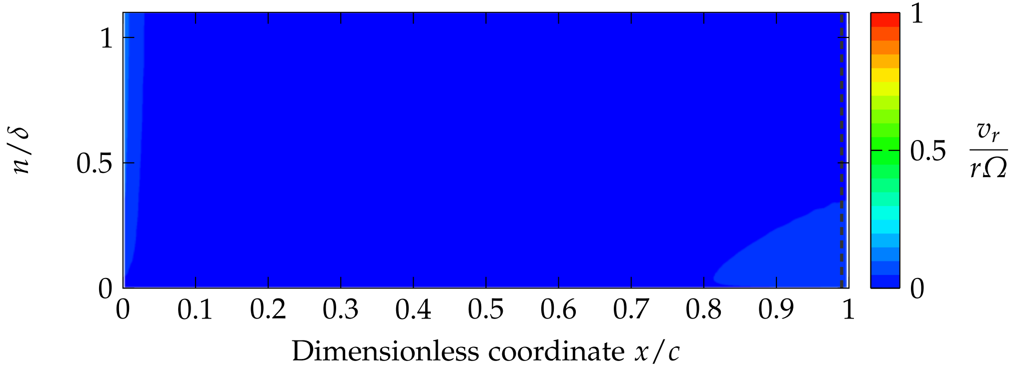

Figure B.2: Spanwise acceleration and velocity components in the boundary layer on the suction side of the wind turbine blade at $r/R = 0.317$ and $U_\infty = 11.4$ m/s

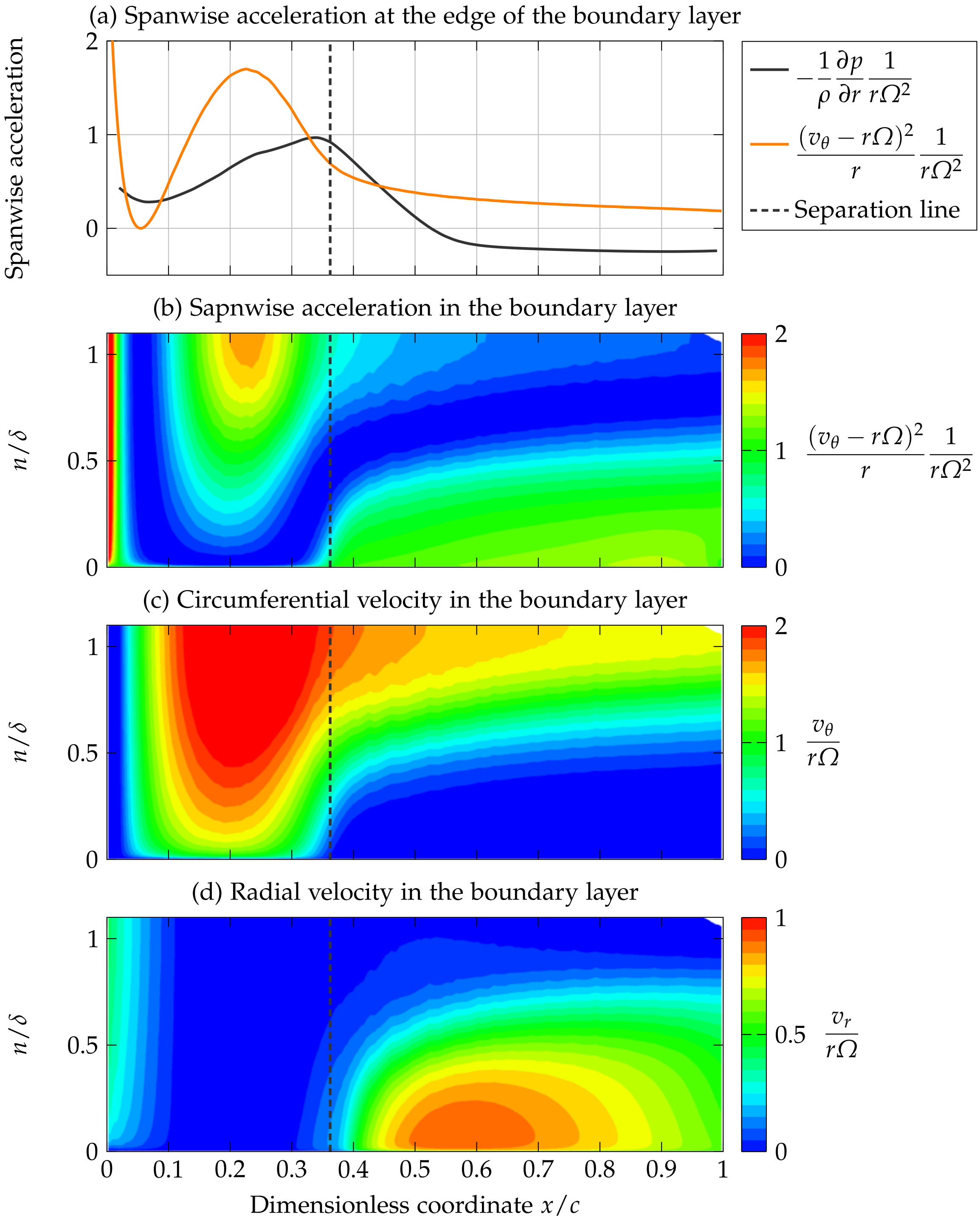

Figure B.3: Spanwise acceleration and velocity components in the boundary layer on the suction side of the wind turbine blade at $r/R = 0.176$ and $U_\infty = 20$ m/s

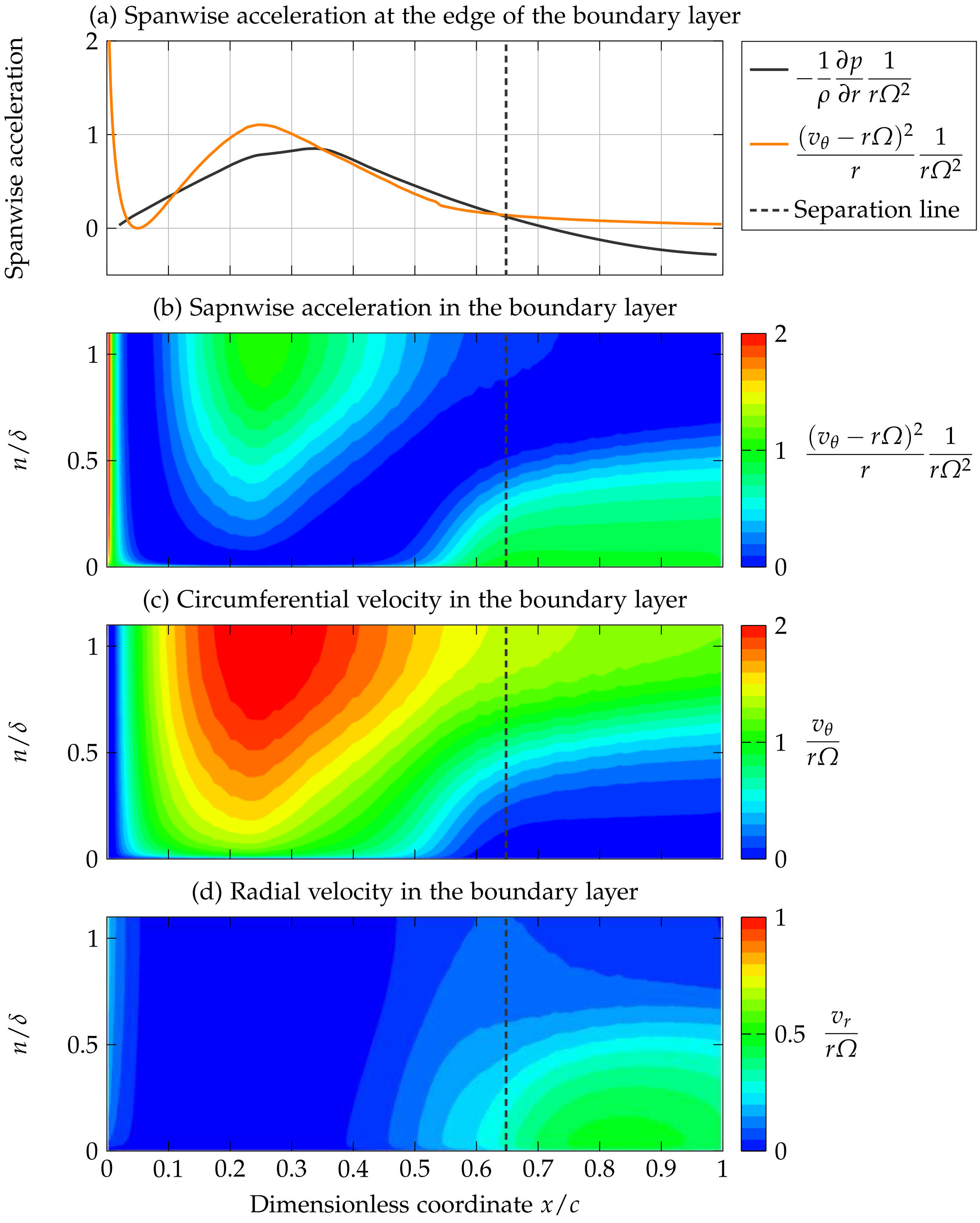

Figure B.4: Spanwise acceleration and velocity components in the boundary layer on the suction side of the wind turbine blade at $r/R = 0.252$ and $U_\infty = 20$ m/s

(a) Spanwise acceleration at the edge of the boundary layer

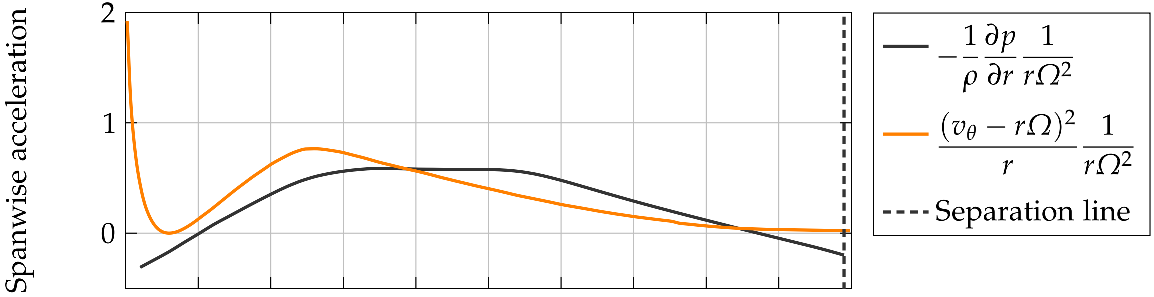

(b) Sapnwise acceleration in the boundary layer

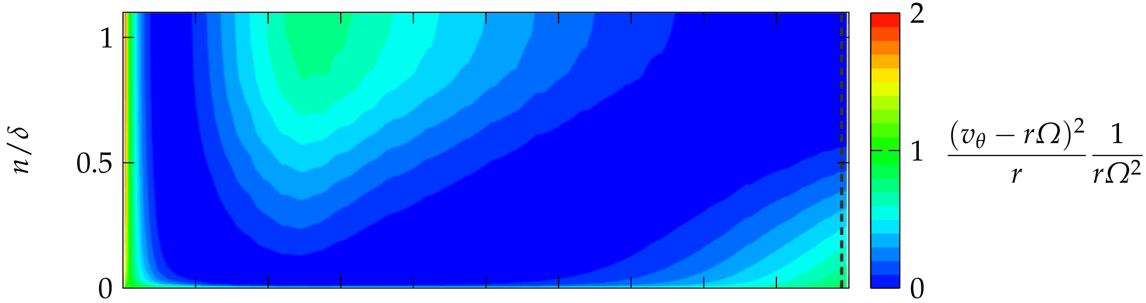

(c) Circumferential velocity in the boundary layer

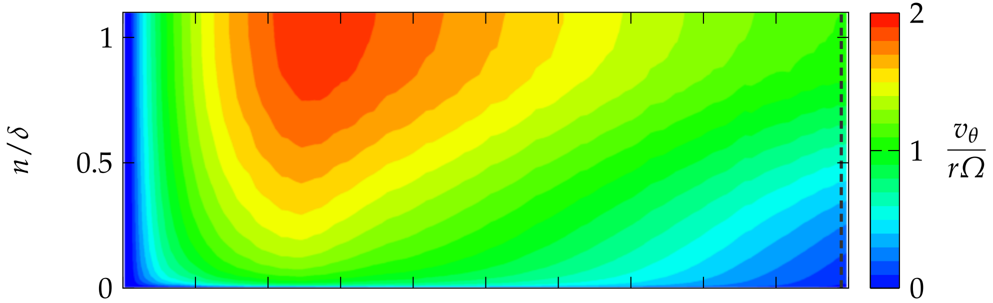

(d) Radial velocity in the boundary layer

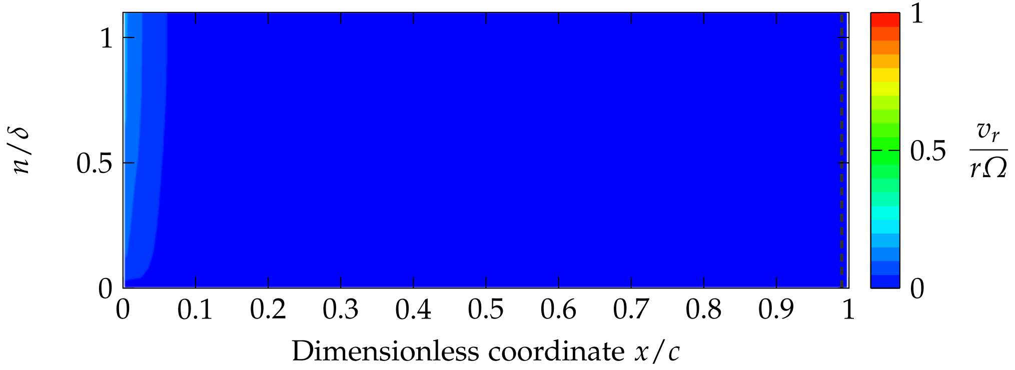

Figure B.5: Spanwise acceleration and velocity components in the boundary layer on the suction side of the wind turbine blade at $r/R = 0.317$ and $U_\infty = 20$ m/s

CURRICULUM VITAE

CONTACT

Shy-Yea Lin, M.Sc.
Glünderstr. 8
30167 Hannover, Germany
Phone: +49-176-2025-4980
Email: shyyealin@gmail.com

PERSONAL DETAILS

Date of birth	20th of December, 1983
Place of birth	Tainan, Taiwan
Nationality	Taiwan

EDUCATION

09.2002-08.2006	Bachelor of Science	National Cheng-Kung University (NCKU), Taiwan
09.2006-06.2008	Master of Science	NCKU, Taiwan

RESEARCH EXPERIENCES

07.2005-02.2006	Project: *Microexplosion of gas-in-liquid compound drops* Department of Mechanical Engineering, NCKU, Taiwan
01.2008-05.2008	Master Thesis: *Formation and burning of a stream of gas-in-oil compound drops* Department of Mechanical Engineering, NCKU, Taiwan
08.2008-07.2009	Research assistant Department of Mechanical Engineering, NCKU, Taiwan
08.2009-07.2010	Research assistant Department of Aerospace and Systems Engineering, Feng Chia University
since 10.2011	Ph.D thesis: *Coherent structures and rotational effects on the flow over spinners of horizontal axis wind turbines* Institute of Turbomachinery and Fluid Dynamics

LANGUAGE

Mandarin	native
Taiwanese	native
English	very good
German	very good

Hanover, November 5, 2016